5-2010

Petrogenesis of the Greenwater Range: Comparison to the Crater Flat volcanic field and implications for hazard assessment

Ashley Kaye Tibbetts
University of Nevada Las Vegas

PETROGENESIS OF THE GREENWATER RANGE: COMPARISON TO THE CRATER FLAT VOLCANIC FIELD AND IMPLICATIONS FOR HAZARD ASSESSEMENT

Ashley Kaye Tibbetts

Bachelor of Science
Boston University
2007

A thesis submitted in partial fulfillment
of the requirements for the degree of

Master of Science in Geoscience
Department of Geoscience
College of Sciences

Graduate College
University of Nevada, Las Vegas
May 2010

THE GRADUATE COLLEGE

We recommend that the thesis prepared under our supervision by

Ashley K. Tibbetts

entitled

Petrogenesis of the Greenwater Range: Comparison to the Crater Flat Volcanic Field and Implications for Hazard Assessment

be accepted in partial fulfillment of the requirements for the degree of

Master of Science
Geoscience

Eugene Smith, Committee Chair

Adam Simon, Committee Member

Pamela Burnley, Committee Member

Diane Pyper-Smith, Graduate Faculty Representative

Ronald Smith, Ph. D., Vice President for Research and Graduate Studies
and Dean of the Graduate College

May 2010

ABSTRACT

Petrogenesis of the Greenwater Range: Comparison to the Crater Flat Volcanic Field and Implications for Hazard Assessment

Ashley Kaye Tibbetts

Dr. Eugene I. Smith, Examination Committee Chair
Professor of Geoscience
University of Nevada, Las Vegas

Pliocene basalts of the Greenwater Range, California erupted from 24 volcanic vents now represented by volcanic plugs, craters and scoria mounds. Basaltic magmas originated in the asthenospheric mantle, but show evidence of a lithospheric component. Depths and temperatures of melting calculated using a silica activity geobarometer are 54.3–89.6 km and 1367-1435^{o}C, placing melting in the asthenosphere. The preferred petrogenetic model involves melting of lithospheric mantle thermally and mechanically, but not chemically, converted to asthenospheric mantle. Melting depths correspond to low velocity zones in the mantle as revealed in seismic profiles. Chemical and lithologic similarities between basalt in the Greenwater Range and basalt in Crater Flat, Nevada near the proposed nuclear waste repository at Yucca Mountain suggest that both are part of the same volcanic field. These factors result in an increase in the area and number of vents used to calculate volcanic hazard and accordingly an increased risk to the proposed repository.

TABLE OF CONTENTS

LIST OF FIGURES

ACKNOWLEDGMENTS

Thank you to Terry Plank for her advice and support, Clint Conrad for advice on mantle modeling and dynamics, Cin-Ty Lee for help with depth and temperature of melting calculations, and Jim Calzia for providing unpublished dates in the Greenwater Range. Thank you to my committee members, Dr. Adam Simon, Dr. Pamela Burnley, and Dr. Diane Pyper-Smith for their time and advice. Greatest thanks to Racheal Johnsen for all her help in the lab and editing. Thank you to Audrey Rager for help with editing. Thank you to Christi Emery and Kelly Robertson for help in the field and to Colin Robins for help in the field and support through the writing process. Special thanks to my adviser Dr. Eugene Smith for all his advice, encouragement, and infinite patience. Financial support for my graduate studies was provided by the Clark County Department of Comprehensive Planning, Nuclear Waste Division, the Inyo County Yucca Mountain Repository Assessment Office, and a Department of Geoscience teaching assistantship.

CHAPTER 1

INTRODUCTION

One of the major unsolved problems in petrology is the depth and source of melting and the evolution of basalts. With regard to the Greenwater Range in the Death Valley volcanic field in the western Great Basin, there are several contrasting models for the depth and cause of melting as well as the degree of melt contamination during ascent. These models will be discussed in detail in Appendix G. The controversy may in part be due to lack of specific knowledge regarding the geochemistry of the basalts and the lithosphere and crust/mantle structure of the area. The objective of this study is to use geochemistry and petrography to develop a petrogenetic model that provides a source and melting mechanism for the basalts of the Greenwater Range that can be compared to models for the evolution of the Crater Flat volcanic field (Fig. 1) to determine if these fields can be linked for the purposes of hazard assessment. The preferred model discussed in this thesis for the evolution of basalts of the Greenwater Range involves the melting of asthenospheric mantle that has been thermally and mechanically converted from lithosphere containing veins and pods of subduction-derived fluids. Melting may be initiated by upwelling in hot and/or wet areas (indicated by low S-wave velocity) of the asthenosphere. Comparison of the Greenwater Range with Crater Flat indicates this source and melting mechanism could be valid for both fields. This model for the Greenwater Range volcanic section can potentially be applied to similar volcanic systems in the Great Basin and to basaltic fields in similar tectonic environments in other parts of the world.

In addition to contributing to petrologic knowledge, these findings can be used for volcanic hazard assessment of this and nearby volcanic fields, which include Yucca Mountain (Fig. 1). Current probability for disruption of the proposed repository at Yucca Mountain by an igneous event is estimated to be 1.54×10^{-8} events/yr (Smith and Keenan, 2005). This calculation assumes that volcanism is confined to the immediate area around Yucca Mountain and all melting is in the lithospheric mantle (Smith and Keenan, 2005). Recently, it was proposed that the Greenwater Range is an extension of the Crater Flat-Lunar Crater volcanic belt (Fig. 2) and that melting occurs at depth in the asthenosphere (i.e. 115-133 km for Crater Flat). If the area used to calculate the volcanic hazard was extended to include the Greenwater Range, the risk of disruption of the proposed repository at Yucca Mountain could increase by several orders of magnitude (Wang et al., 2002; Smith et al., 2002; Smith and Keenan, 2005).

Geologic Background

The Greenwater Range is located in the Death Valley volcanic field, Inyo County, California (Fig. 1). The Greenwater Range lies on the eastern edge of Death Valley to the southwest of the Funeral Mountains and the Furnace Creek Fault (Serpa and Pavlis, 1996) and is 35 km south of Yucca Mountain, the site of a proposed high-level nuclear waste repository. The field is approximately 10 km by 20 km and consists mainly of basaltic lava flows and scoria cones. The age of the volcanic section is currently thought to be Pliocene-Quaternary (5 Ma-Recent) based on a K-Ar date of 4.14 ± 0.12 Ma of a basalt flow in the section (J. Calzia, personal communication, 2008), however, the analytical data required to evaluate this date is unavailable. A U-Pb zircon date (this study) for the underlying rhyolite of the Funeral Formation (Plate 1) sets the maximum age of the Greenwater Range basalt at 4.9 +/- 0.2 Ma.

The Greenwater Range is situated in the western Great Basin segment of the Basin and Range Province (Fig. 3) and is located to the east of the $^{87}Sr/^{86}Sr = 0.706$ line, which is the division between mid-Proterozoic basement of the craton to the east and accreted terrains to the west (Fig. 4) (Rogers et al., 1995). The Great Basin is an extensional region between the Colorado Plateau and the Sierra Nevada Mountains (Eaton, 1982).

Extension in the Death Valley area began 16 m.y. ago. The greatest extension rate was 20-30 mm/yr between 16-5 Ma, slowing to 10 mm/yr from 5 Ma to the present (Daley and DePaolo, 1992; Jones et al, 1992; Serpa and Pavlis, 1996; DePaolo and Daley, 2000). Total crustal extension accompanied by a decrease in lithospheric thickness in the southern Basin and Range (Sierra Nevada Mountains to the Nova Basin west of Death Valley) is estimated to be 250 km or 60-100% (Walker and Coleman, 1991; Daley and DePaolo, 1992; Harry et al., 1993; Zandt et al., 1995; Serpa and Pavlis, 1996). According to Daley and DePaolo (1992) and DePaolo and Daley (2000), crustal thinning is greater on the western and eastern edges of the Great Basin, in Death Valley and the Lake Mead area respectively, than in the rest of the Great Basin.

The Farallon Plate was actively subducting beneath the Death Valley region of the North American plate prior to 20 Ma, but moved north of 37^{o}N latitude by 20 Ma (Zandt et al., 1995) due to the development of the San Andreas Fault and the continued northeast migration of the Farallon slab (Bunge and Grand, 2000). The northern extent of the

Greenwater Range is located at approximately 36°7.5'N, and was located south of the Farallon slab at the time of volcanism.

The Greenwater Range is part of a northeast trending belt of Pliocene to Recent basalt fields that extends from the Death Valley area to the Lunar Crater field in central Nevada (Fig. 2). Magmatism in this belt is located in a northwest directed Great Basin extensional strain field (Walker and Coleman, 1991; Jones et al., 1992; Zandt et al., 1995) characterized by west dipping low-angle normal faults (Farmer et al., 1989; Walker and Coleman, 1991; DePaolo and Daley, 2000). The favored extensional model for the Basin and Range province is a simple shear model that results in the decoupling of upper crust from lower crust and mantle and non-uniform extension of crust and lithosphere (Walker and Coleman, 1991; Jones et al., 1992; DePaolo and Daley, 2000). In contrast, the Zandt et al. (1995) model assumes a pure shear model that links crust and mantle and requires uniform extension (Fig. 5). The simple shear model is preferred by Walker and Coleman (1991), Jones et al. (1992), and DePaolo and Daley (2000) for the Death Valley region.

The crust-mantle structure in the Death Valley region consists of a 30 km thick crust (Zandt et al., 1995; DePaolo and Daley, 2000), and a 20-40 km thick lithosphere (Fig. 6) (Jones et al., 1992; Zandt et al., 1995; DePaolo and Daley, 2000). The lithosphere-asthenosphere boundary rose over time as the crust and lithosphere thinned from approximately 100 to 40 km and the asthenosphere rose to fill the space (DePaolo and Daley, 2000).

Determining the source of the Greenwater Range volcanic section is complicated by the decoupling of the upper crust from the lower crust and lithosphere during simple shear extension. The Greenwater Range is located between the right-lateral Furnace Creek Fault to the northeast (Fleck, 1970) and the Greenwater Valley Fault to the southwest (Fig. 7) (Serpa and Pavlis, 1996) and is situated in the upper plate of a mid-crustal detachment. Isotopic evidence from 4-6 Ma basalts from the Nova Formation in the northern Panamint Mountains and Darwin Plateau indicates that lower crust and lithosphere from under the western Sierra Nevada was delaminated and moved to the east 150 to 250 km to a position beneath Death Valley after 10 Ma (Fig. 5) (Walker and Coleman, 1991). The delamination of the lithosphere under the Sierra Nevada Mountains is supported by a negative Bouguer gravity anomaly, and a low velocity zone indicating a low density, hotter mantle under the Sierra Nevada and a cooler mantle under Death Valley (Jones, 1987).

Previous Work

Mapping and Geochronology

Previous mapping by McAllister (1970), McAllister (1973) and, Streitz and Stinson (1977) placed the basalts in the Greenwater Range into the Funeral Formation. Although several geologic maps, both detailed and regional, exist for the Greenwater Range, no chemical analyses have been done for the basalts of the Funeral Formation in the northern Greenwater Range. One K-Ar date of 4.14$\pm$0.12 Ma (J. Calzia, personal communication, 2008) has been obtained for the basalt and one K-Ar date of 6 Ma has been obtained for the underlying rhyolite (Streitz and Stinson, 1977).

Previous Melting Models

The majority of previously proposed petrogenetic models to explain Basin and Range basaltic magmatism more or less agree that the source changed from lithospheric to asthenospheric mantle with time (Vaniman et al., 1982; Lum et al., 1989; Ormerod et al., 1991; Bradshaw and Smith, 1994; Rogers et al., 1995; Yogodzinski et al., 1996). Farmer et al. (1989) suggested that for a simple shear model (Fig. 5), lithospheric melting will occur in the area of greatest upper crustal extension and asthenospheric melting will occur in areas of greatest mantle lithospheric thinning. Contrary to this suggestion, Asmerom (1994) showed a change in the source of mafic magma from asthenospheric to lithospheric source due to the decrease in extension rate and the availability of structural pathways for magma ascent. The Asmerom model assumes pure shear extension and does not apply to the simple shear (Fig.5) extension model favored by Walker and Coleman (1991), Jones et al. (1992), and DePaolo and Daley (2000).

Melting models for the Death Valley-Lunar Crater belt include a variety of mechanisms for asthenospheric and lithospheric melting such as edge driven convection and asthenospheric upwelling (Savage and Sheehan, 2000; Conrad et al., 2009), slab window induced asthenospheric upwelling (Ormerod et al., 1988; Jones et al., 1992), melting of mafic components in sub-lithospheric mantle due to lithospheric thinning and subsequent crossing of the basalt solidus (Harry et al., 1993; Harry and Leeman, 1995), and the rapid extension of the lithosphere resulting in melting of H_2O-bearing peridotite (DePaolo and Daley, 2000). These models will be examined in detail in Appendix G.

Figure 1: Map depicting Greenwater Range volcanic centers and Crater Flat and surrounding volcanic fields. Red dots indicate volcanic centers.

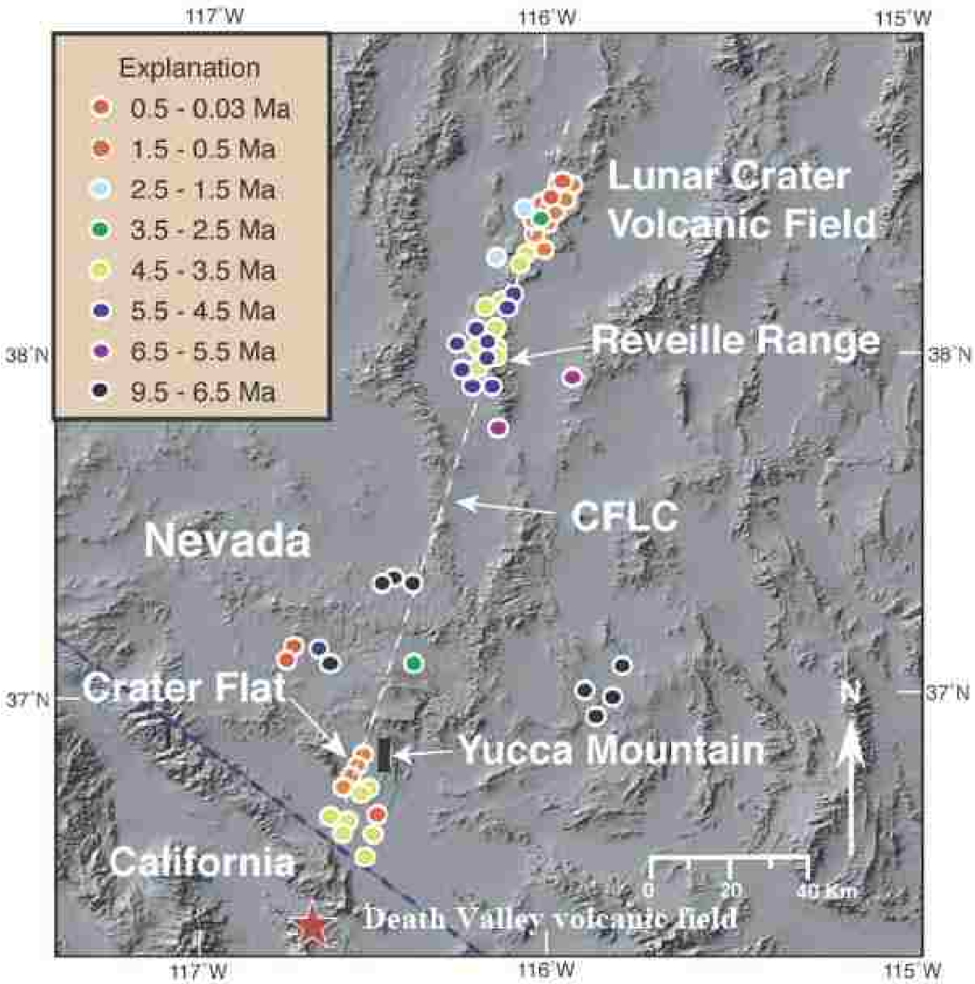

Figure 2: Location and age of 10 Ma-Recent basalts in the Lunar Crater-Crater Flat belt and the location of Yucca Mountain. Red star represents the Death Valley volcanic field. From Smith et al. (2002).

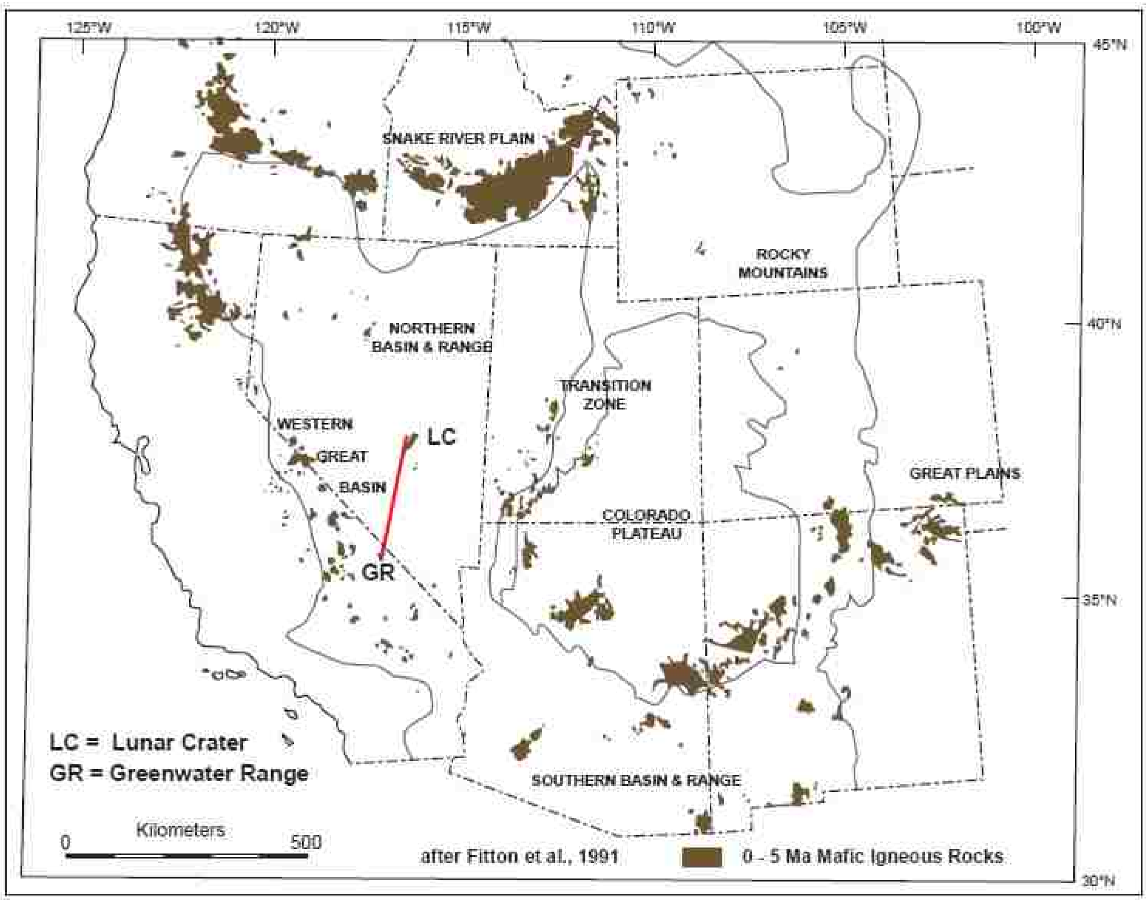

Figure 3: Map of the Great Basin showing locations of 5 Ma to present mafic volcanic rocks. Lunar Crater-Greenwater Range line through southern Nevada into southeastern California represents the Lunar Crater-Greenwater volcanic belt. After Fitton et al. (1991).

Figure 4: Location of the $^{87}Sr/^{86}Sr = 0.706$ line in relation to the Death Valley volcanic field (circled in red). The Lunar Crater-Greenwater belt lies to the east of the 0.706 line in the cratonic Proterozoic crust. From Rogers et al. (1995).

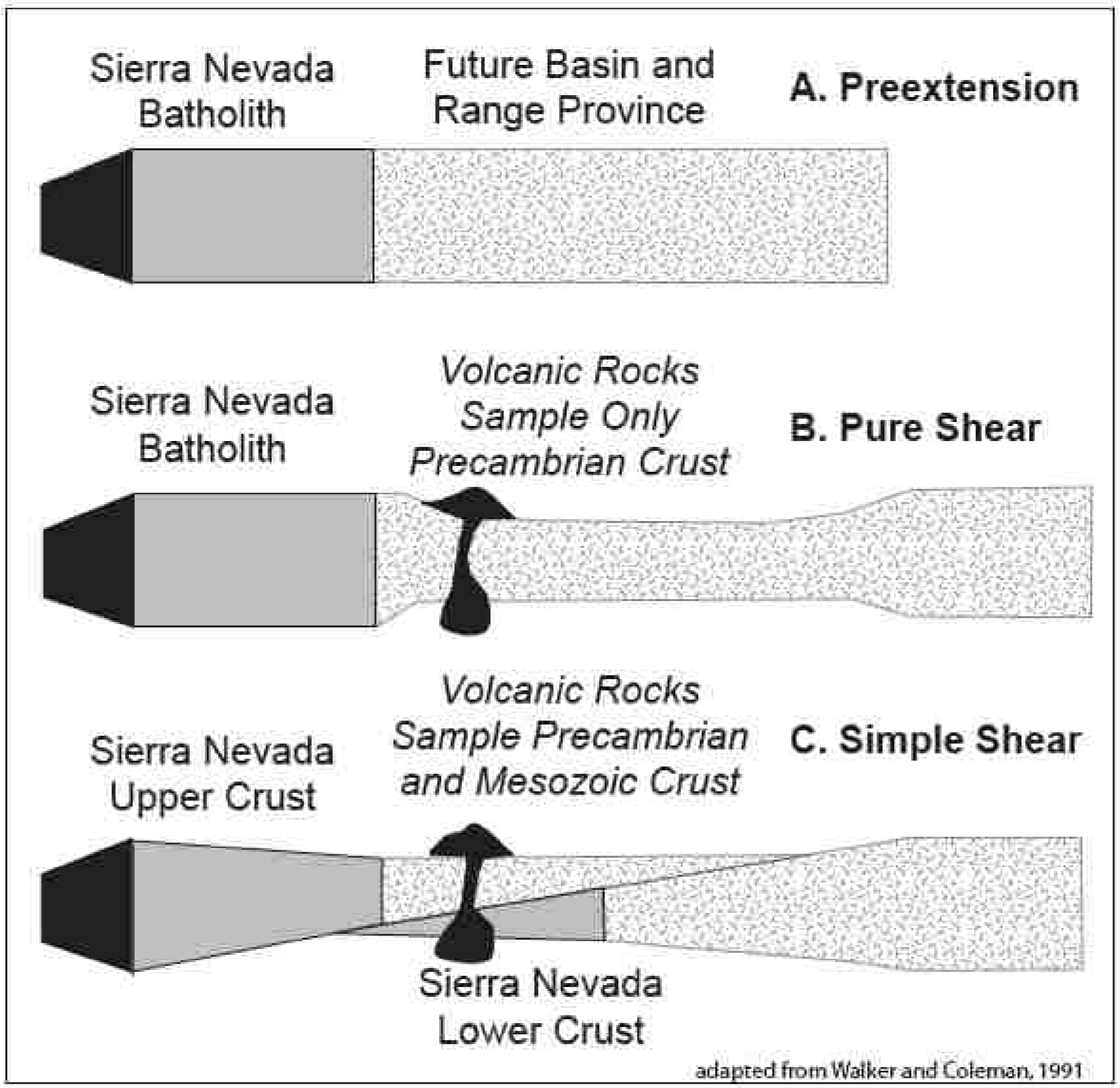

Figure 5: Pure shear vs. simple shear model for delamination of Sierran lithosphere. In pure shear the maximum deformation of crust and mantle coincide spatially. In simple shear models the maximum deformation of crust and mantle do not coincide (Walker and Coleman, 1991).

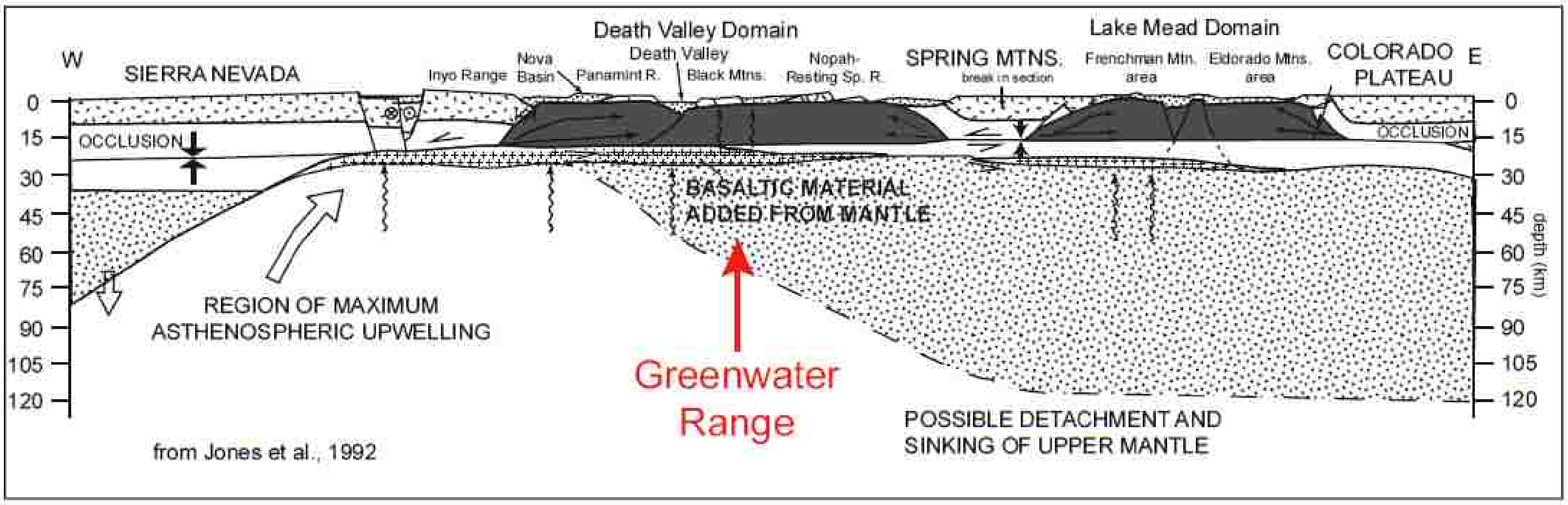

Figure 6: Model of crust-Mantle structure below the Death Valley region after Jones et al. (1992).

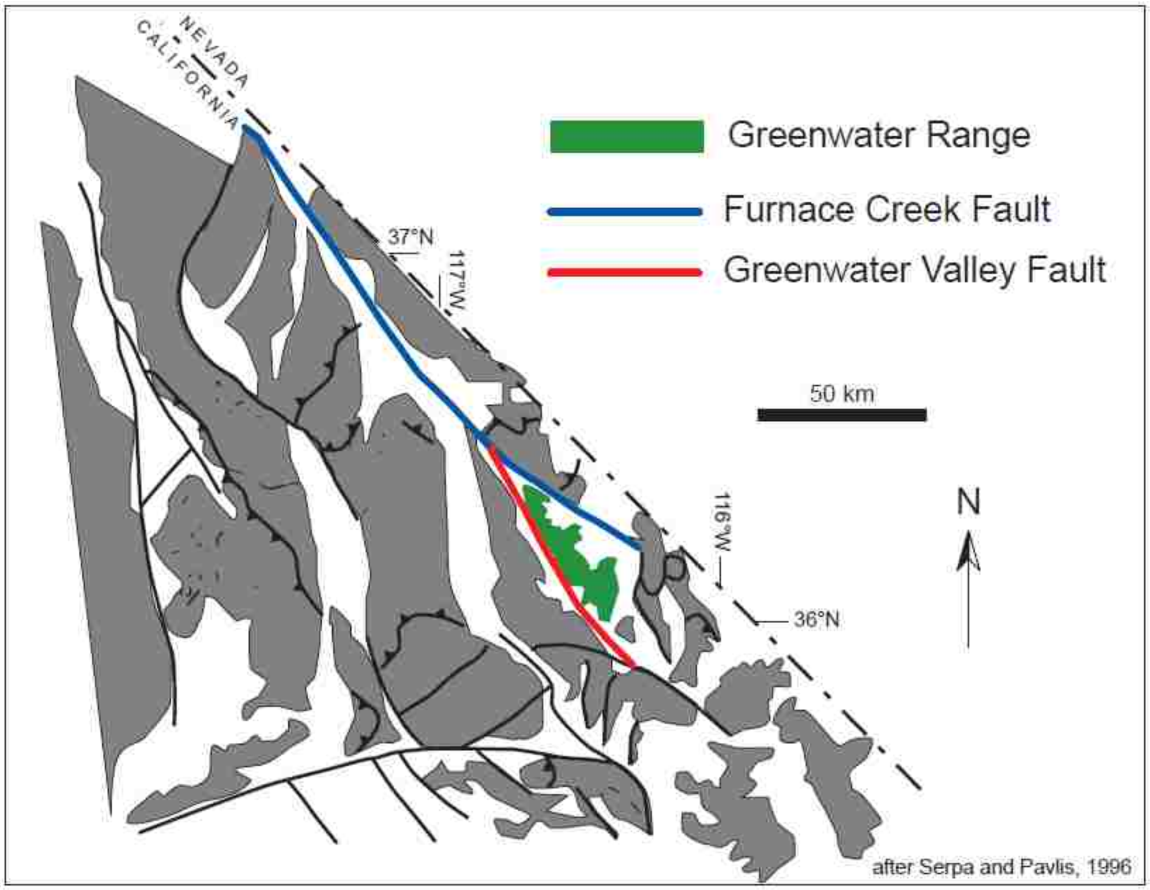

Figure 7: Locations of faults bordering the Greenwater Range (green) (after Serpa and Pavlis, 1996).

CHAPTER 2

GEOLOGY OF THE GREENWATER RANGE

Description of Centers

Location of Vent Areas

The Pliocene basalt and basaltic andesite of the Greenwater Range's Funeral Formation contains twenty-four volcanic centers and numerous lava flows. The centers are located as shown in Figure 8, extending from the northwest near the mining town of Ryan where the range meets California Highway 190 to the southeast, ending where Shoshone Ridge meets State Highway 127. Names of centers are shown in Figure 9. Individual vents are described in detail below.

General Features

All basalt exposed for long periods of time is covered in a layer of desert varnish and vesicles tend to be filled at least partially with caliche. In general, basalt flows overlie the preexisting topography and have not been significantly tilted. The exception occurs in the northeastern part of the range, close to the Furnace Creek fault where flows are tilted up at ~30^{o} to the northwest. Lava flows that erupted from the 24 centers consist of alternating layers of agglomerate and massive basalt that varies in thickness from approximately 200 meters at the northeastern end of the field to approximately 100 meters in the southwest and as little as 5 meters in areas at the basalt-rhyolite contact (Plate 1). In general, flow thickness decreases from northeast to southwest. The dimensions of each of the 24 centers are listed in Table 1. Stratigraphic relationships (Fig. 10) were largely determined by the law of superposition.

Table 1: Dimensions of Volcanic Centers in the Greenwater Range

Center	Diameter (m)	Height (m)
Three Peaks (west)	215 x 215	80
Three Peaks (north)	220 x 240	85
Three Peaks (east)	390 x 380	75
Smith's Climb	300 x 350	100
Secondary Smith Vent	230 x 240	33
Crater	1000 x 800	-140
Two Peaks (smaller south)	150 x 120	25
Two Peaks (larger north)	270 x 280	90
Point Cone	950 x 430	160
Lower Cone 1	550 x 350	106
Lower Cone 2	430 x 600	56
Lower Plug	330 x 280	53
Lower Scoria Hill	125 x 100	12
Mesa Center	250 x 320	22
Tall Peak	500 x 375	170
Old Peak	200 x 290	65
Twin Peaks (larger NW))	300 x 325	86
Twin Peaks (smaller SE))	225 x 260	30
buried peak (north)	190 x 205	20
buried peak (middle)	100 x 100	5
buried peak (south)	90 x 50	10
Lower Ridge	900 x 520	50
Southeast Center	2175 x 1890	260
Shoshone Ridge	250 x 125	15

Petrography

Greenwater Range basalts range from 40-98% matrix and contain phenocrysts of plagioclase, olivine, and oxides. In the matrix, olivine is most commonly altered to iddingsite, plagioclase occurs as stubby laths to acicular crystals, and oxides occur as individual cubic crystals and anhedral masses.

Olivine is the most common phenocryst and is euhedral to anhedral and often partially to totally altered to iddingsite. Plagioclase phenocrysts occur as rectangular laths with albite twinning and less commonly as stubby blockier laths. Oxide phenocrysts are opaque, cubic and/or anhedral clumps. Oxides also occur as inclusions in olivine phenocrysts.

Xenocrysts are defined by degradation of their crystalline structure and resorption of the crystal due to lack of chemical equilibrium with their surroundings. Xenocrysts include quartz, potassium feldspar, and plagioclase in varying stages of resorption and in highly degraded amoeboid to crystalline shapes and can appear as glomerocrysts. The most common xenocryst is plagioclase with some twinning still evident. Centers that contain xenocrysts include: Smith's climb, the Lower Cones, Lower Ridge, Buried Cones, and the dacite and basaltic andesite of Shoshone Ridge.

Detailed descriptions of individual thin sections can be found in Appendix A and sizes and percentages are summarized in Table 2.

Three Peaks

Three Peaks is a group of three well defined, little eroded, cinder covered cones about the edge of a playa (Pic 1, in appendix H). The cones have conduits containing breccia and agglomerate with highly vesicular basalt blocks covered by varying amounts of red scoria and sculpted bombs (< 20 cm). A dike connects the two northwestern cones (two left most in picture 1) of the Three Peaks cinder cones. The flows from the northeastern point of the field to the north of Ryan are associated with these cones. This center and flows overlie sedimentary layers of the Furnace Creek and Artist Drive Formations.

In thin section, the basalt is highly vesicular with 98% matrix made up of plagioclase and minor olivine (altered to iddingsite) and oxides. Phenocrysts are predominantly small (<0.25 mm), partially altered, subhedral olivine with rare small plagioclase (<0.25 mm).

<u>Smith's Climb and Secondary Vent</u>

Smith's climb is a basaltic-andesite plug (Pic 2). Although the basaltic andesite conduit is all that remains of the main vent, there is some scoria still present on the flat summit and flows related to Smith's climb (Pic 2). A poorly defined secondary vent lies approximately 100 m northeast of Smith's climb. It is considerably smaller than the main vent and is composed only of a small area of basaltic andesite blocks. It does not appear to have any scoria associated with it and most likely no flows. Flows from Smith's Climb overly those of the Crater, which are exposed in Crater Canyon to the west (Fig. 8).

In thin section, basalt from Smith's Climb contains 95% matrix with mostly plagioclase and olivine and some oxides and glass. Phenocrysts are primarily olivine with occasional small (<0.25 mm) plagioclase. Sample DV-08-116 contains partially resorbed feldspar and quartz xenocrysts. Olivine shows minor alteration to iddingsite and few oxide inclusions.

Crater

The Crater (Pic 3) is one of the largest centers (Table 1). This center displays both Hawaiian-type deposits composed largely of scoria and bombs (Pic 4) and Strombolian deposits composed almost entirely of bombs. The bombs in these deposits tend to have vesicular cores and massive rims. A dike cuts the edge of the Crater and the Crater itself contains a conduit with a radiating dike swarm emanating from it. There is still a portion of the Crater wall exposed with steeply dipping scoria deposits plastered against the crater wall (Pic 5). The Crater and associated flows directly to the north contain sedimentary xenoliths (Pic 6) that appear to be from the Furnace Creek and Artist Drive Formations that underlie the young basalt. The xenoliths show no evidence of assimilation, reinforcing the idea that they came from the immediately underlying sedimentary rock and had no time to assimilate before the basalt cooled.

In thin section, basalt from the Crater contains 90% matrix composed of plagioclase with less common olivine and oxides. Phenocrysts are predominantly subhedral olivine altered to iddingsite and minor amounts of small (0.5 mm) plagioclase laths.

Two Peaks

Two Peaks is a pair of symmetrical, dome shaped centers that sit above the surrounding flows and are composed primarily of highly vesicular basalt. The well defined northern peak is composed of agglomerate with massive flows of olivine (altered to iddingsite) basalt. The less defined, more weathered southern peak is smaller than the northern peak (Table 1) and is separated from it by scoria beds and a small knob of basalt

(Pic 7). Flows from Two Peaks overlie sedimentary units of the Furnace Creek and Artist Drive Formations.

In thin section, basalt of Two Peaks contains 70% matrix composed of plagioclase and minor olivine and oxides. Phenocrysts are predominantly olivine largely altered to iddingsite with abundant oxide inclusions.

Point Cone

Point Cone is a series of vents along a dike that over time produced a cone cluster (Pic 8). The cone cluster is mainly composed of scoria except for agglomerate and basalt in vent areas and is covered by large (up to 2 m) sculpted bombs (Pic 9). The flows associated with this peak extend to the southwest. Point Cone may be the source of part of the upper portion of the large flow stack to the west of Point Cone (Plate 1).

Lower Cone 1

Lower Cone 1 is the larger of two cones that occur at lower elevation in the east part of the Greenwater Range. The cone is very well defined and consists of two closely spaced knobs (550 x 350 m) connected by a dike that may have originally extended to a third knob (275 x 150 m) to the northeast (Pic 10) that is now cut off by a gully. These three knobs represent vent areas aligned northeast-southwest. Dikes crop out on the flank of the cone that is otherwise covered by scoria (Pic 11). Vent areas are composed of agglomerate with vesicular basalt blocks. A lobate basalt flow to the southeast of Smith's Climb may have originated from Lower Cone 1 and perhaps Lower Cone 2. The basalts of Lower Cone 1 overlie sedimentary rocks of the Furnace Creek and Artist Drive Formations.

Lower Cone 2

Lower Cone 2 is smaller than Lower Cone 1 (Table 1) and consists of a scoria covered cone with a well defined agglomerate and vesicular basalt conduit (Pic 12). Vesicular basalt blocks occur at the summit along with < 10 cm long sculpted bombs. Larger (~ 0.5 m) sculpted bombs are found on the flanks of the cone (Pic 13).

In thin section, samples from Lower Cones 1 and 2 contain up to 85% matrix that consists primarily of plagioclase with the remainder either glass or olivine and oxides. Phenocrysts are olivine with some small (0.25 mm) and rare larger (0.5 mm) plagioclase. Both samples from the Lower Cones contained partially resorbed quartz and feldspar xenocrysts. Olivine phenocrysts are abundant, small (0.25-0.75 mm), euhedral to subhedral, and partially to completely altered to iddingsite.

Lower Plug

The Lower Plug is a highly eroded but well-defined conduit (Pic 14) with no associated flows. The conduit has a dark glassy outer section and a coarse grained lighter inner section. The plug has a fan-shaped cross section and is surrounded by breccia that contains sedimentary xenoliths most likely from the underlying Furnace Creek and Artist Drive Formations. This vent erupted through the underlying sedimentary rocks of the Furnace Creek and Artist Drive Formations and ash possibly from the eruption of the rhyolite of the Funeral Formation based on its proximity.

Lower Scoria Hill

The Lower Scoria Hill is a small scoria covered vent (Table 1) with agglomerate and vesicular basalt blocks. There are no associated flows or bombs. This vent erupted through the underlying sedimentary rocks of the Furnace Creek and Artist Drive Formations.

Samples from the Lower Scoria Hill and Lower Plug show varying amounts of vesiculation and are on average 85% matrix. Basalt of the Lower Plug is mostly plagioclase with minor olivine and oxides and also contains several olivine and plagioclase glomerocrysts. The matrix of the basalt of the Lower Scoria Hill mostly contains plagioclase with some oxides and glass. Phenocrysts are olivine with minor alteration to iddingsite and minor plagioclase.

Mesa Center

The Mesa Center (Pic 15) is isolated from the other centers. It is therefore assumed that the flows that surround this center are associated with it. The center itself is mostly obscured by flows and the exposed portion is inaccessible. The scoria and flow units that comprise the vent are eroded on one side where a cross section of the vent is well exposed. The whole vent/flow complex overlies sedimentary rocks of the Furnace Creek and Artist Drive Formations.

Tall Peak

Tall Peak is the largest peak in the southwestern part of the field. It is a well-defined center that overlies Old Peak immediately to the west. The associated flows extend to the west (Pic 16) and overlie sedimentary rocks of the Furnace Creek and Artist Drive Formations. There are no bombs but a considerable amount of scoria has been exposed by erosion. Besides scoria, the cone consists of massive light blue basaltic andesite with olivine altered to iddingsite at the base and agglomerate closer to the summit.

Old Peak

Old Peak (Pic 17) is highly eroded and partially buried by Tall Peak (Pic 16), but the conduit is still visible. Old Peak is composed of highly weathered and jointed light blue basalt with olivine altered to iddingsite. Any scoria that may have been present has been eroded.

In thin section, basalt from Old Peak is 85% matrix made up of plagioclase with less common olivine, oxides, and glass. Phenocrysts are mostly olivine with rare small (0.5 mm) plagioclase. Olivine is anhedral and partially altered to iddingsite.

Twin Peaks

Twin Peaks are a pair of well-defined, cinder cones. The western cone is the larger of the two, is basaltic andesite, and has abundant scoria on its flanks. Flows from the western cone surround the smaller eastern basalt cone, indicating the eastern cone is older. Both cones consist of vesicular basalt/basaltic andesite, small bombs (< 20 cm), and agglomerate arranged about the conduit. Flows from Twin Peaks overlie outcrops of the rhyolite of the Funeral Formation (Pic 18). Cumulate and mantle peridotite xenoliths were found in flows from Twin Peaks just above the contact between basalt and rhyolite of the Funeral Formation. West of Twin Peaks, lava flows overlie sedimentary rock of the Furnace Creek and Artist Drive Formations.

Buried Peaks

The Buried Peaks consist of three knobs locally overlain by scoria. Vent areas are poorly exposed but appear to consist of agglomerate and highly vesicular basalt blocks. Vents are mostly buried by younger flows so little about their structure is known.

Basalt of Buried Peaks is on average 85% matrix primarily consisting of plagioclase with less common glass, oxides, and olivine. Phenocrysts are primarily olivine with minor oxides and rare small (0.25 mm) plagioclase. Olivine is variably altered, with oxide inclusions. Partially resorbed xenocrysts include plagioclase and quartz.

Lower Ridge

Lower Ridge is isolated from any other centers. It is assumed, therefore, that the low-volume flows that surround this vent are associated with it. The basalt of Lower Ridge consists of a thin flow overlying lake sediments of the Furnace Creek Formation. The basalt is mostly agglomerate and highly vesicular basalt blocks with minor scoria arranged about a vent area.

In thin section, Lower Ridge contains 80% matrix composed of plagioclase and some olivine. Phenocrysts are mostly small (0.25-0.5 mm), anhedral, olivine partially altered to iddingsite. Phenocrysts also include some plagioclase with a bimodal (<0.25, 0.5 mm) size distribution and particularly distinct albite twinning. Xenocrysts include partially resorbed quartz and plagioclase.

Southeast Center

The Southeast Center is basaltic andesite and is composed of a series of well-defined conduits (Pic 19) that form a cone shape that is crosscut by several dikes. In addition to the main conduits there is a plug intruding the northern part of the cone. A thick stack of flows on the west side of Southeast Center is clearly related to this center (Pic 20). A thin flat lying basaltic andesite flow that erupted from Southeast Center overlies the tilted older basalt of the Greenwater Volcanics. This is the only place where the young basalt or basaltic andesite overlies the older Greenwater volcanic section.

Shoshone Ridge

Shoshone Ridge is in the extreme eastern part of the Greenwater Volcanic field just west of California Highway 127 (Fig. 8). Just west of the ridge is a mound-shaped hill of basaltic andesite. The western part of the ridge is composed of a dacite flow and the eastern part is a basalt flow that erupted from an eroded cinder cone.

In thin section, the dacite is vesicular and contains 95% matrix primarily composed of plagioclase with minor oxides. Clinopyroxene, olivine, plagioclase, and quartz are present, but some are embayed and have corroded rims, implying that many if not all are xenocrysts.

The basaltic andesite and basalt are massive and average 85% matrix composed primarily of plagioclase with some olivine and oxides. The phenocrysts are primarily small (0.25-0.5 mm) anhedral olivine mostly altered to iddingsite and a few large (1-1.5 mm) less altered olivine with rare small (0.25-0.5 mm) plagioclase. The basaltic andesite contains several partially resorbed plagioclase xenocrysts.

Rhyolite

The rhyolite of the Funeral Formation is flow banded and devitrified and is overlain by approximately four meters of thinly bedded rhyolite surge deposits that are in turn overlain by the basalt of the Funeral Formation. A U-Pb age of 4.9 +/- 0.2 Ma was obtained from zircons analyzed by SIMS at the University of California Los Angeles. Basaltic enclaves occur in the rhyolite (Pic 21) near the basalt-rhyolite contact, but were not identified elsewhere. Because this project was focused on basalt, the rhyolite was only explored in enough detail to determine its relationship to the basalt.

Table 2: Thin section size and percentage summary for centers.

center	% matrix	% phenocrysts	% olivine	size (mm)	% plagioclase	size (mm)	% oxides	xenocrysts	size (mm)
Smith's Climb	95	5	99	0.25-1	1	0.25-0.5	0	feldspar, quartz	1-1.5
Lower Cones	80-90	10-20	95	0.25-0.75	5	0.25-0.5	0	feldspar, quartz	0.5-1.5
Shoshone Ridge	80-95	5-20	95-98	0.25-1.5	2-5	0.25-1	0	plag, feldspar, quartz	1-2
Three Peaks	98	2	100	<0.25	0	---	0	---	---
Crater	90	10	95	0.25, 0.75	5	0.5	0	---	---
Two Peaks	70	30	95	1-2	0	----	5	---	---
Lower Ridge	80	20	80	0.25-0.5	20	<0.25-0.5	0	plag, feldspar, quartz	0.25-2.5
Lower Plug & Scoria Hill	85-88	12-15	90-95	0.25-0.5, 1-1.5	5-10	0.25	0	---	---
Buried Peaks	70-90	10-30	50-95	0.25, 1-2	5	0.25	0-45	plag, feldspar, quartz	0.5-2
Old Peak	85	15	95	0.5-1	5	0.5	0	---	---

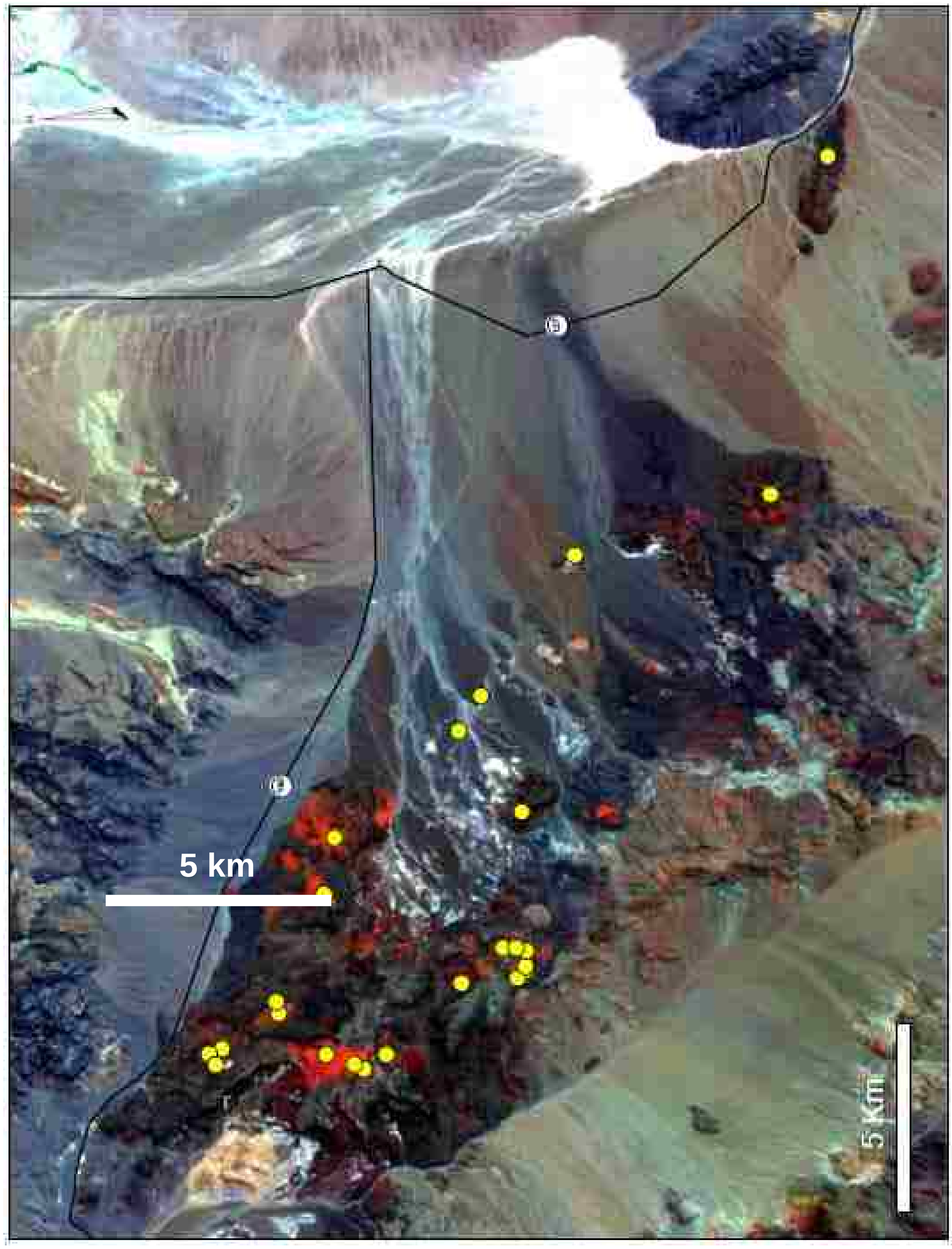

Figure 8: Distribution of Greenwater Range Pliocene basalt centers, denoted by yellow dots.

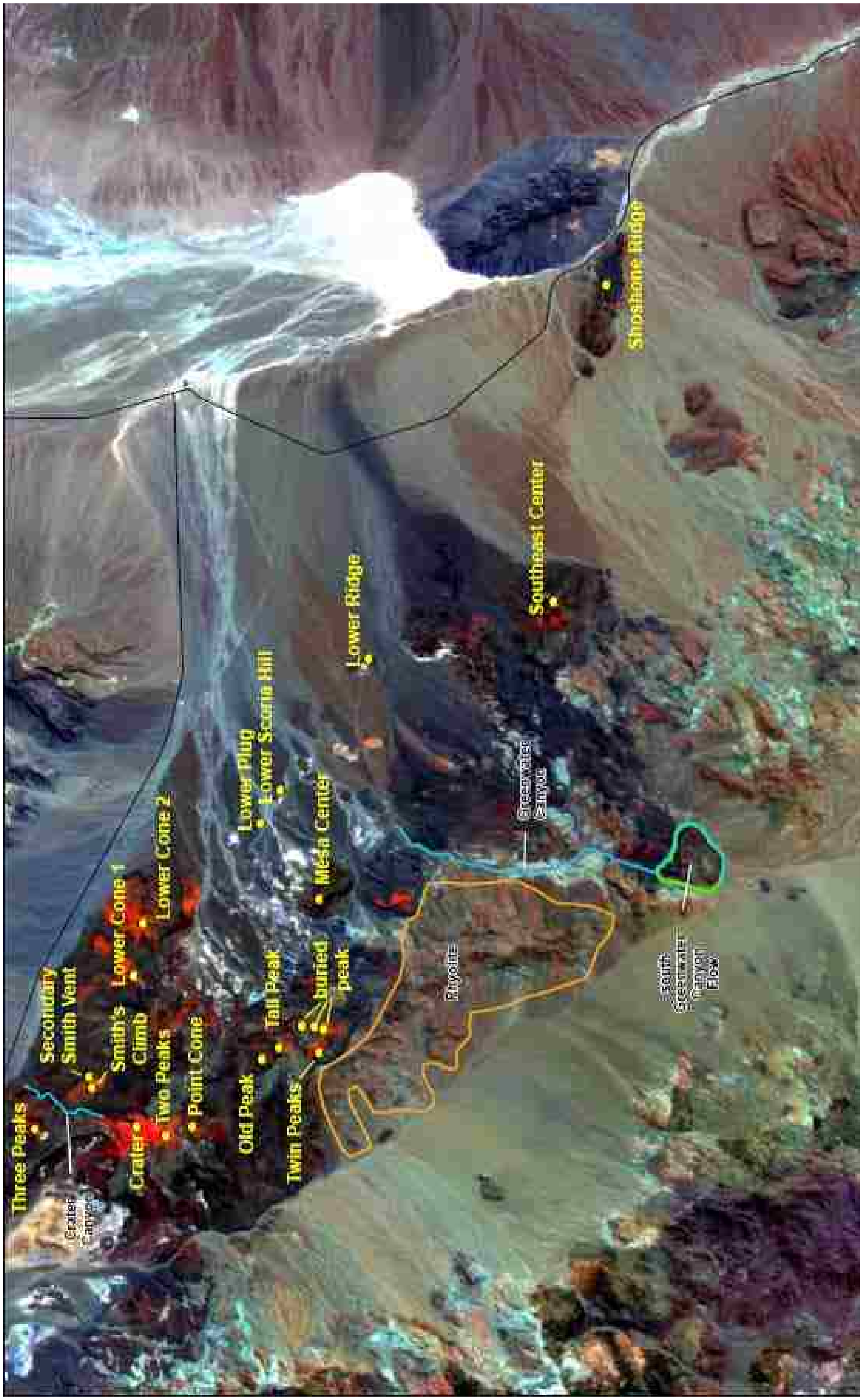

Figure 9: Google Earth Map showing locations and names of Greenwater Range Pliocene basalt/basaltic andesite centers, and Pliocene rhyolite.

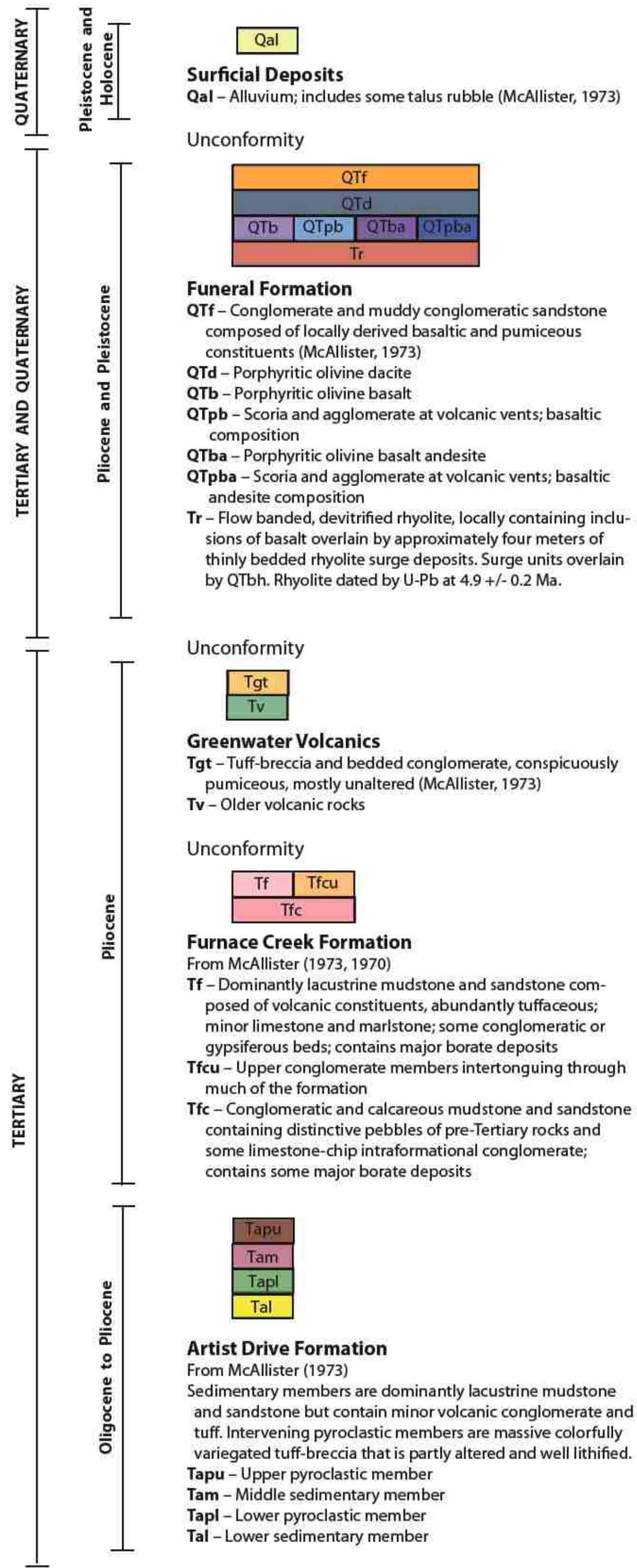

Figure 10: Stratigraphic column for Greenwater Range and immediately surrounding area.

CHAPTER 3

GEOCHEMISTRY OF THE GREENWATER RANGE

Field and Instrumental Techniques

Sample Collection

Sample collection (Fig. 11) was mainly restricted to basalt and basaltic andesite of the Funeral Formation, but several samples of rhyolite of the Funeral Formation and basalt of the Greenwater Volcanics were also collected. In addition, several sedimentary units and the lower pyroclastic member of the Artist Drive Formation were collected for comparison with sedimentary xenoliths in basalt. Sample collection of flows and volcanic centers was accomplished by breaking off representative pieces of the unit with enough unweathered and largely massive interior to be of use for chemical analysis and thin sections (0.5 to 1 gallon bag). These samples were stored in plastic bags labeled with sample numbers and the latitude, longitude, and elevation. Location data are reported in Appendix B.

Sample Preparation

Sample preparation for chemistry was accomplished using the following methods. The original ~≤10 cm sample pieces collected in the field were crushed into ~≤2 cm pieces using the Badger Rock Crusher. These chips were stored in labeled plastic bags until needed. The Badger was cleaned with compressed air and paper towels between each sample to prevent contamination. The crushed samples were then picked for 60 mL of unweathered chips. These unweathered chips were then powdered using a tungsten carbide shatter box for 3 minutes. The shatter box was cleaned with compressed air and paper towels between samples and gloves were worn when transferring powder from the shatter box to labeled plastic bags to prevent contamination.

Powdered samples were placed in glass vials, labeled, and sent to the University of Kansas Isotope Geochemistry Laboratory for isotopic analysis by a VG Sector 54 mass spectrometer as detailed by Feuerbach et al. (1993). Powdered samples were also placed in plastic vials, labeled, and sent to Activation Laboratories LTD for rare-earth element (REE) analysis by ICP-MS.

The powdered samples were then analyzed for volatiles using a loss on ignition (LOI) technique. This process involves first weighing the ceramic crucible, and then the crucible plus ~16 g of sample. The sample and crucible are then heated at 110^{o}C overnight. The sample and crucible are then reweighed, heated at 950^{o}C for 2 hours, and weighed again. All values were recorded and used to determine the sample's LOI value.

Samples previously analyzed for LOI were then made into fusion disks for major element analysis. Fusion disks were made by weighing a graphite crucible, adding 0.72$\pm$0.0005 grams of sample powder, 7.2$\pm$0.0005 grams of 50% lithium metaborate/50% lithium tetraborate flux, and then stirring until homogenized. All values were recorded. The crucible, sample, and flux were then heated to 1050^{o}C for 10 minutes, removed and stirred, then heated and stirred at 5-minute intervals until the heating time totaled 30 minutes and/or the sample was completely dissolved. The crucible was then removed from the furnace and set on a metal plate until the molten sample solidified and cooled to room temperature. The resulting glass fusion disk was then removed from the crucible, the flat side ground down using a 30-micron diamond-grinding disk until all graphite was removed from the surface, and finally labeled. The disks were then cleaned with alcohol and run on a Panalytical Axios Advanced X-ray Fluorescence Spectrometer (XRF) for major elements. A standard, usually BCR-2, was run with each batch of 16 samples.

Sample powder previously analyzed for LOI was also made into pressed pellets for trace element analysis. The pressed pellets were made by weighing 12$\pm$0.0005 grams of sample powder and 3$\pm$0.0005 grams of binder (blending, binding and briquetting additive; spectroblend 44µ powder) into polystyrene vials. A small bead was added to each vial to aid in mixing samples. The vials were then shaken on a modified paint mixer for 2.5 minutes, flipped to face the opposite direction, and shaken for an additional 2.5 minutes in order to sufficiently homogenize the binder and sample powder. Each sample was then poured into the mount press mold, the mixing bead was removed, and the container was put under pressure on a Buehler Specimen Mount Press for 15 minutes. The pellet was then removed from the mold and the mold was cleaned using Kimwipes in preparation for the next sample. The pressed pellets were then labeled and analyzed for trace elements using the XRF.

Thin section billets were made by cutting ~0.5 inch unweathered sections of sample using a rock saw. The billets were labeled and sent to Quality Thin Sections in Tucson, Arizona to be made into thin sections.

Data

Major element data can be found in Appendix C, trace element data in Appendix D, REE data in Appendix E, and isotopic data in Appendix F.

Classification

The Pliocene volcanic rocks of the Greenwater Range are classified using the LeBas et al. (1986) diagram as trachybasalts and basalts to basaltic trachyandesites and basaltic andesites (Fig. 12) and vary from potassic alkaline (Fig. 13 and 14) to subalkaline calkalkalic (Fig. 13 and 15). Southeast Center, Smith's Climb and Secondary Vent, and the western end of Shoshone Ridge plot in the lower silica part of the basaltic trachyandesite field (Fig. 12). Tall Peak and its surrounding flows span the low silica end of the basaltic andesite and basaltic trachyandesite fields (Fig. 12). The flat lying basalts at the south end of Greenwater Canyon are basaltic andesites (Fig. 9, 12).

Major Elements

The volcanic rocks of the Funeral Formation in the Greenwater Range vary from 46.47 - 56.52 wt. % SiO_2 and in Mg# (Mg/(Mg+Fe)) from 40.6 – 64.4 (Fig. 16). In general, the volcanic rocks exhibit increases in Al_2O_3 and Na_2O and decreases in TiO_2, FeO, MgO, and P_2O_5 with increasing SiO_2 (Fig. 17). CaO and K_2O show flat slopes on Harker diagrams (Fig. 17). Samples from the different centers group together on most major element plots (Fig. 18).

Trace and Rare-Earth Elements

In general, the trace elements of the Greenwater Range basalt and basaltic andesite have an OIB signature (Fig. 19a) with the exception of negative Nb, Rb, and Ti anomalies and positive Cs, Ba, Th, La, and Pb. The slight negative Ti anomaly is obscured by the lack of data for some samples for surrounding elements, as such; it cannot be distinguished on the spider diagrams. Element concentrations range from 100 times chondrite for light REE to 10 times chondrite for heavy REE (Fig. 19b).

Several elements divide the basalt and basaltic andesites into two chemical groups. The initial separation into two groups was based on Nb concentration. A value of 20 ppm separates the low Nb from high Nb basalt. Additionally, Zr, Nd, Ce, Ta, and Pr (Fig. 20) concentrations are higher in the high Nb group and lower in the low Nb group (Fig. 20). Furthermore, on average, this grouping is seen in all trace and rare-earth elements as observed on OIB and chondrite normalized spider diagrams (Fig. 19). The grouping is seen to a lesser extent in the major elements. The high Nb group is lower in MgO and higher in TiO_2, FeO, and P_2O_5 (Fig. 17). Geographically, the high Nb basalt centers are in the northwestern part of the field and the low Nb centers are located in the southeast (Plate 1) (Fig. 21).

Isotopic Data

The basalts and basaltic andesites of the Greenwater Range exhibit low epsilon Nd (-2.38 to -12.89) and high $^{87}Sr/^{86}Sr$ (0.706113 to 0.707973) with an anomalous 0.709790 $^{87}Sr/^{86}Sr$ from the Lower Ridge. Considering basalts/basaltic andesites in the entire field, there is a trend of decreasing epsilon Nd with increasing $^{87}Sr/^{86}Sr$ (Fig. 22). Samples also display an increase in $^{206}Pb/^{204}Pb$ (17.764 to 18.573) with a slight increase in $^{207}Pb/^{204}Pb$ (15.512 to 15.603) from asthenospheric values (Fig. 24). All samples plot above the Northern Hemisphere Reference Line (NHRL). Due to lack of data for multiple samples from a single center, it is not possible to determine if the isotopic data show any grouping for the centers as they do in the major elements.

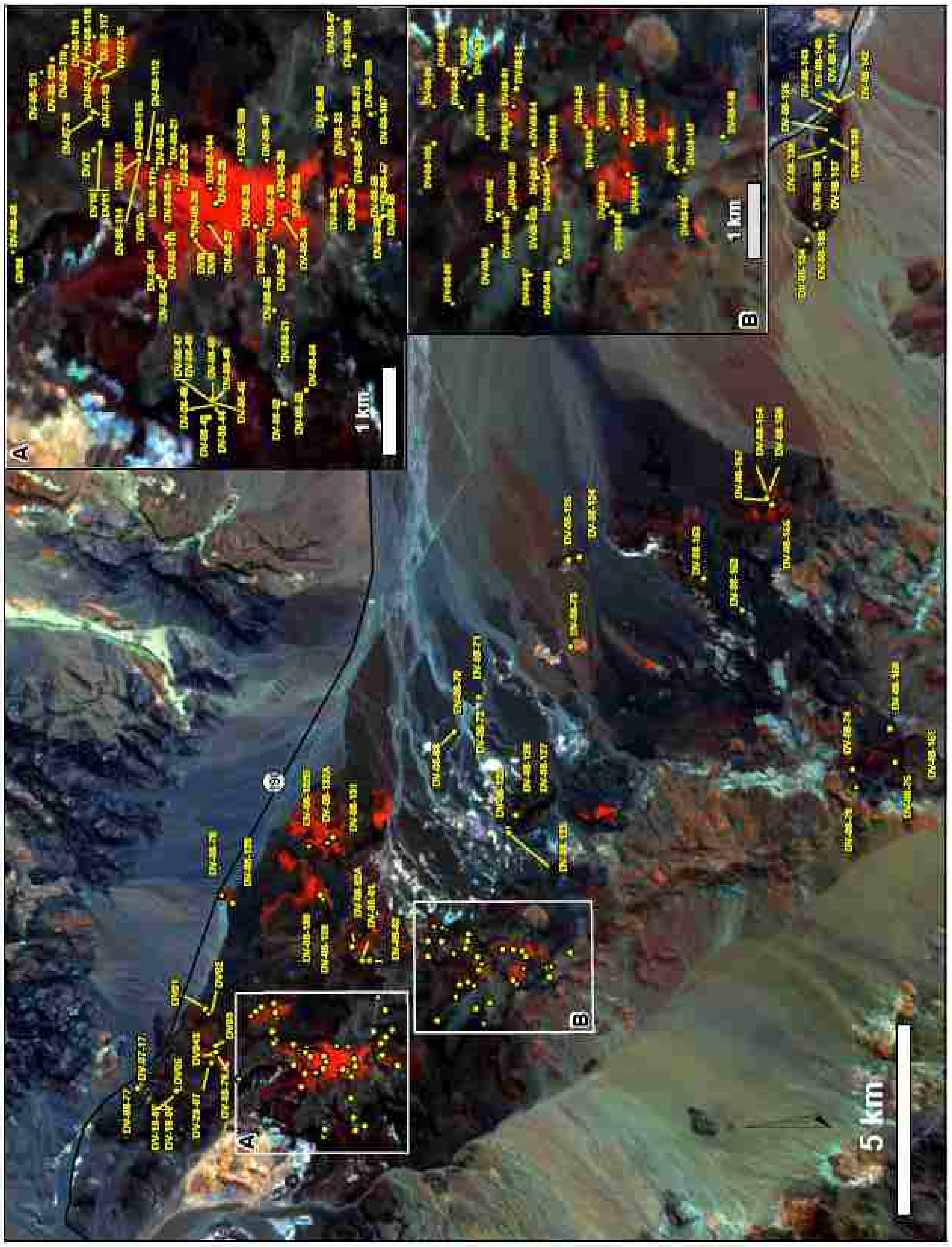

Figure 11: Greenwater Range sample locations.

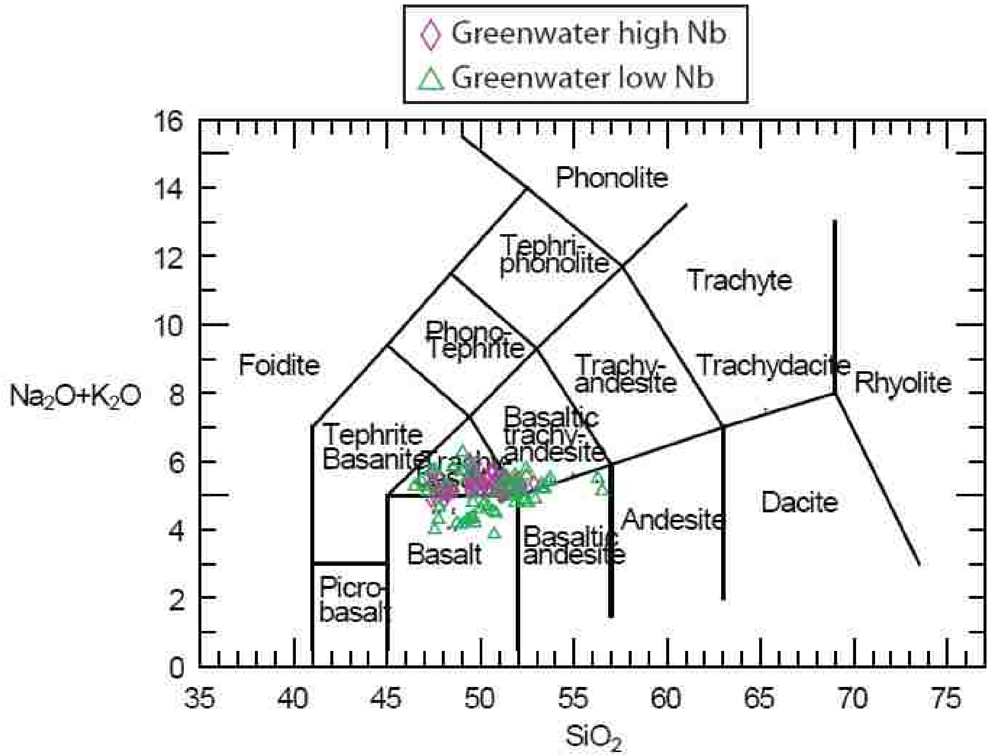

Figure 12: LeBas et al. (1986) rock classification diagram of Greenwater Range volcanic rocks. All chemical plots use Igneous Petrology for Windows software (Terra Softa Inc., 2000).

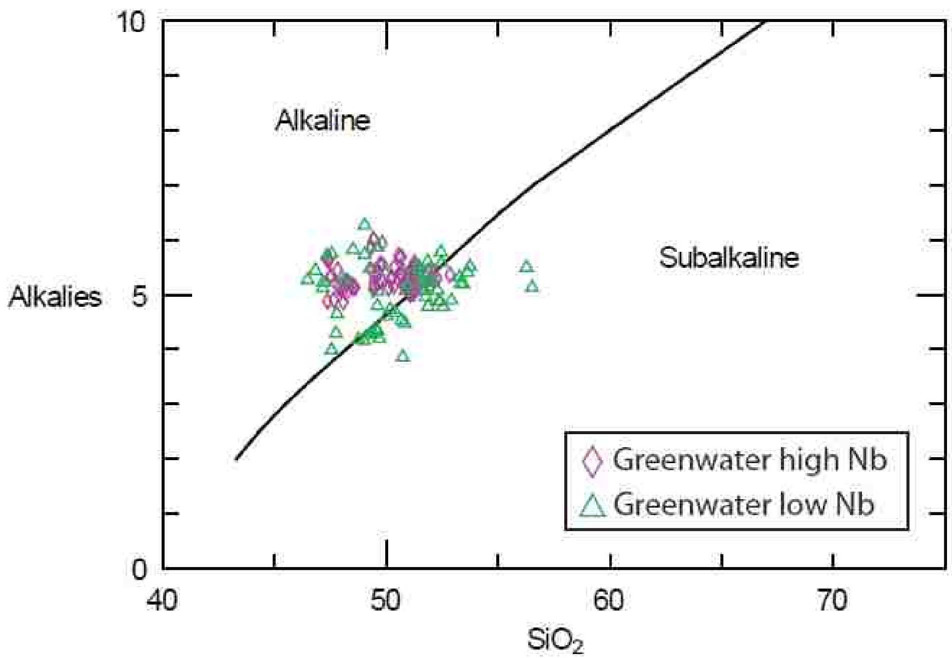

Figure 13: Alkaline vs. Subalkaline discrimination diagram for Greenwater Range volcanic rocks.

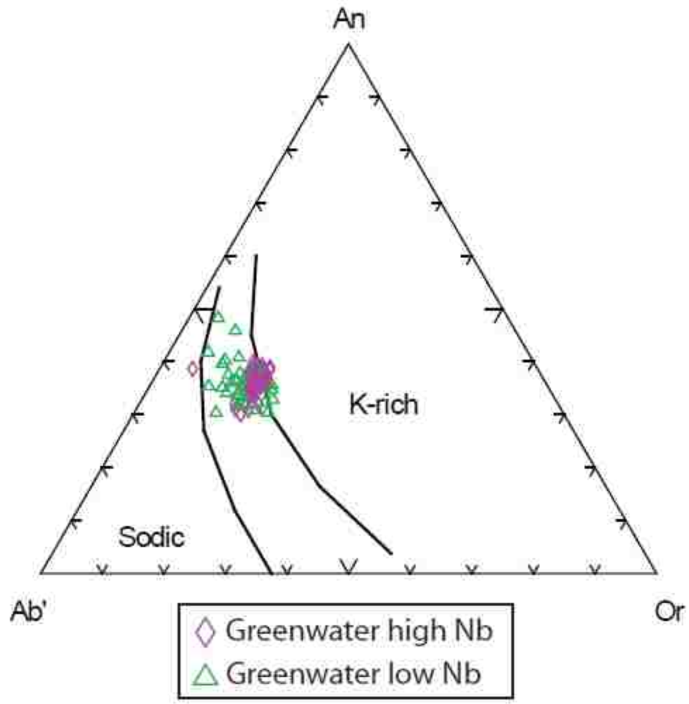

Figure 14: Potassium rich and poor vs. sodic classification diagram for alkaline Greenwater Range volcanics, showing rocks mainly plotting in the transitional K-Na field.

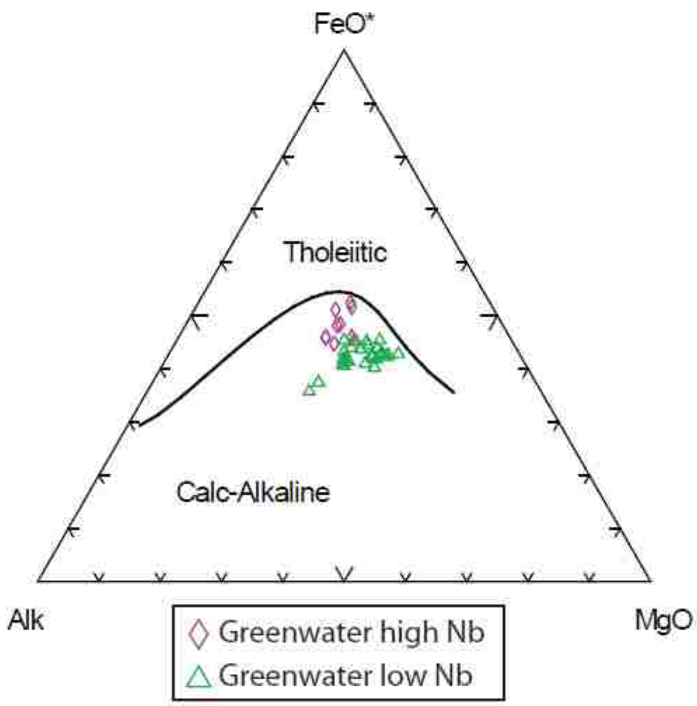

Figure 15: Tholeiitic vs. Calc-Alkaline discrimination diagram for subalkaline Greenwater Range volcanic rocks.

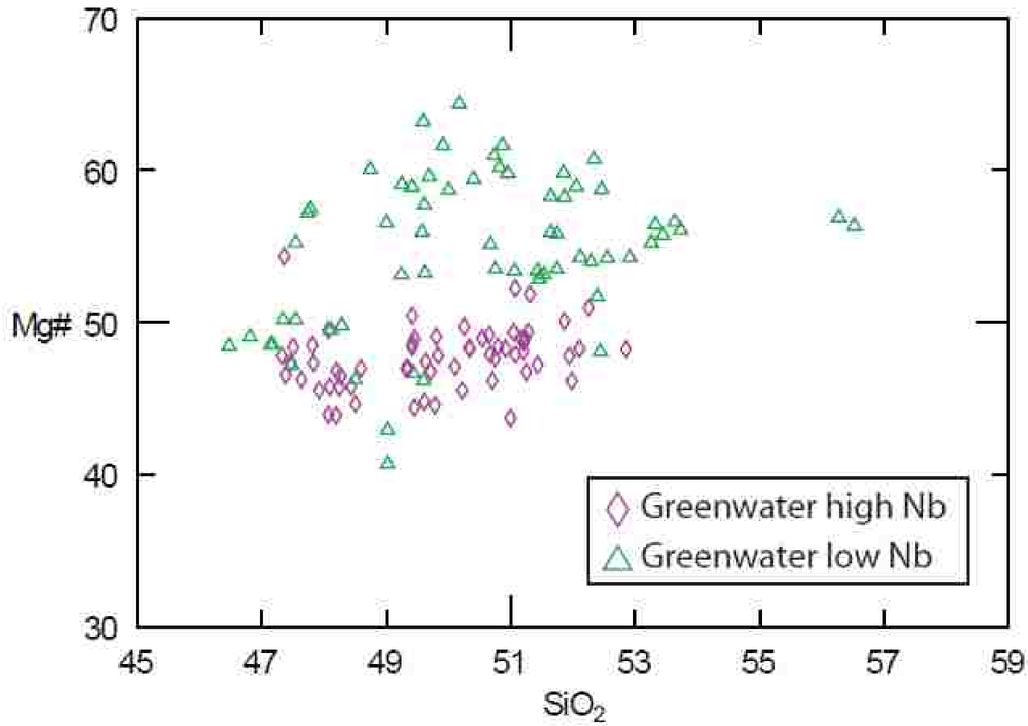

Figure 16: Mg# (Mg/(Mg+Fe)) vs. SiO_2 plot for Greenwater Range volcanics. Error bars are smaller than symbol size.

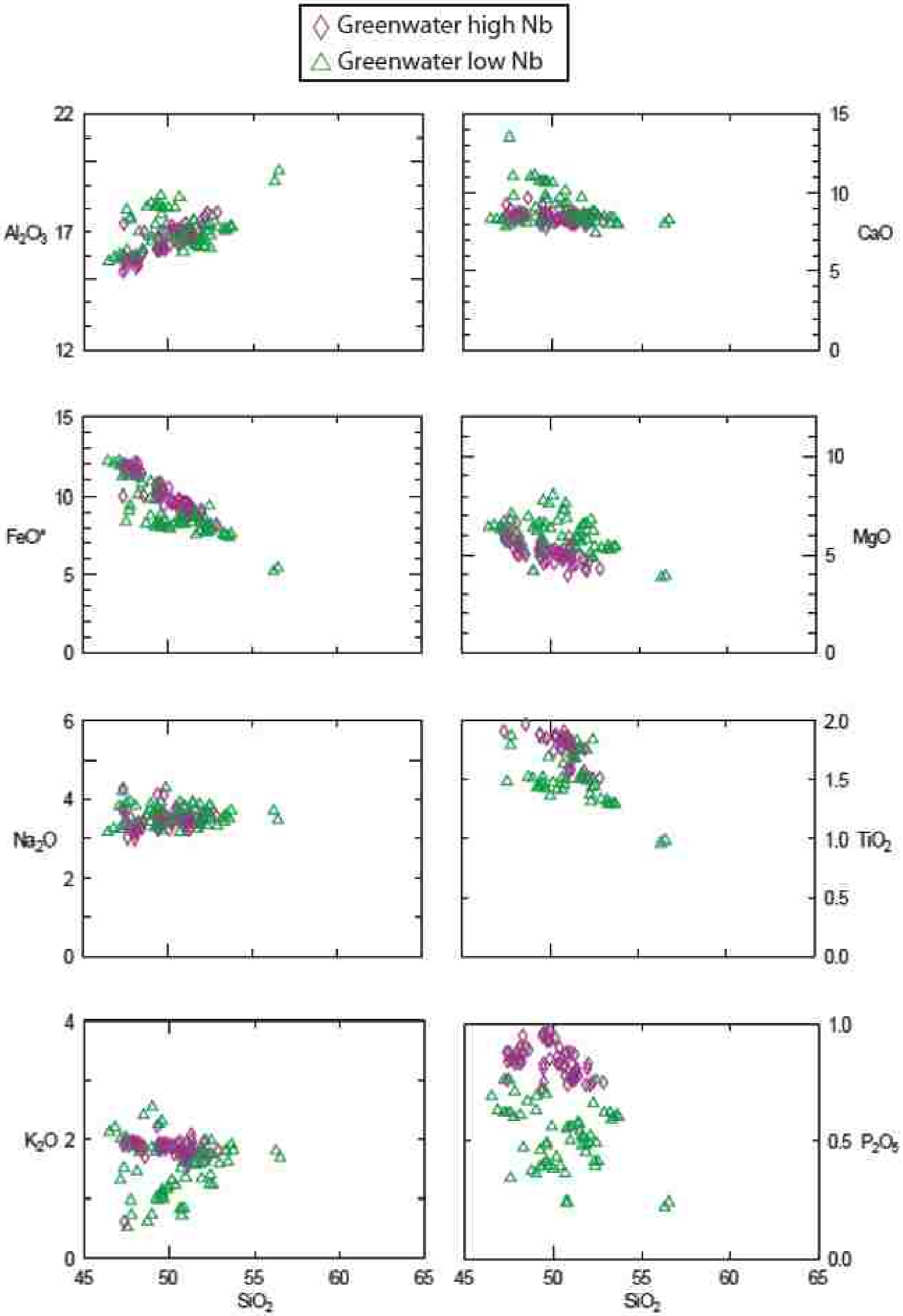

Figure 17: Harker variation diagrams for Greenwater Range volcanics. Error bars are smaller than symbol size.

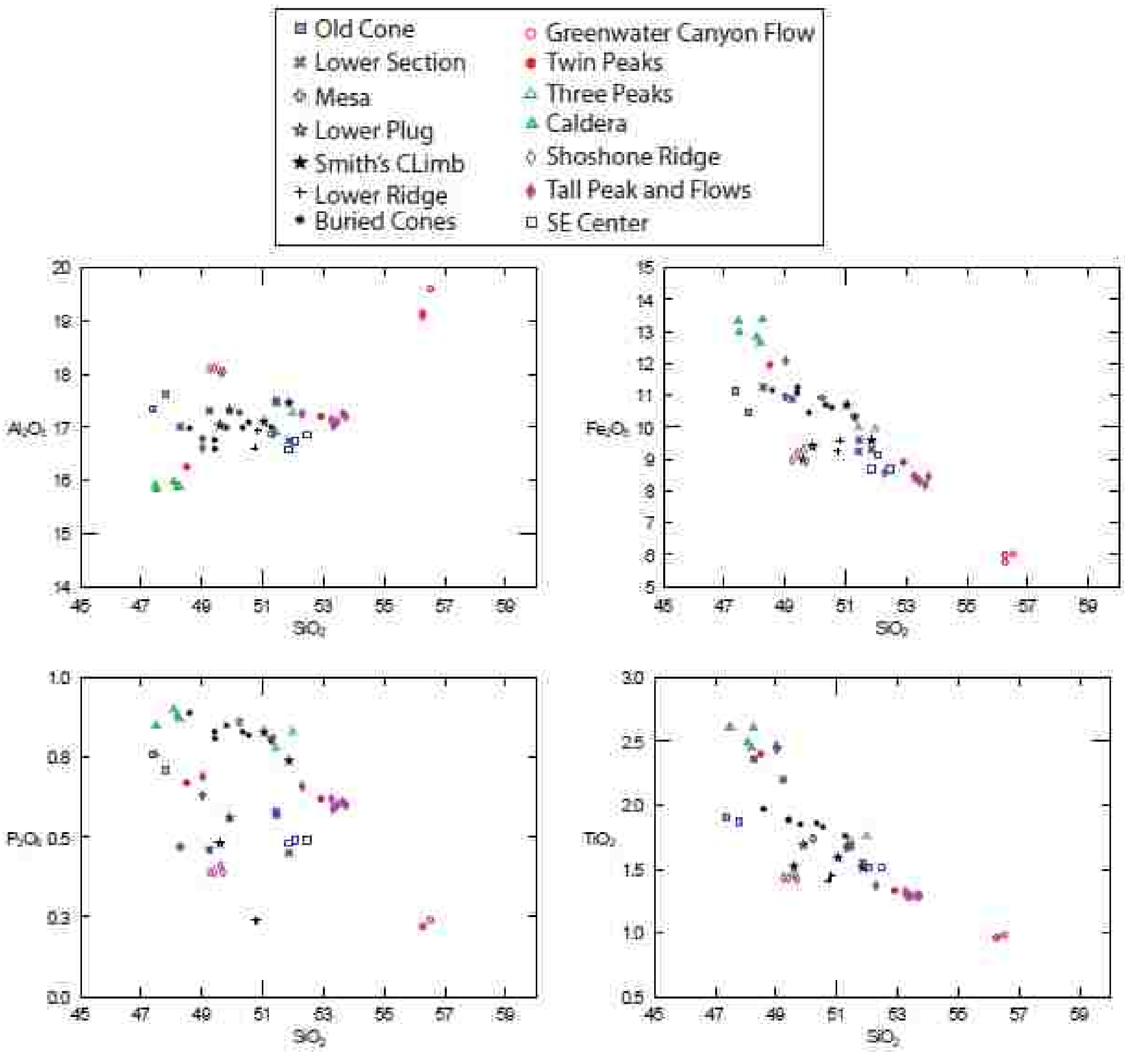

Figure 18: Major element plots for Greenwater Range centers. Error bars are smaller than symbol size.

A)

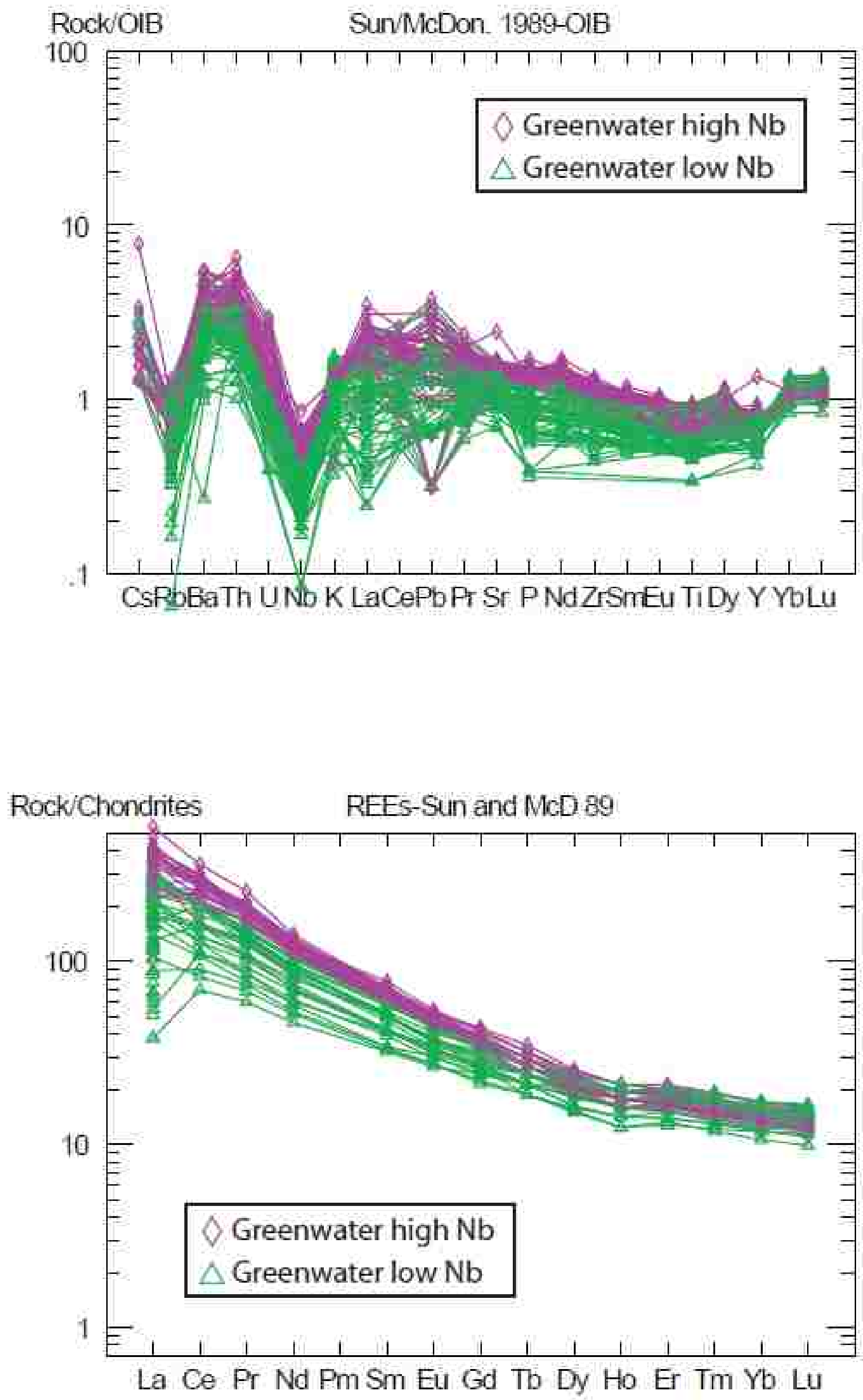

B)

Figure 19: A) OIB normalized spider diagram, B) Chondrite normalized spider diagram.

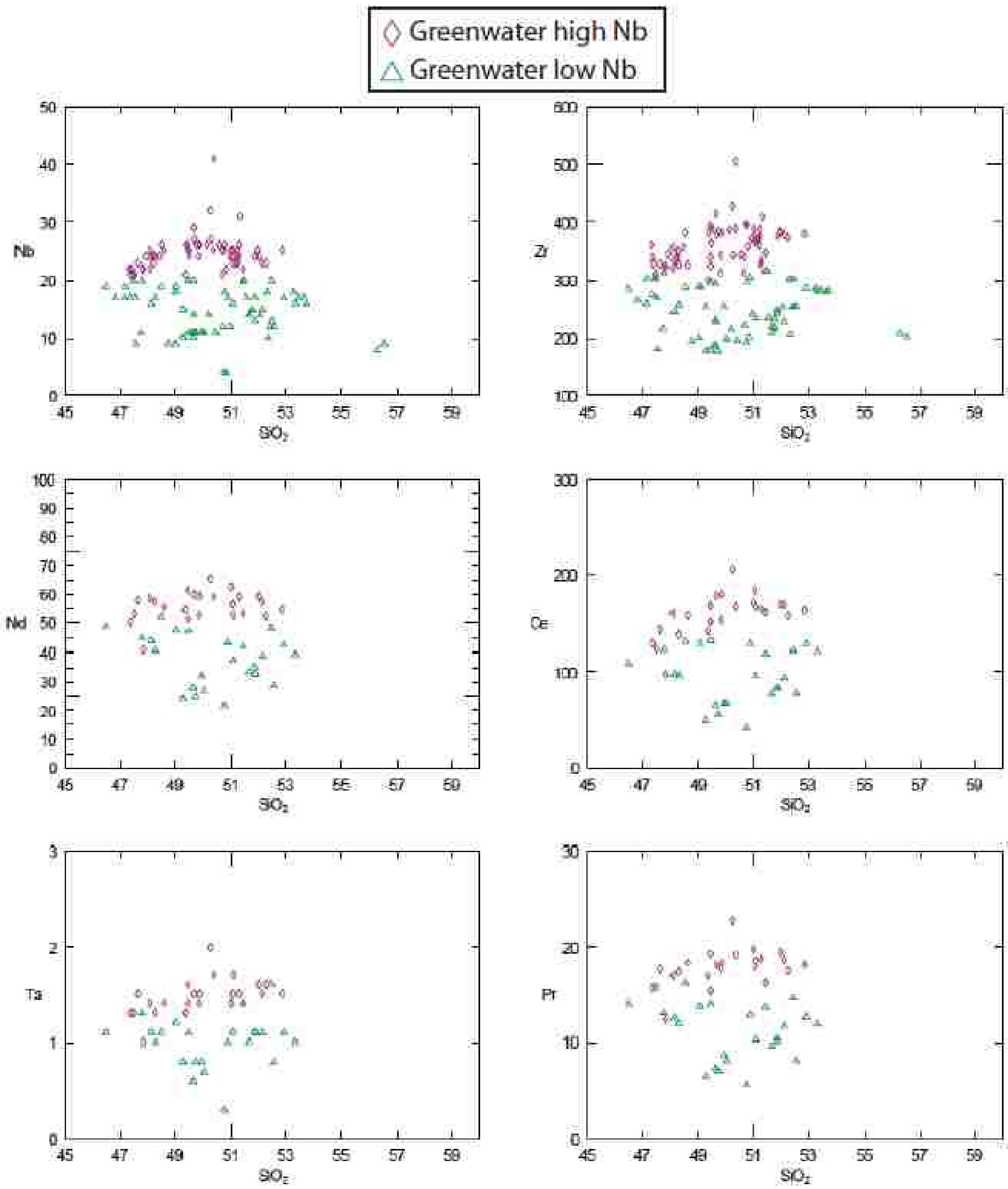

Figure 20: Trace element/REE vs. SiO_2 plots showing grouping of high and low Nb samples. Error bars are smaller than symbol size.

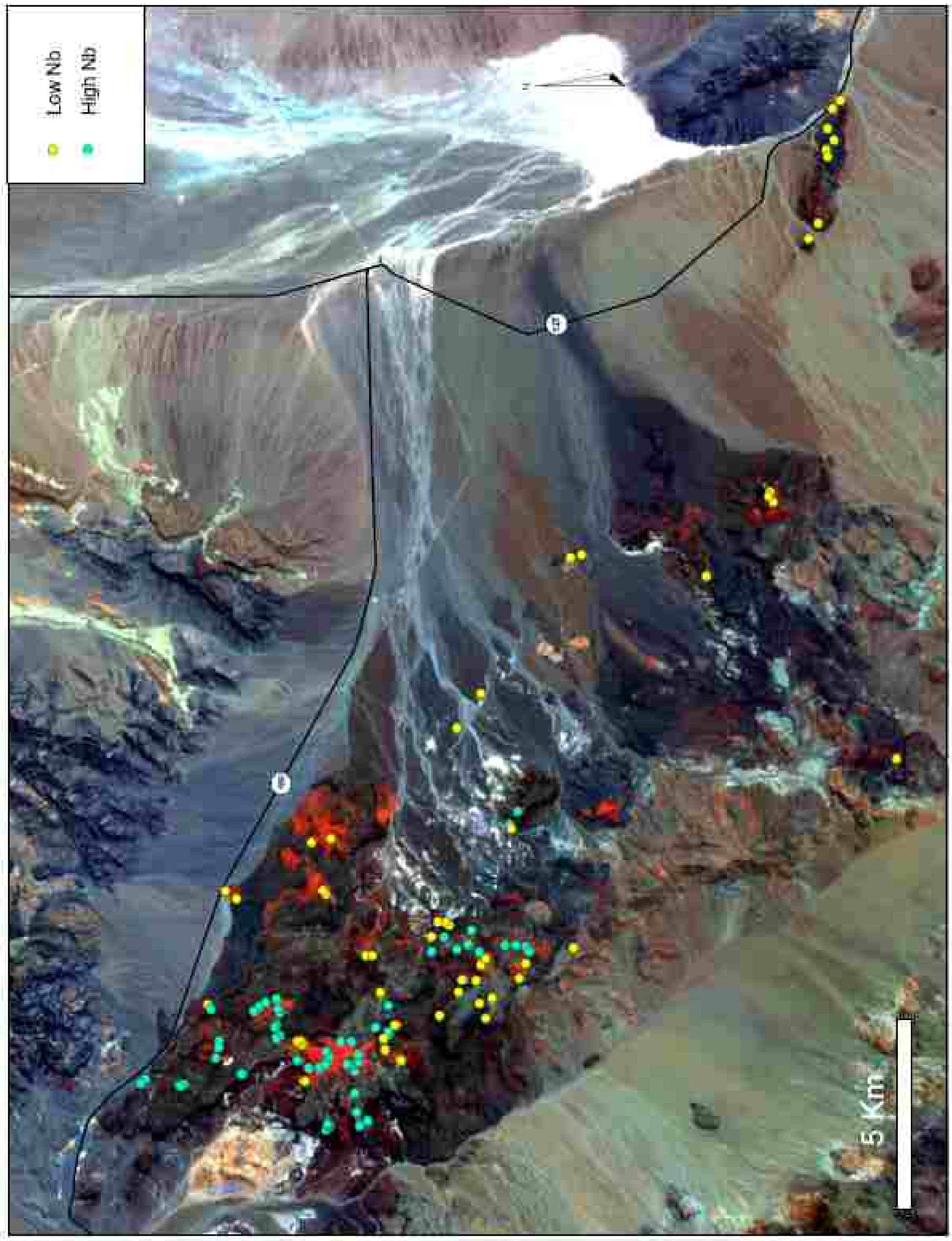

Figure 21: Distribution of high and low Nb samples. Yellow are low Nb and blue are high Nb.

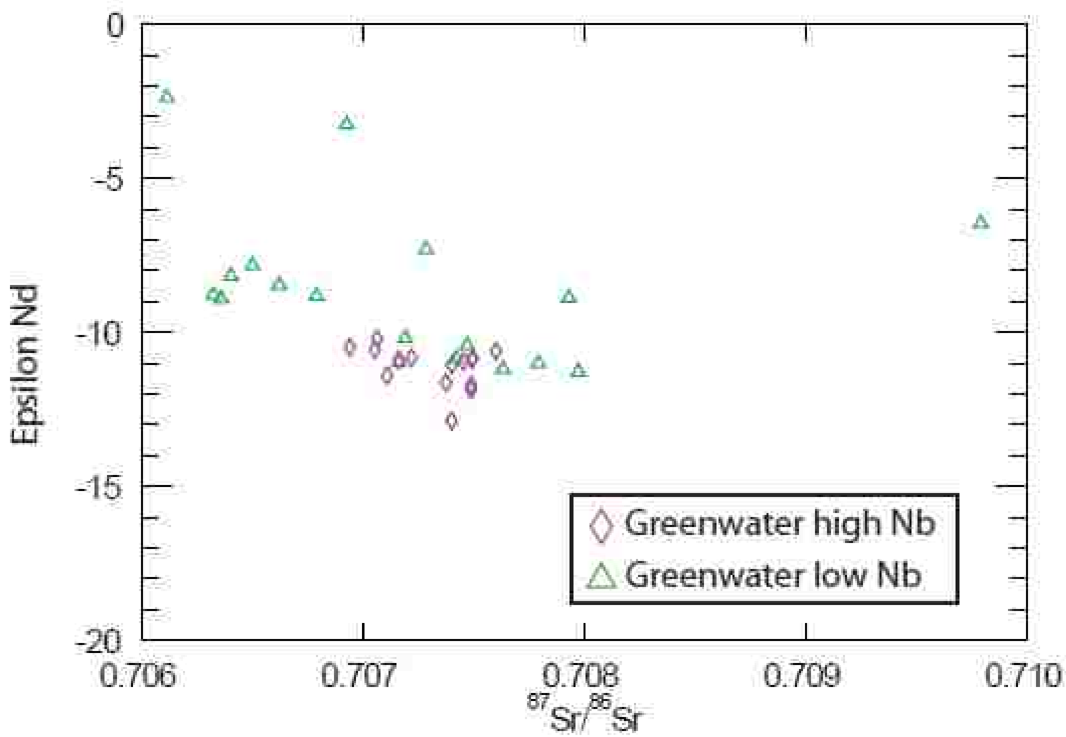

Figure 22: Epsilon Nd vs. $^{87}Sr/^{86}Sr$ plot of Greenwater Range volcanics. Compositional fields can be seen in Figure 33. Error bars are smaller than symbol size.

CHAPTER 4

DEPTH OF MELTING CALCULATIONS

Silica Barometer Method

Depth of melting for basalt and basaltic andesites in the Greenwater Range and Crater Flat volcanic fields were calculated using the silica barometer of Lee et al. (2009). Depth of melting for Crater Flat basalt was calculated to test the link between the Crater Flat and Greenwater volcanic fields (see Chapter 7). Use of this barometer requires that the source include olivine and orthopyroxene and that the basalts have > 40 wt. % SiO_2 and > 7.5 wt. % MgO (Lee et al., 2009). The presence of plagioclase results in a "slight (Lee et al., 2009)" overestimate of temperature and pressure. The presence of clinopyroxene results in an underestimate of pressure and overestimate of temperature (Lee et al., 2009).

The foundation of this barometer is that the activity of silica in basaltic melts is controlled by the reaction $Mg_2SiO_4^{ol} + SiO_2^{melt} = Mg_2Si_2O_6^{opx}$, which results in the activity of silica (SiO_2) being inversely proportional to the equilibrium constant at some pressure and temperature. The large molar volume change of this reaction results in silica activity being dependent on pressure, which allows for its use as a barometer. Most importantly, silica is a major element with limited sensitivity to compositional variations and does not act incompatibly. Previously basalt depths were calculated using an Fe-Na based barometer (Wang et al., 2002), but since Na acts as an incompatible element during partial melting and is mobile during subsequent alteration events, the Fe-Na barometer is not as accurate as the Si-barometer. The uncertainties involved with the silica barometer are ± 0.20 GPa (~7.5 km) for pressure and ± 3 % for temperature (Lee et al., 2009). The

Si-barometer is easy to apply because it requires only whole rock major element analysis reported as wt% oxides.

Results

Depths for the Greenwater Range and Crater Flat volcanic fields were calculated assuming dry melting, MgO > 7.5 wt.%, SiO_2 > 44 wt.%, Fe as 90% Fe^{2+}, and a conversion factor of 37.5 km/GPa.

Olivine is the only phenocryst present so there is no need to worry about over or under estimates due to the presence of plagioclase or clinopyroxene. Using these parameters the silica barometer gives the following results:

- Temperatures, pressures, and depths for the Greenwater Range: 1367 - 1435°C, 1.45 - 2.39 GPa, and 54.34 – 89.64 km.
- Temperatures, pressures, and depths Crater Flat: 1388-1415°C, 2.5-2.8 GPa (Plank, personal communication 2008), and 93.75 - 105 km.

Lithospheric depths for the Greenwater Range and Crater Flat are 45-50 and 70 km, respectively. These results are illustrated in Figure 23. These calculations indicate a 35.3 km melting column for the Greenwater Range, the top of which is 4 – 9 km below the base of the lithosphere. Crater Flat basalt has a 11 km melting column, the top of which is 24 km below the base of the lithosphere. Even given a 0.20 GPa (7.5 km) uncertainty the calculated depths place the melting in the asthenosphere for both volcanic fields. In addition to asthenospheric depths of melting, the associated melting temperatures are too hot to be lithospheric ($\leq$1100-1200°C) (Wang et al., 2002), once again implying asthenospheric melting (>1280°C) (McKenzie and Bickle, 1988).

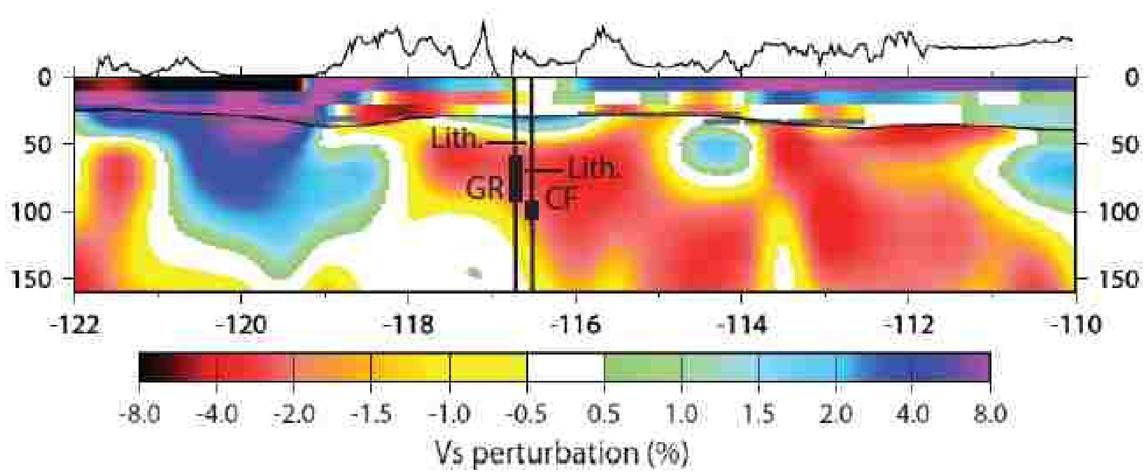

Figure 23: Seismic S- wave velocity profile constrained by ambient noise and earthquake tomography of the mantle (Yang et al., 2008) at 36.25 degrees latitude from -122 to -110 degrees longitude (Yang, personal communication). Vertical black lines represent longitudinal locations of the volcanic fields (-116.6^{o} Greenwater Range and -116.5^{o} Crater Flat), black rectangles represent melting columns (54.34 – 89.64 km Greenwater Range and 93.75 - 105 km Crater Flat), and horizontal black lines represent the approximate base of the lithosphere (47.5 km Greenwater Range and 70 km Crater Flat). Vs perturbation (%) is the percent difference between the measured Vs at each point on the profile and the mean Vs at the same depth.

CHAPTER 5

PETROGENESIS OF GREENWATER RANGE BASALTS

In this section a new model that accounts for most of the geochemical observations will be proposed. The models to be considered include: slab components from an old subduction zone, mixing of OIB and Archean lithosphere, and the feasibility of fractional crystallization (FC) and assimilation fractional crystallization (AFC). At the end of the chapter, the origin of the basaltic andesites by will be discussed.

Geochemical Observations

Any reasonable model for the Greenwater Range volcanics must take into account the observations made from field relations, chemistry, and petrography. These include the following:

1) Major element trends.

2) Presence of sedimentary xenoliths and quartz and feldspar xenocrysts in some volcanic centers.

3) Phenocryst and matrix content and abundances.

4) Deviations from OIB trace and rare-earth elements.

5) The two chemical groups are based primarily on Nb, but also on Zr, Nd, Ce, Ta and Pr.

6) Variations of Epsilon Nd, $^{87}Sr/^{86}Sr$, $^{207}Pb/^{204}Pb$, and $^{206}Pb/^{204}Pb$ from OIB signatures.

7) Composition of basement rock. Basalt primarily overlies sedimentary units of the Furnace Creek and Artist Drive Formations except in the southeast part of the field where it overlies the rhyolite of the Funeral formation and near the Southeast Center where a small volume flow overlies older basalt.

Evidence for asthenospheric and lithospheric components in the source

The basalts of the Greenwater Range display what can be interpreted as asthenospheric and lithospheric signatures as well as evidence for contamination. Therefore, any source model must account for the contrasting signatures and contamination as described in the following paragraphs.

Evidence for an asthenospheric component includes:

1. The OIB like signature with the notable exception of negative Nb, Rb, and Ti anomalies and positive Cs, Ba, Th, La, and Pb anomalies (Fig. 19a).
2. Depths of melting (54.34 – 89.64 km) below the base of the lithosphere (45-50 km) (Fig. 23).
3. Temperatures of melting (1367 - 1435^{o}C) too hot to be lithospheric.

Evidence for a lithospheric source includes:

1. Low epsilon Nd and high $^{87}Sr/^{86}Sr$ (Fig. 22).
2. $^{207}Pb/^{204}Pb$ and $^{206}Pb/^{204}Pb$ values that plot above the northern hemisphere reference line (NHRL) (Fig. 24).
3. Nb/La < 1.1 (0.2-0.9) indicating lithospheric influence (Fig. 25).
4. Exceptions to OIB signature including negative Nb, Rb, Ti and positive Cs, Ba, Th, La, and Pb anomalies (Fig. 19a).

Evidence of contamination of a mafic component includes:

1. Partially resorbed potassium feldspar and quartz xenocrysts and partially resorbed plagioclase xenocrysts.
2. Evolution trends in major elements including increasing Al_2O_3 with increasing SiO_2.
3. Evolution from basalt/trachybasalt to basaltic andesite/ basaltic trachyandesite.

Any model must, therefore, explain the paradox of depth of melting calculations indicating an asthenospheric source, while chemistry suggests a shallower source in the lithospheric mantle.

The Source of Greenwater Basalt

Several source and evolution models specifically for the Greenwater Range will now be discussed; including their strengths, weaknesses, how well they explain the observed chemistry, and how feasible they are given the regional structure.

Slab components from old subduction zones

The preferred model (Fig. 26) for the source of basalts of the Greenwater Range involves old subducted slab components and fluids melted and emplaced in the lithosphere during a previous subduction event under the Death Valley region (Fig. 26a). This could include slab material as well as oceanic sediment from the top of the slab. In order for these slab components to display a significantly old lithospheric isotopic signature, they would need sufficient time for their original asthenospheric isotopic signature to evolve. This requires that the slab components be at least 1 billion years old. The Proterozoic age limits the slab source to western US orogenies such as the Ivanpah orogeny (1710-1700 Ma) in the Mojave province (Wooden and Miller, 1990), the Yavapai orogeny (1700 Ma) in the mid to southwestern US, and the Mazatzal orogeny (1660-1600 Ma) in the mid to southwestern US (Jones, 2009).

After being isolated in the lithosphere for about 10^9 years, the base of the lithosphere, including the old slab components, may have been thermally and mechanically, but not chemically, converted to asthenosphere by the following process.

The Farallon Slab underwent flat subduction beneath the western US from 70 to 45 Ma and rollback from 35 to 20 Ma (Fig. 27) (Zandt et al., 1995). As the Farallon slab moved from under the area, the asthenosphere rose into the gap to fill the space the slab previously occupied. The added heat of the asthenosphere would cause the local geothermal gradient to rise. In addition to this process, thinning of the lithosphere due to Basin and Range extension caused additional upwelling and a rise in the geotherm. The overall result of this heat input may be a thermal and mechanical, but not chemical, conversion of the base of the lithosphere to asthenosphere (Fig. 26b). A similar process was described by Perry et al. (1988) to explain chemical changes in basalt in the Rio Grande Rift.

A partial melt of the mixture of lithospheric mantle peridotite, asthenospheric mantle, and pockets of old slab components (Fig. 26c) would result in basaltic melt that crystallizes olivine, and plagioclase at shallower depths. These basalts would have an overall OIB trace element signature (Fig. 19a) but be modified by the slab component to show negative anomalies in the high field strength elements such as Nb and Ti, and positive Ba and Th anomalies. The oceanic sediment subducted with the slab might result in a positive Pb anomaly. The oceanic sediments would also account for the position of the $^{207}Pb/^{204}Pb$ and $^{206}Pb/^{204}Pb$ above the northern hemisphere reference line in the oceanic sediment field (Fig. 24). These variations from OIB signature would explain the variations seen in the Greenwater basalts.

The two chemical groups of basalt (high and low Nb) can be explained by the degree of partial melting. Smaller degrees of melting result in the enrichment of incompatible elements such as Nb, Zr, Nd, Ce, Ta, and Pr in the melt phase (Fig. 20).

This is supported by the overall higher trace element abundances for the high Nb group and lower trace element abundances for the low Nb group (Fig. 19). The low and high Nb groupings display a spatial trend, but do not correlate with stratigraphy (i.e. high Nb is over and underlying low Nb). From these observations it can be postulated that the degree of melting oscillated between higher and lower degrees of melting over time, but smaller degree melts were produced more frequently in the northwestern part of the field and higher degree melts were produced more frequently in the southeastern part of the field.

The more evolved basaltic andesites of the Greenwater Range have the same overall OIB trace element (Fig. 28) signature with the same positive and negative anomalies and the same isotopic signatures (Fig. 29, 30) as the basalts. Major elements concentrations are similar except that the basaltic andesites are higher in SiO_2 wt. % (Fig. 31). There are several possible relationships between the basalt and basaltic andesites.

Contamination of basalt to produce basaltic andesite: Contamination is a poor explanation of the cause of the more evolved samples because enough contamination to add several percent silica would likely change the trace and isotopic signatures.

Fractional Crystallization and Assimilation-Fractional Crystallization: FC and AFC are also a poor fit because there is no direct relationship between chemistry and any index of differentiation.

Different degrees of partial melting: Varying amounts of partial melting is postulated to result in the high and low Nb grouping. However, the difference between basalt and basaltic andesite would require a larger difference in the degree of melting than that required for the change from high to low Nb grouping. Note that there are both low and high Nb basaltic andesites as well as low and high Nb basalts (Fig. 32). This raises the possibility that the difference between high and low Nb groups may be related to source chemistry as well as the degree of partial melting.

An advantage of the "slab components from old subduction zones" model is that it explains the paradox between depth of melting calculations and chemistry. Depth of melting calculations place the source in the asthenosphere, but chemistry suggests shallower melting in the lithosphere. Melting a mixture of lithosphere converted to asthenosphere but retaining lithospheric chemistry and mixing it with an OIB type asthenospheric source at asthenospheric depths is consistent with both calculated melting depths and chemistry.

<u>OIB and lower Archean lithosphere mixing</u>

A modified version of the preferred model involves the melting of asthenospheric peridotite and the mixing of this melt with Archean lithosphere converted thermally and mechanically to asthenosphere. A partial melt of this mixture would create a basaltic liquid with an overall OIB trace element signature (Fig. 19a). The melt would inherit the low epsilon Nd, high $^{87}Sr/^{86}Sr$ and trace-element signature of the Archean component. The observed epsilon Nd and $^{87}Sr/^{86}Sr$ of the Greenwater Range basalts (Fig. 22) that fall between OIB and Archean values as well as $^{207}Pb/^{204}Pb$ and $^{206}Pb/^{204}Pb$ values that plot above the NHRL (Fig. 24) might also be explained. The Archean component would have to be mafic to produce a basaltic partial melt.

A reasonable OIB-like asthenospheric component for which data are well known and that occurs close to Death Valley is basalt from the Lunar Crater volcanic field in central Nevada. The closest possible Archean end-member is represented by peridotite xenoliths in the Cima Volcanic field located just 100 km to the south (Luffi et al., 2009). Cima xenoliths were found to have temperatures between 911-1055^{o}C and depths of ~32-42 km (Luffi et al., 2009) indicating a location in the lower lithosphere. However, the chemical data necessary to produce a mixing curve are not available for the Cima samples, so Archean data from harzburgite from Wyoming were used as a substitute. This sample is not ideal for modeling. However, since data for Archean mafic rock is scarce in the western US, it the best that can be done.

A mixing curve for Lunar Crater basalts and Archean lithosphere based on Epsilon Nd and $^{87}Sr/^{86}Sr$ plots just below the Greenwater Range data (Fig. 33). Greenwater Range basalts can be approximately produced by 20% mixing of Archean lithosphere with Lunar Crater OIB type asthenospheric melt. This is, however, a large amount of contamination and, although it may account for the isotopic signature, the affect of Archean contamination on the trace-element signature is unknown because trace element data is not available for this Archean sample. Also, it is not known if there is indeed Archean lithosphere under Death Valley, though there are xenoliths nearby in the Cima volcanic field that have been dated by the Re-Os technique as Archean (Lee et al., 2000). Even if there is some Archean lithosphere below Death Valley there would have to be a considerable amount to contribute 20% for the mixing model. If there were this much Archean lithosphere under Death Valley, it would likely be observed in xenoliths in the area.

Based on the discussion above, the Archean contamination model is not favored, mainly because it is unknown whether or not Archean basement exists beneath the Greenwater Range.

Origin of Evolved Magmas

Fractional crystallization and assimilation-fractional crystallization

An important question is whether basalts of each center are related to each other by a fractional crystallization (FC) or assimilation fractional crystallization (AFC) process. FC and AFC usually result in coherent chemical trends from primitive to evolved, but Greenwater chemistry forms a scattered data set that does not correlate with any index of differentiation (e.g., SiO_2 or Mg#) (Fig. 34). The most primitive sample, based on SiO_2 and Mg#, plots towards the middle of the group on trace-element plots and the basaltic andesites are scattered throughout the basaltic compositions (Fig. 34). Furthermore, isotopic ratios show considerable variation (Fig. 29) rather than the grouping that would be produced by a pure FC process. Due to these basic problems with data distribution it is concluded that FC and AFC models are unreasonable models for the Greenwater Range. Individual basalt centers probably represent independent magma batches. The basalts of the Greenwater Range, although cogenetic, are not comagmatic.

There is considerable petrographic evidence for crustal contamination of basalt. Xenocrysts such as quartz and feldspar can be explained by the entrainment of crystals from country rock during magma ascent. Small amounts of entrainment would not change the chemical composition. Sedimentary xenoliths are believed to be ripped up from the underlying sedimentary layers of the Furnace Creek and Artist Drive Formations but the magmas cooled before the xenoliths could be assimilated.

Summary

- The slab components from old subduction zones model produces the overall observations for the basalts and is the preferred model.
- Neither fractional crystallization nor assimilation-fractional crystallization models are reasonable due to trace and isotopic data distribution.
- The OIB asthenospheric melt mixing with Archean lithospheric melt model has too many problems and cannot reliably produce the observed chemistry under the known conditions of the area.
- A change in degree of melting for the preferred model can produce the high and low Nb groups and perhaps the less voluminous basaltic andesites. It is possible that the high and low Nb groups may reflect source composition as well as the degree of partial melting.

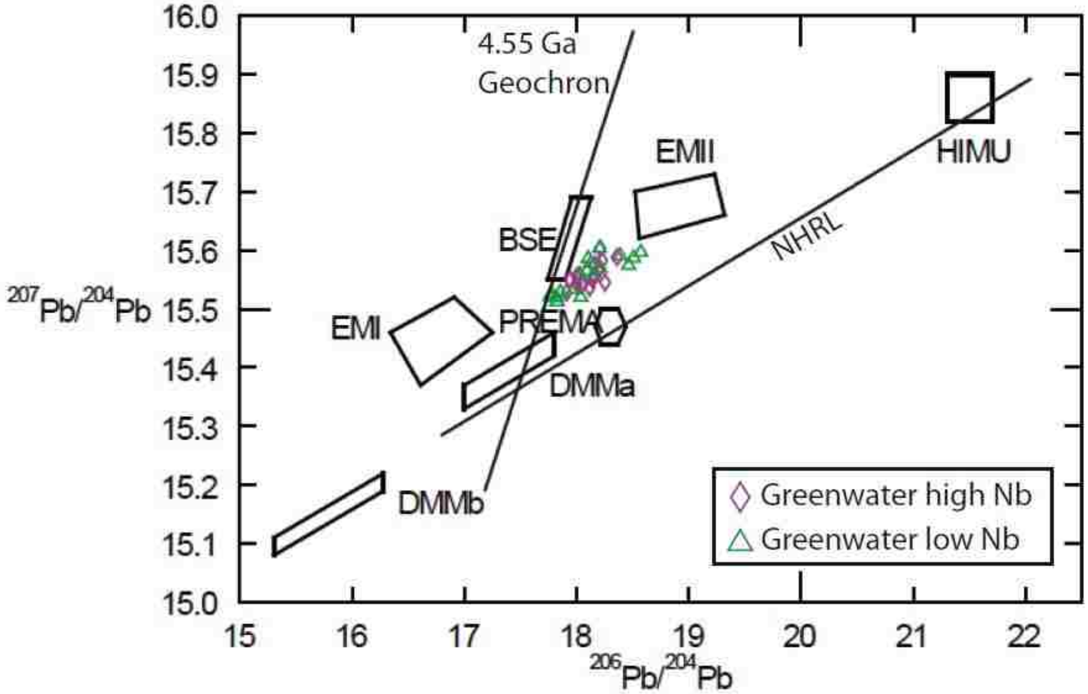

Figure 24: $^{207}Pb/^{204}Pb$ vs. $^{206}Pb/^{204}Pb$ plot Greenwater Range volcanic section. NHRL and Geochron from Wilson (2001). Error bars are smaller than symbol size.

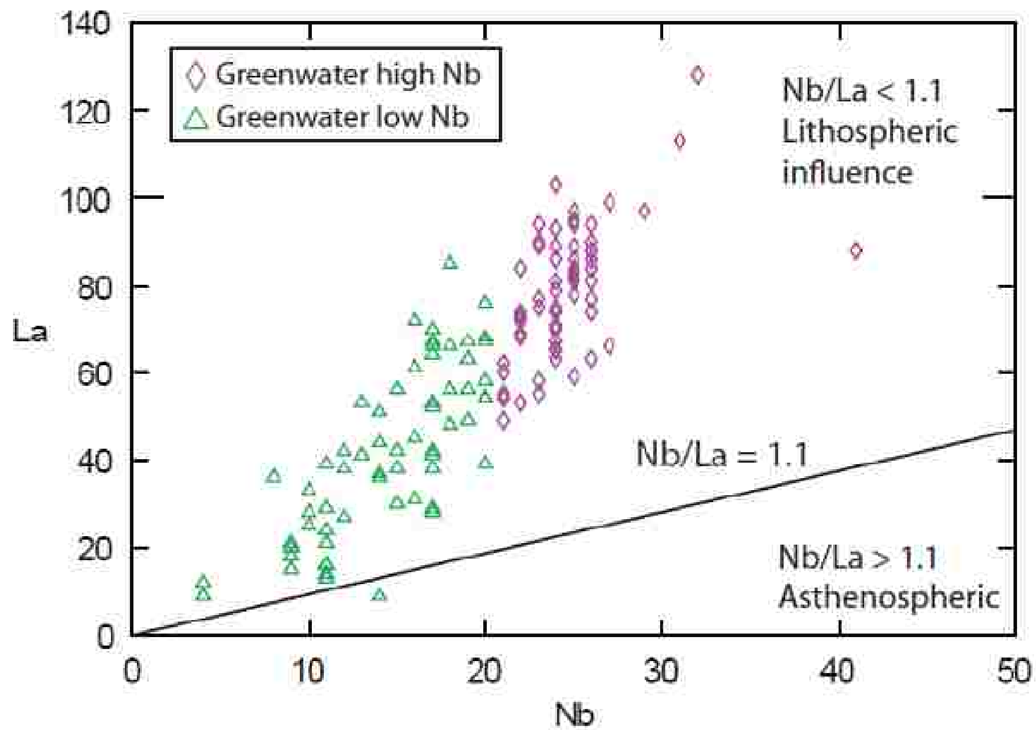

Figure 25: La vs. Nb plot showing the Nb/La =1.1 line, where Nb/La > 1.1 indicates lithospheric influence. Error bars are smaller than symbol size.

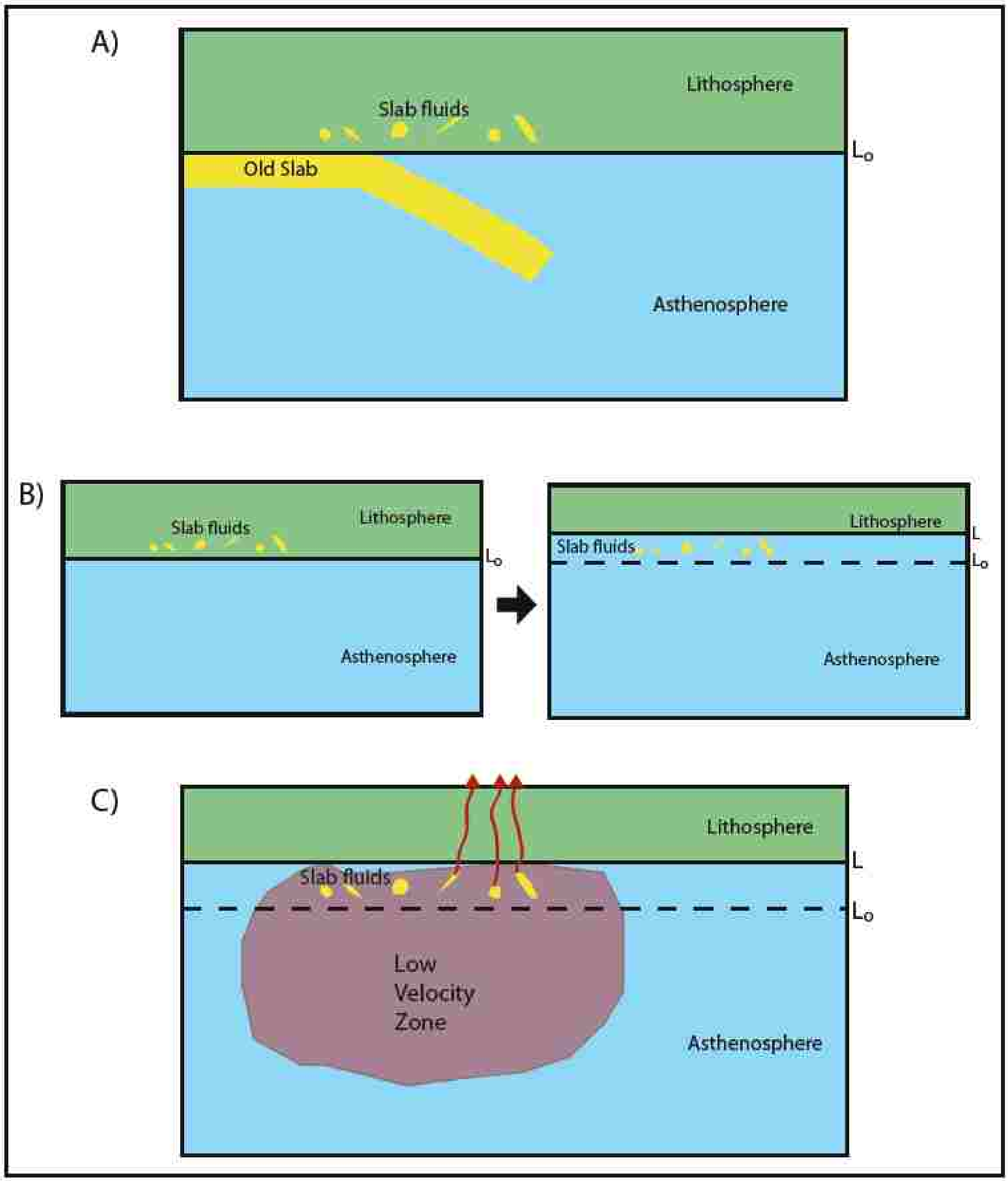

Figure 26: Cartoon of the preferred source model. A) Emplacement of slab components/melt in the base of the lithosphere during an old subduction event. B) Mechanical and thermal, but not chemical conversion of the base of the lithosphere to asthenosphere due to added heat from asthenospheric upwelling. C) Melting of old slab components in an asthenospheric low velocity zone.

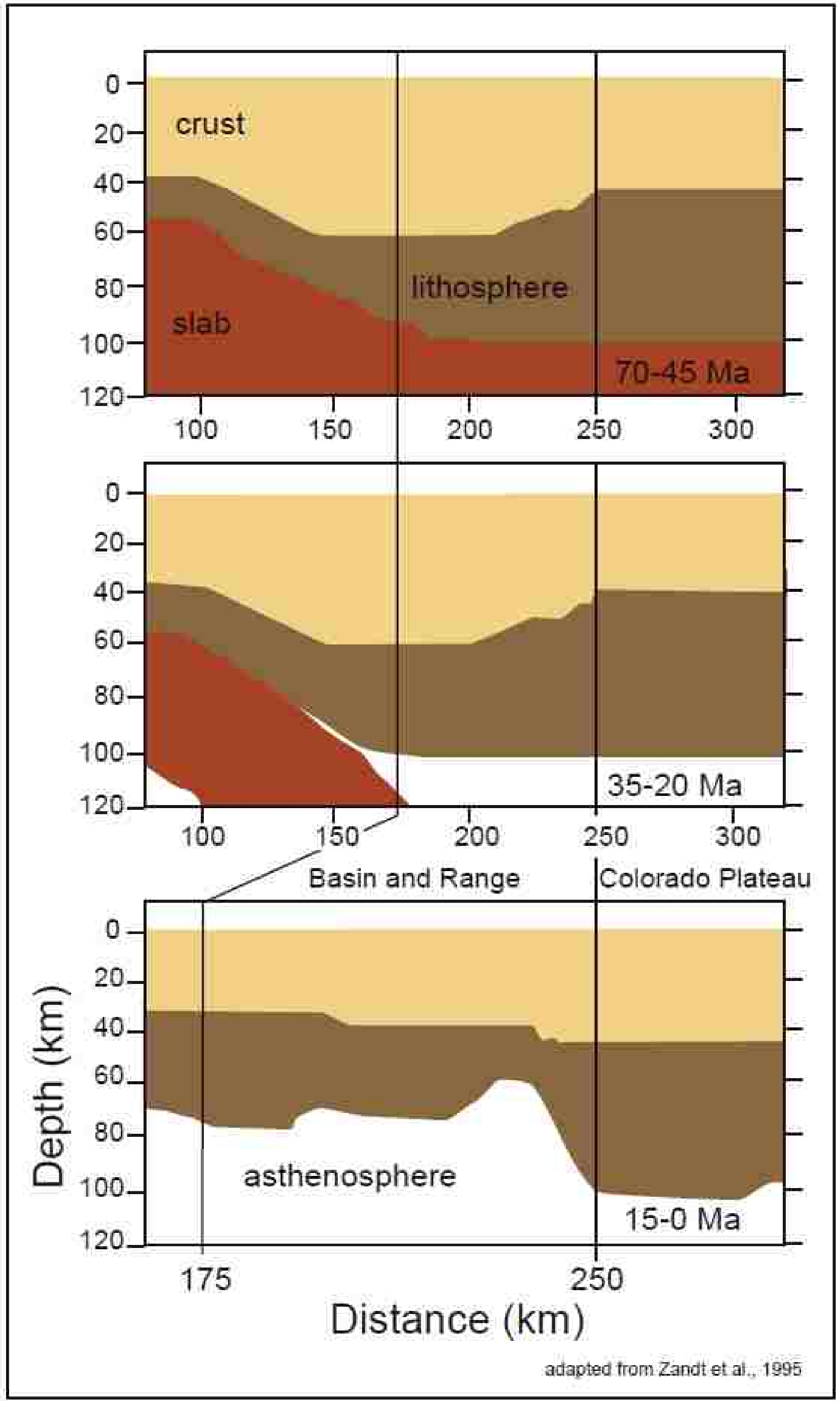

Figure 27: Movement of Farallon slab from under the Death Valley area creating a slab window (after Zandt et al., 1995).

A)

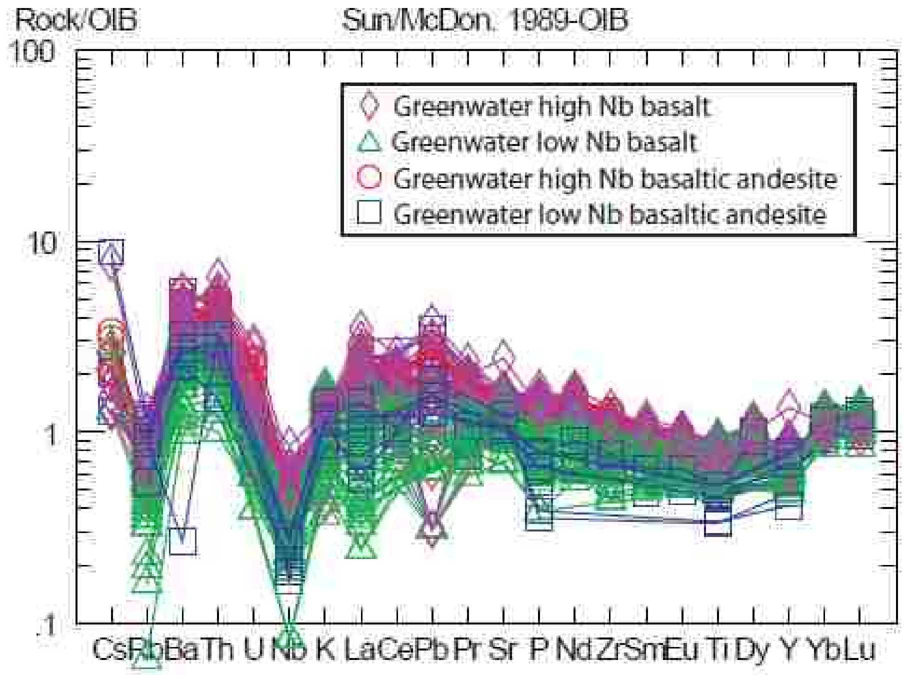

B)

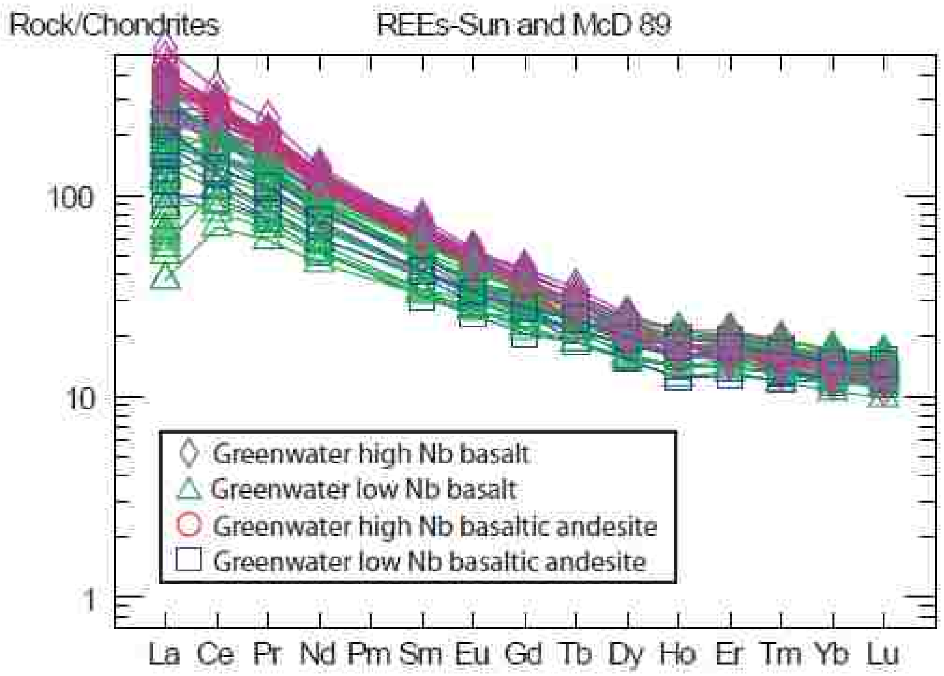

Figure 28: A) OIB normalized spider diagram, B) Chondrite normalized spider diagram.

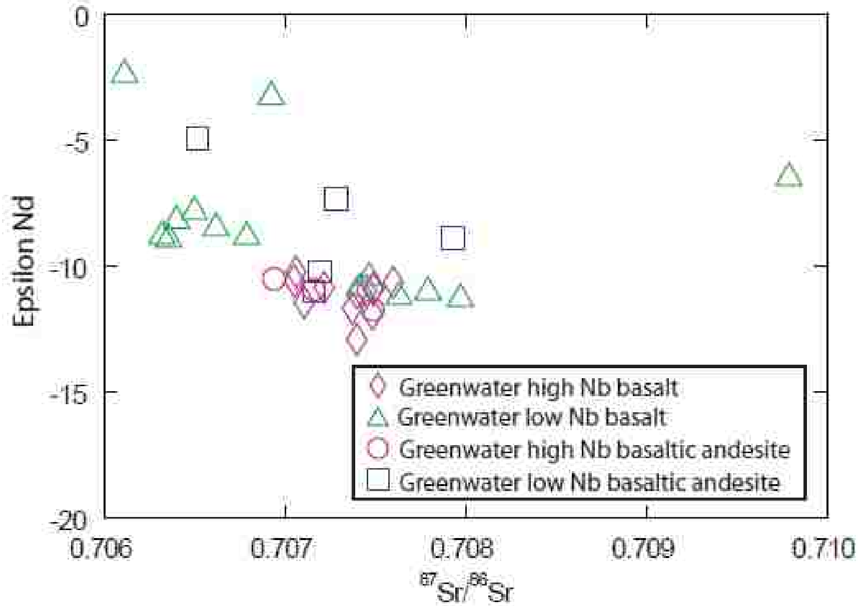

Figure 29: Epsilon Nd vs. $^{87}Sr/^{86}Sr$ plot for Greenwater Range basalts and basaltic andesites. Compositional fields can be seen in figure 33. Error bars are smaller than symbol size.

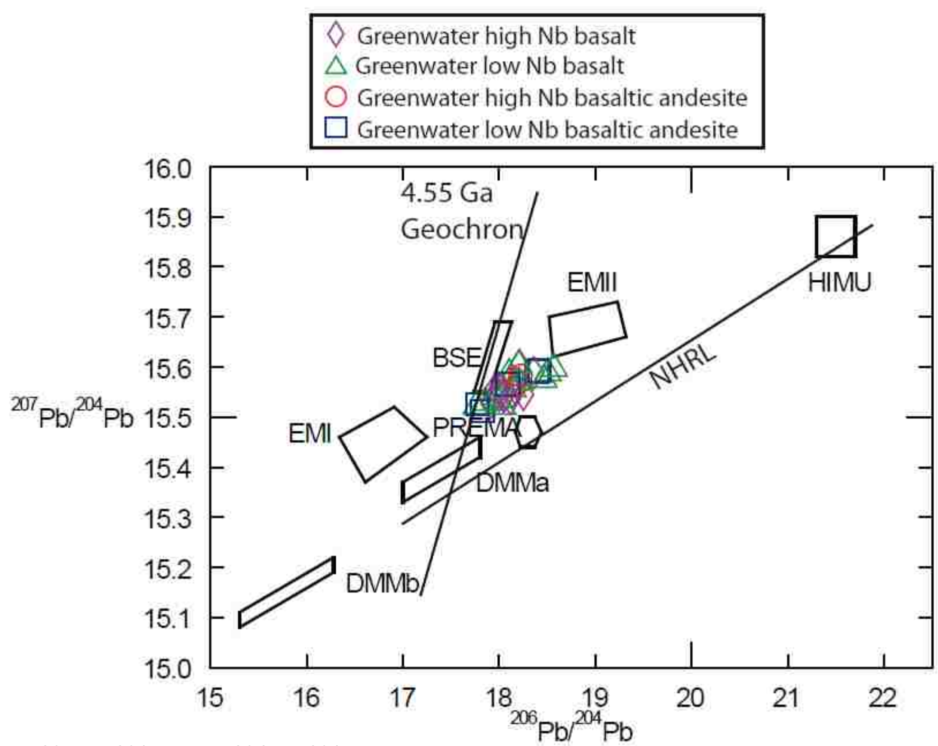

Figure 30: $^{207}Pb/^{204}Pb$ vs. $^{206}Pb/^{204}Pb$ plot Greenwater Range basalts and basaltic andesites. NHRL and Geochron from Wilson (2001). Error bars are smaller than symbol size.

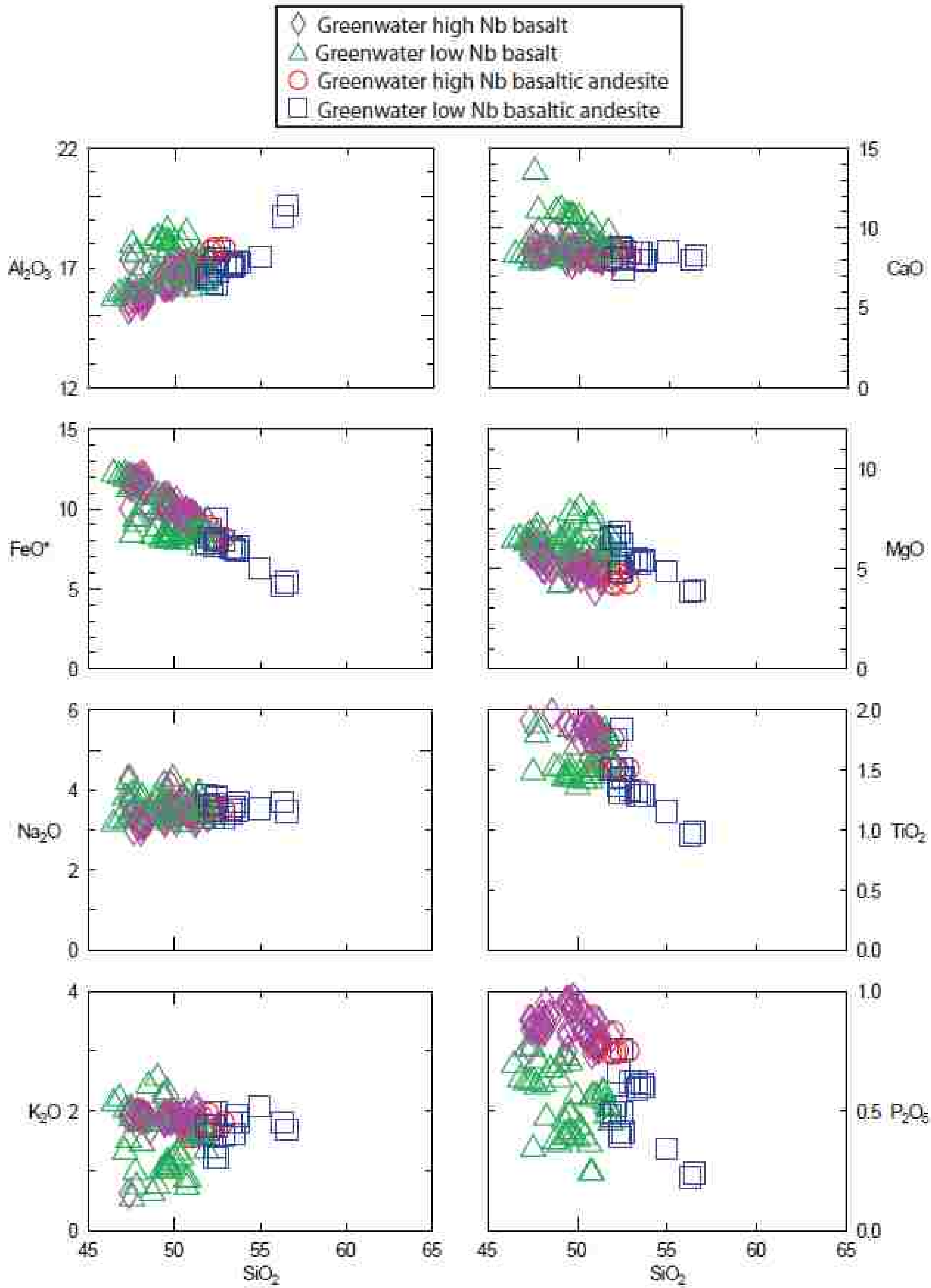

Figure 31: Harker variation diagrams for Greenwater Range basalts and basaltic andesites. Error bars are smaller than symbol size.

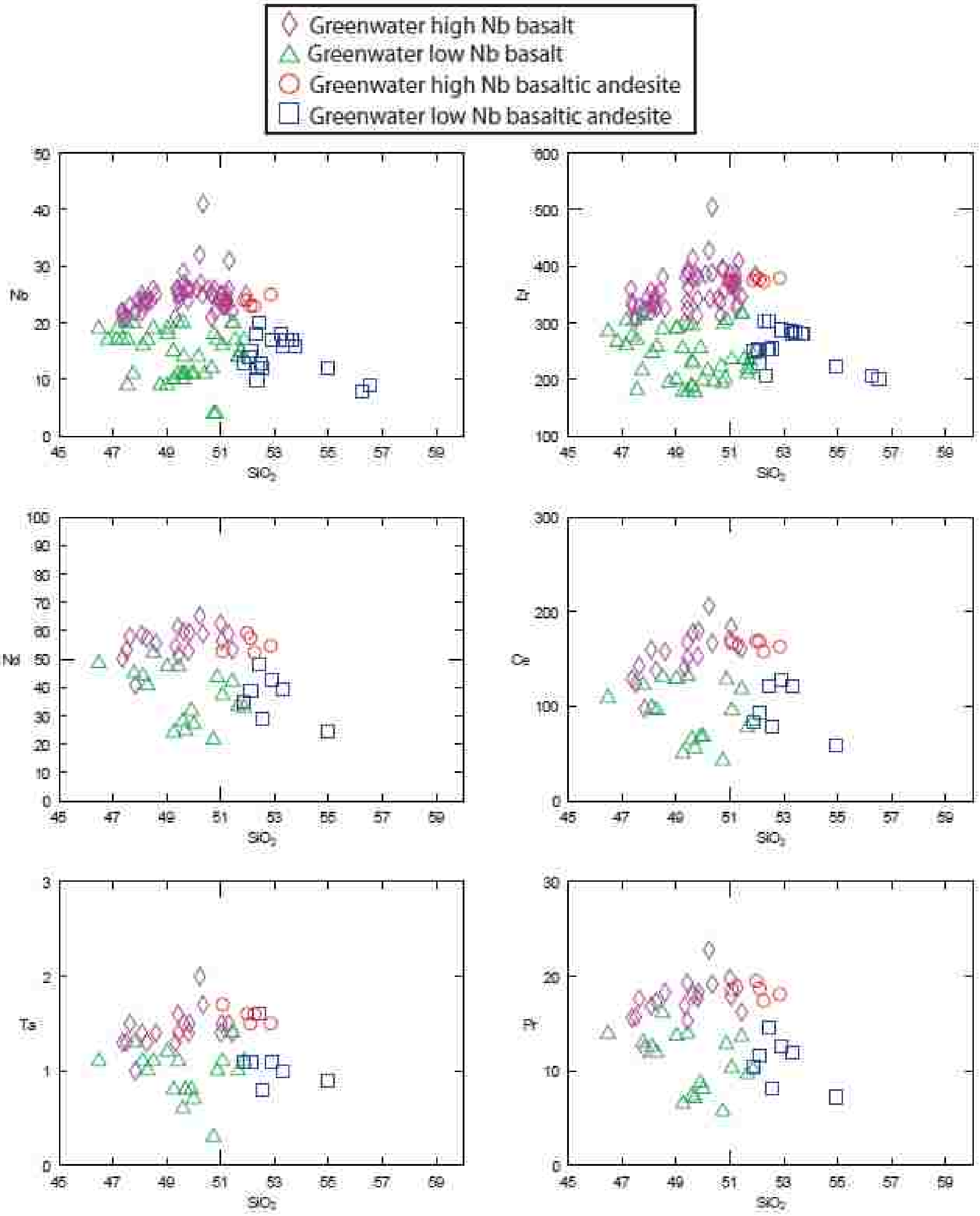

Figure 32: Trace/rare earth element vs. SiO_2 plots showing grouping of high and low Nb. Error bars are smaller than symbol size.

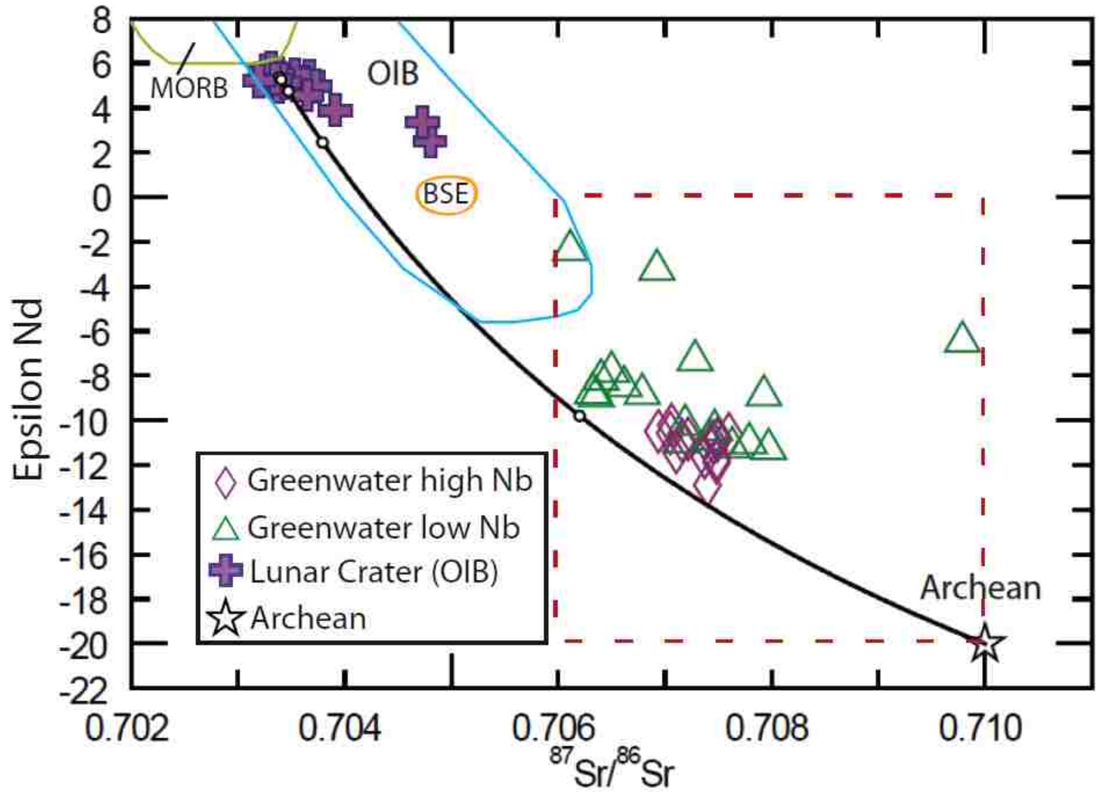

Figure 33: Archean and Lunar Crater mixing trend. Open circles on mixing line represent 5% of Archean end member. Greenwater samples require mixing 20% of the Archean end member with the OIB end member. Boundaries of OIB (blue), MORB (green), and bulk silicate earth (orange) fields indicated by colored lines. Dashed red box indicates boundary for Figures 22, 29, and 45. Error bars are smaller than symbol size.

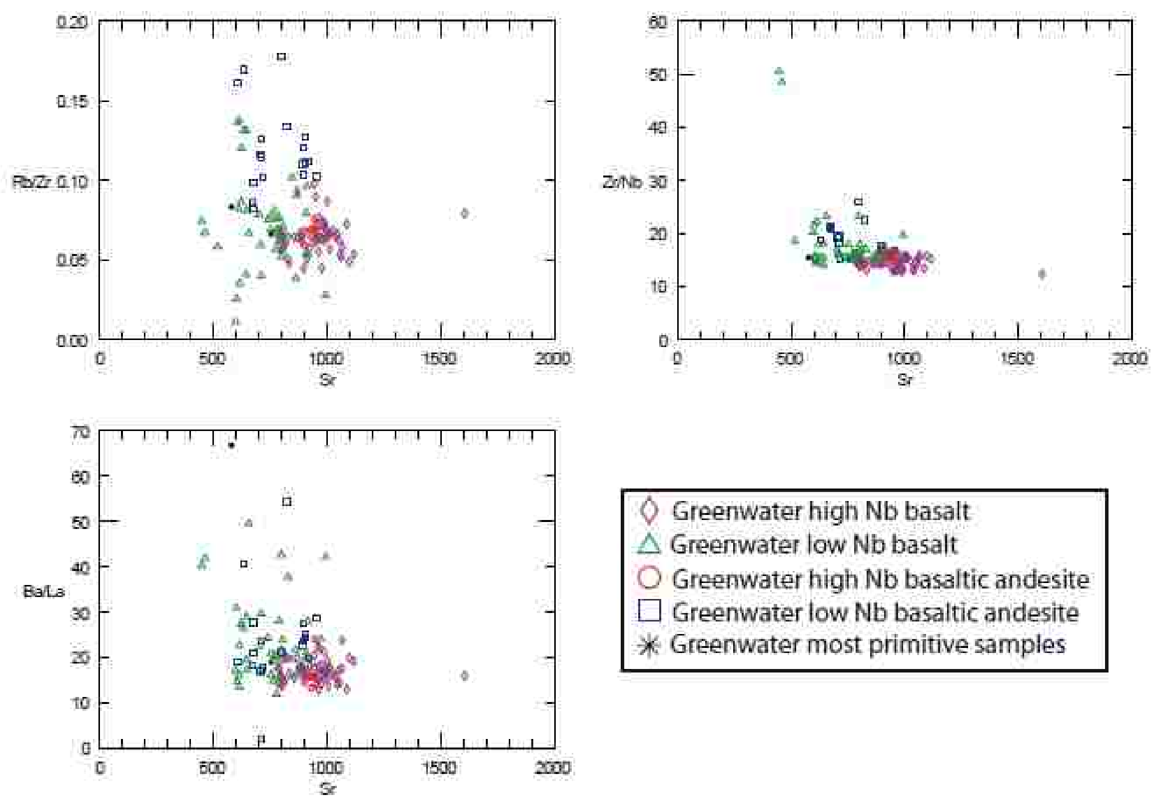

Figure 34: A) Rb/Zr vs. Sr, B) Zr/Nb vs. Sr, C) Ba/La vs. Sr. Note that the most primitive samples plot in the middle of each grouping.

CHAPTER 6

MELTING MECHANISM

If we accept the preferred model of melting of old slab components, then the next step is to propose a melting mechanism.

Edge-Driven Convection

The edge-driven convection model for asthenospheric upwelling was first proposed by King and Anderson (1998) and King and Ritsema (2000) and assumes a cratonic keel between the craton and the accretionary margin of North America and hotter areas of the asthenosphere that travel under the North American Plate. The North American plate moves northwest over alternating low and high zones of shear velocity interpreted to correlate with hot and cold areas respectively of eastward flowing mantle under the Basin and Range. Mantle flow direction is measured using seismic anisotropy of olivine crystals (Conrad et al., 2007). As the low Vs asthenosphere reaches the lithospheric keel it rises, but does not have a matching downward flow as the space necessary for this upwelling is created by the extension of the lithosphere and addition of mafic components to the lithosphere and crust above the zone of upwelling. Low Vs regions interspersed with high Vs regions result in episodic patterns of volcanism with each peak of volcanism followed by a period of quiescence (Smith et al., 2008). A ~250 km thick keel in the eastern Basin and Range is imaged by S waves and the associated asthenospheric upwellings present as low velocity zones that extend from the base of the lithosphere to a depth of approximately 300 km (Van Der Lee and Nolet, 1997). Upwelling can also be seen as a semicircular anisotropic flow feature surrounding a null region in the Great Basin (Savage and Sheehan, 2000). Both types of imaging detect upwelling under the Death Valley region as well as throughout the Basin and Range (Dueker et al., 2001) (fig. 35).

Edge-driven convection does not apply to the Death Valley area as it requires a keel that, though present to the east, is not necessarily close enough to explain volcanism in the Death Valley region. This model also requires that low Vs asthenosphere moves at a sufficient rate to produce the observed volcanism at the observed times. Actual mantle flow and circulation does not cause low Vs areas to move at a high enough velocity to explain the timing of volcanism (see details below). A revised form of the edge driven convection model was developed by Conrad (Personal Communication) that accounts for the problems mentioned above. The revised model suggests that the asthenosphere has a velocity of 0 cm/yr at the base of the lithosphere and 5 cm/yr east at a depth of 200 km (Silver & Holt 2002, Conrad et al., 2007). This velocity gradient would cause low Vs regions to shear over time changing their location and geometry. This situation results in a single anomaly traveling with the plate but shearing progressively downward. In this scenario, magmatic pulses are not related to different Vs regions but to the small-scale velocity structure of a single anomaly. Different small-scale structures within the larger anomaly would explain episodic volcanism.

Further analysis of the mantle under the Greenwater-Crater Flat region provides information on the geometry of low Vs regions and how they may be related to the observed volcanism. EarthScope's seismic array has provided seismic velocity data for the area under the Greenwater and Crater Flat fields. Seismic S-wave velocity profiles constrained by ambient noise and earthquake tomography of the mantle (Yang et al.,

2008) show low velocity pockets, which may correspond to higher temperatures and/or higher water contents. The profile at 36.25 degrees latitude from -122 to -110 degrees longitude (Fig 23) (Yang, personal communication 2009) covers the Greenwater-Crater Flat region, with Greenwater Range at 36.25 degrees latitude and -116.6 degrees longitude and Crater Flat at 36.45 degrees latitude and -116.5 degrees longitude. The profile shows a low velocity anomaly at the location and depths of melting of the Greenwater and Crater Flat volcanic fields (Fig. 23) (Yang et al., 2008; Yang, personal communication 2009).

In order to gain a better understanding of the relation of volcanism to the low velocity anomaly, it is necessary to reverse the mantle flow to the time of volcanism to observe the position of the anomaly at the time of melting. A simple representation of this can be accomplished by applying a reverse horizontal shear to the mantle profile, where the velocity is 0 cm/yr at the base of the lithosphere and 5 cm/yr at depth (Silver & Holt 2002, Conrad et al., 2007). The resultant positions of the melting columns for the Greenwater and Crater Flat volcanic fields (Fig. 36) show that, though the anomaly has moved, the movement is small enough that the anomaly is still under the volcanic fields. This suggests that a single low velocity anomaly is responsible for most, if not all, of the volcanism in the Greenwater Range.

In summary, the correspondence of a low velocity anomaly with the calculated depth of melting suggests that low velocity zones, which may either be hotter or have higher water contents, are clearly areas near or at the solidus.

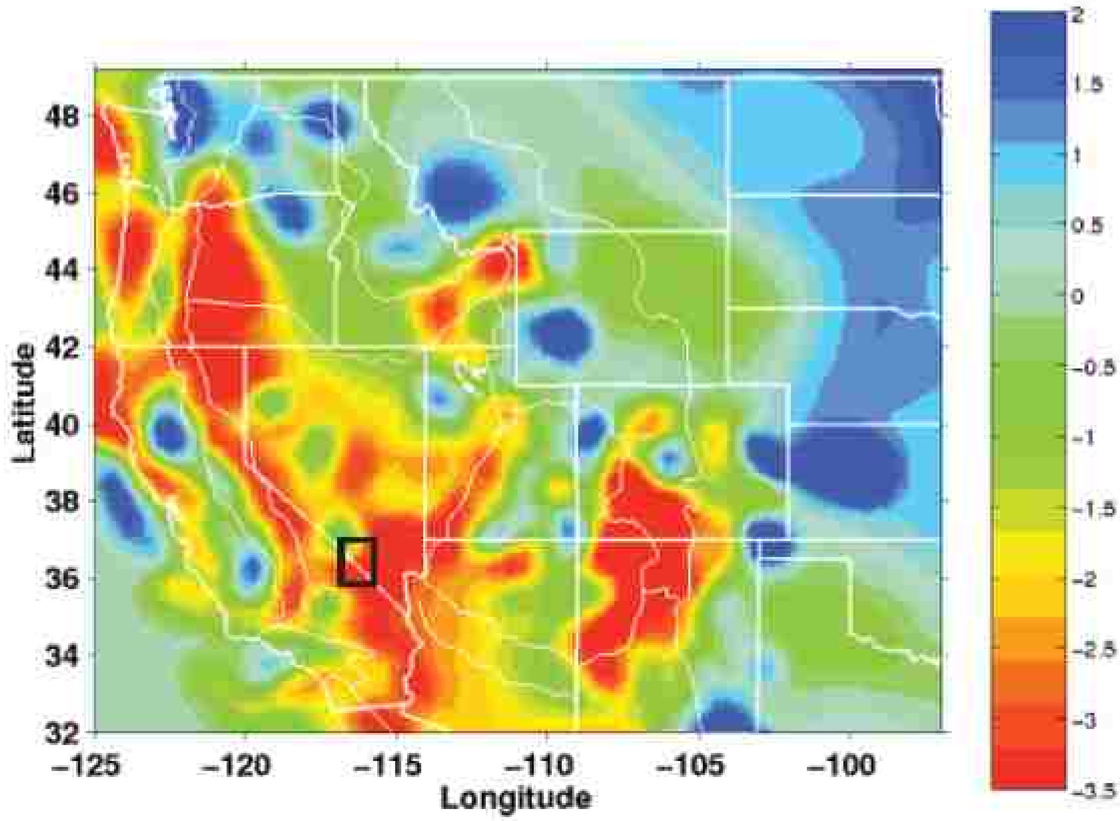

Figure 35: Compressional-wave velocity structure at 100 km depth. High velocities (blue shading) reflect colder, stable roots, and low velocities (yellow and red shading) on western side of image reflect the generally thin lithosphere and warm asthenosphere. Black box denotes Greenwater Range-Crater Flat region (after Dueker et al., 2001).

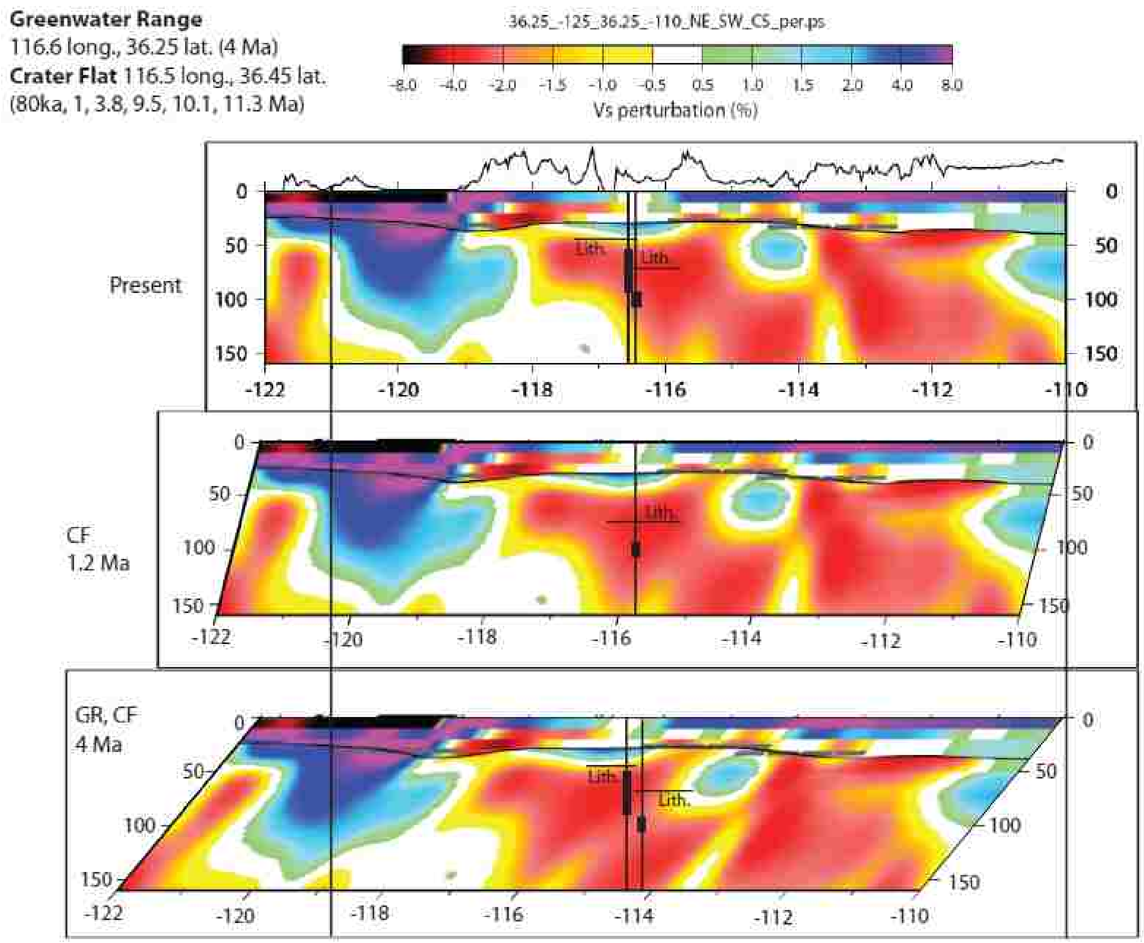

Figure 36: 36.25 N latitude mantle profile (Yang, personal communication) for Death Valley Crater Flat area for present and sheared back to 1.2 and 4 Ma. Vertical black lines represent longitudinal locations of the volcanic fields (-116.6° Greenwater Range and -116.5° Crater Flat), black rectan1gles represent melting columns (54.34 – 89.64 km Greenwater Range and 93.75 - 105 km Crater Flat), and horizontal black lines represent the approximate base of the lithosphere (47.5 km Greenwater Range and 70 km Crater Flat).

CHAPTER 7

COMPARISON BETWEEN GREENWATER AND CRATER FLAT VOLCANIC FIELDS

Volcanic hazard assessment calculations include the number of volcanic centers and the area of volcanism. If the Greenwater Range is added to the hazard assessment for the proposed high-level nuclear waste repository at Yucca Mountain, Nevada, this would increase both the number of centers and the area, and could increase the risk of disruption of the proposed repository at Yucca Mountain by several orders of magnitude (Wang et al., 2002; Smith et al., 2002; Smith and Keenan, 2005). The addition of the Greenwater Range to the hazard assessment requires a petrogenetic link between the Greenwater and Crater Flat volcanic fields. Such a link can be established by comparing isotopic, major and trace element chemistry, and depth of melting to determine if the source, melting mechanism, and magma evolution are the same.

Crater Flat basalts (Bradshaw and Smith, 1994) are classified by LeBas et al. (1986) as mainly trachybasalts with a few plotting in the basalt field (Fig. 37). These trachybasalts/basalts are potassic alkaline in nature (Fig. 38 and 39). As can be seen from the classification diagrams, Crater Flat rocks overlap in composition with the Greenwater Range basalts.

Crater Flat basalts range from 48.63 – 50.33 wt. % SiO_2 and in Mg# from 47 – 49.3 (Fig. 40). These values fall in the middle of the range of high Nb Greenwater Range basalt (Fig. 40). Major element trends of Crater Flat basalt using SiO_2 as an index of magma evolution (Harker diagrams) are similar to and fall in the middle of the range of Greenwater Range basalts (Fig. 41). Crater Flat values tend to group with Greenwater

Range high Nb samples but are slightly above this group in Al_2O_3 and below in FeO (Fig. 41). The major exception to this observation is that Crater Flat basalt corresponds to the low TiO_2 part of the low Nb group (Fig. 41).

Crater Flat basalts have the same OIB signature as the Greenwater Range with slightly higher values in general. They exhibit the same deviations from OIB, with the exception of a higher Nd, a lack of a distinct higher Pb anomaly, and a clear negative Ti anomaly that is much smaller in Greenwater Range samples (Fig. 42a). Chondritic normalized values give a clearer view of the slightly higher light REE contents and high Greenwater Range values for heavy REEs (Fig. 42b). Crater Flat Nb/La ratios (0.2 - 0.3) overlap the lower end of the Greenwater Range and fall in the lithospheric influence range (Fig. 43).

The observed grouping of high and low Nb samples in Greenwater Range basalt extends to Crater Flat in that Crater Flat samples fall in or above the high Nb group (Fig. 44). This is also seen in the slightly higher overall trace element signature for Crater Flat seen on the spider diagrams (Fig. 44) and the grouping of Crater Flat samples with the high Nb group on major element Harker diagrams (Fig. 41) as discussed above.

Isotopically, Crater Flat basalts are similar to Greenwater Range basalts. Epsilon Nd (-8.62 to -9.81) and $^{87}Sr/^{86}Sr$ (0.70691 to 0.70704) are within the range of Greenwater Range basalts, but with less variation (Fig. 45). $^{206}Pb/^{204}Pb$ (18.446 to 18.565) and $^{207}Pb/^{204}Pb$ (15.575 to 15.624) values are too tightly grouped to observe a trend but extend the Greenwater Range trend to slightly higher ratios (Fig. 46). All samples plot above the Northern Hemisphere Reference Line, indicating a lithospheric component.

Both Crater Flat and the Greenwater Range have melting depths that lie in the asthenosphere just below the base of the lithosphere. Melting depths at Crater Flat are 93.75 – 105 km and occur 24-35 km below a 70 km thick lithosphere and Greenwater basalt was generated at a depth of 54.3 – 89.6 km, 4-40 km below a 45-50 km thick lithosphere (Fig. 23). They also plot near each other in a low velocity anomaly (Fig. 23).

Summary

Crater Flat basalts have major, trace, and isotopic chemistry that is similar to those of the Greenwater Range. Both sets of basalt have similar major and trace element chemistry, similar isotopic ratios, and melting columns in the asthenosphere just below the base of the lithosphere. The similar chemistry and the close spatial relationship (~35 km separation) of the fields result in melting columns that plot in the same low velocity anomaly. These similarities suggest that the same reasoning that makes the slab component model the preferred model for the Greenwater Range (chapter 5) makes it preferred viable model for Crater Flat as well.

Given their spatial relationship, it is also possible that the Greenwater and Crater Flat basalts were produced by the same mechanism. This similarity between the Greenwater and Crater Flat fields indicates a relationship between the two and the need to add the Greenwater Range to the Crater Flat field for the calculation of the volcanic hazard about Yucca Mountain. Based on the probability equation, this would add area as well as volcanic centers to the calculation of the hazard assessment and may increase it by several orders of magnitude.

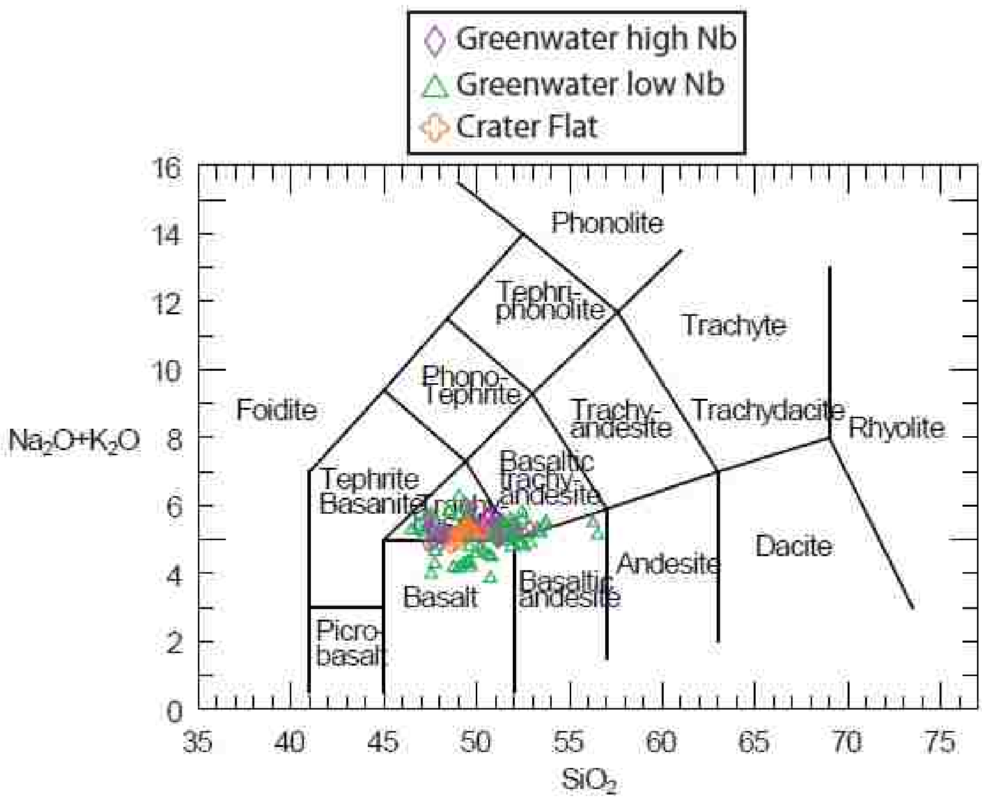

Figure 37: LeBas et al. (1986) rock classification diagram of Greenwater Range and Crater Flat basalts.

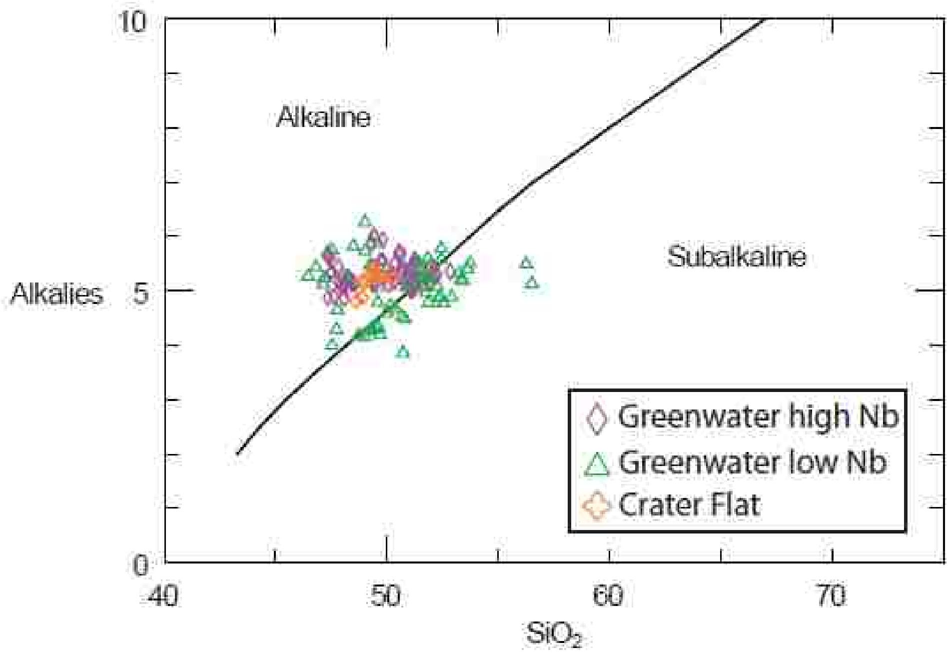

Figure 38: Alkaline vs. Subalkaline discrimination diagram for Greenwater Range and Crater Flat basalts.

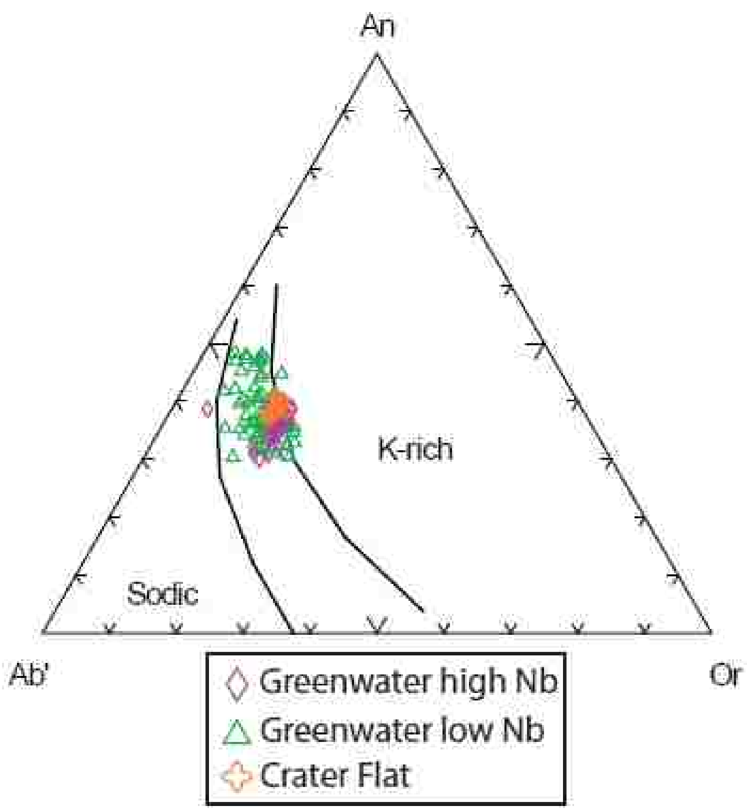

Figure 39: Potassic vs. sodic classification diagram for alkaline Greenwater Range and Crater Flat basalts.

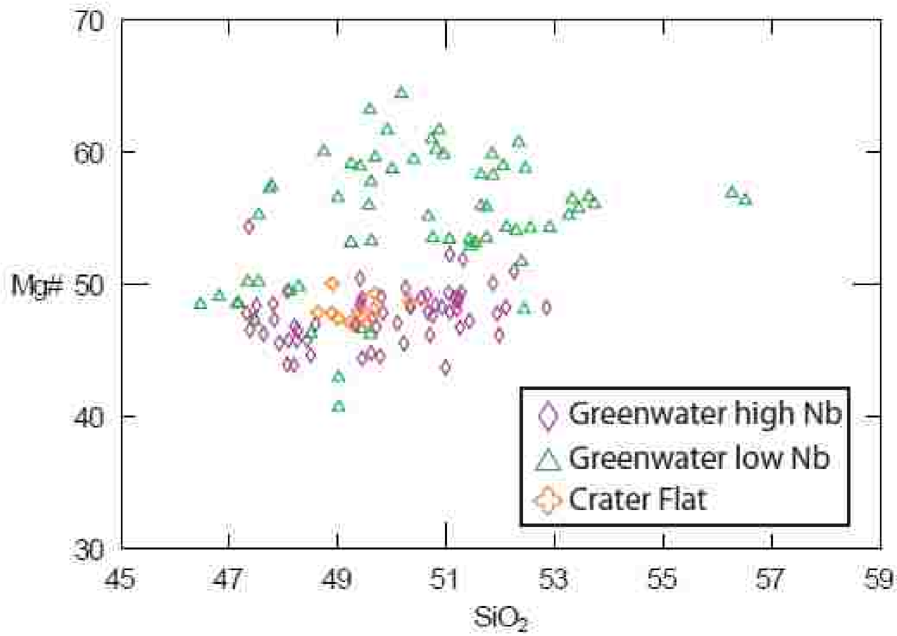

Figure 40: Mg# vs. SiO_2 plot for Greenwater Range and Crater Flat basalts. Error bars are smaller than symbol size.

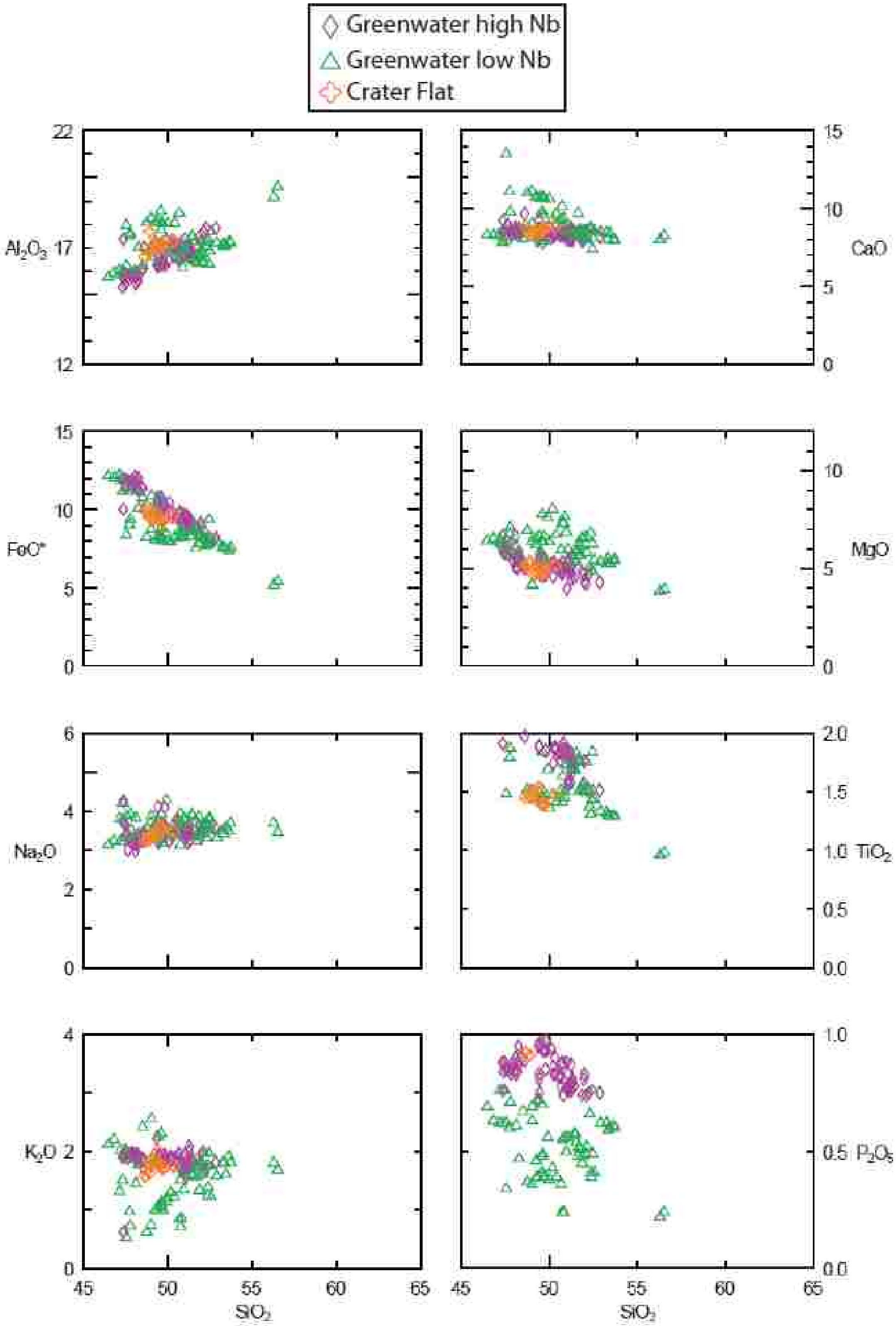

Figure 41: Harker variation diagrams for Greenwater Range and Crater Flat basalts. Error bars are smaller than symbol size.

A)

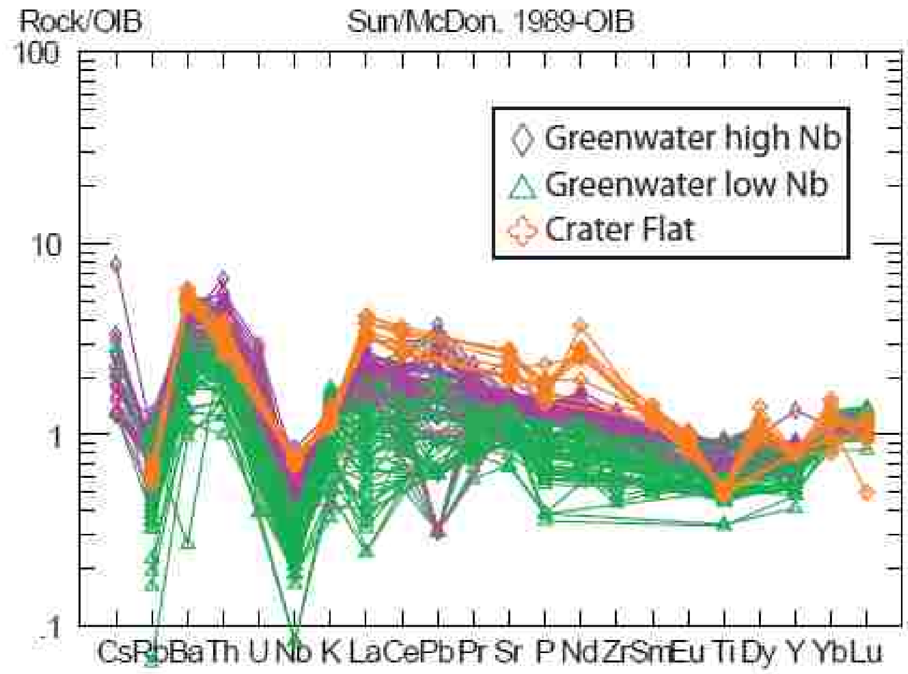

B)

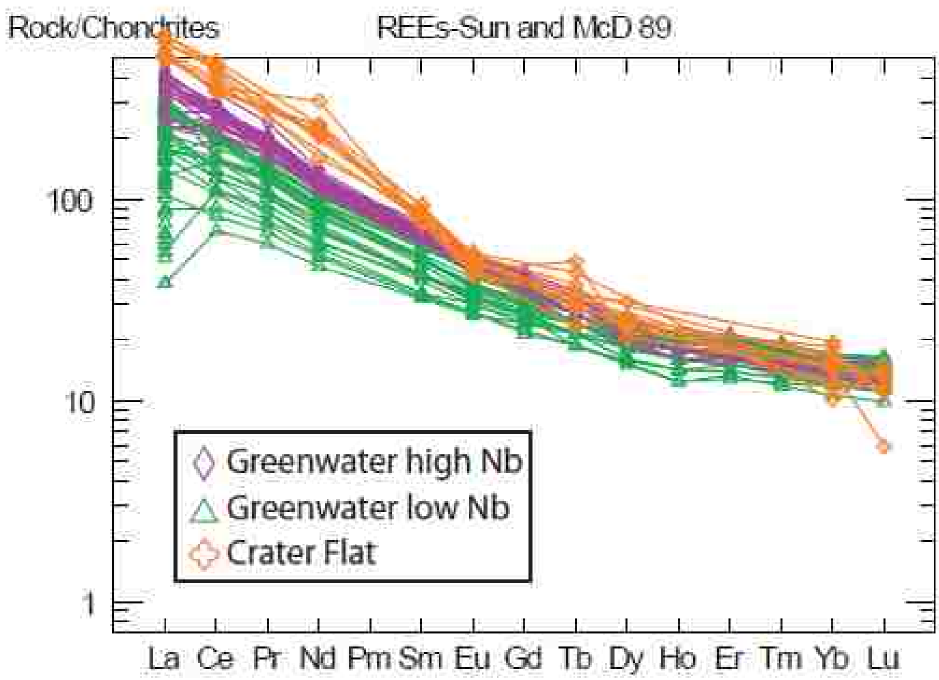

Figure 42: A) OIB normalized spider diagram, B) Chondrite normalized spider diagram.

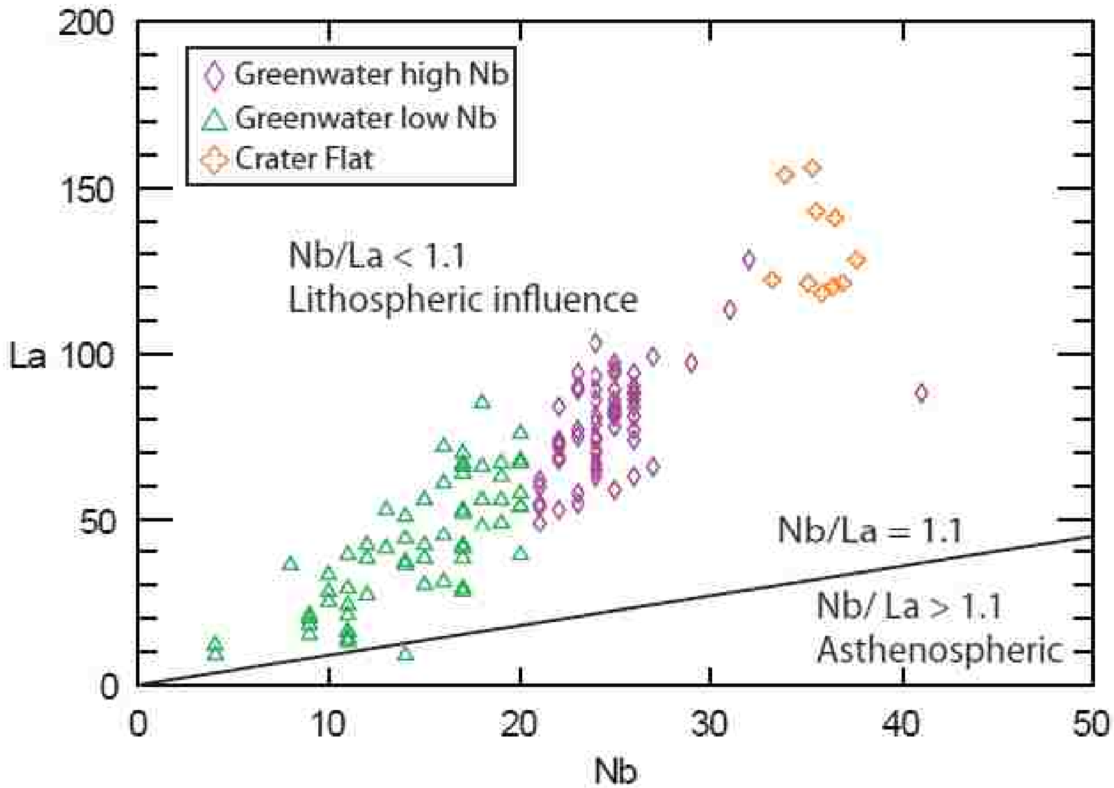

Figure 43: La vs. Nb plot showing the Nb/La =1.1 line, where Nb/La < 1.1 indicates lithospheric influence. Error bars are smaller than symbol size.

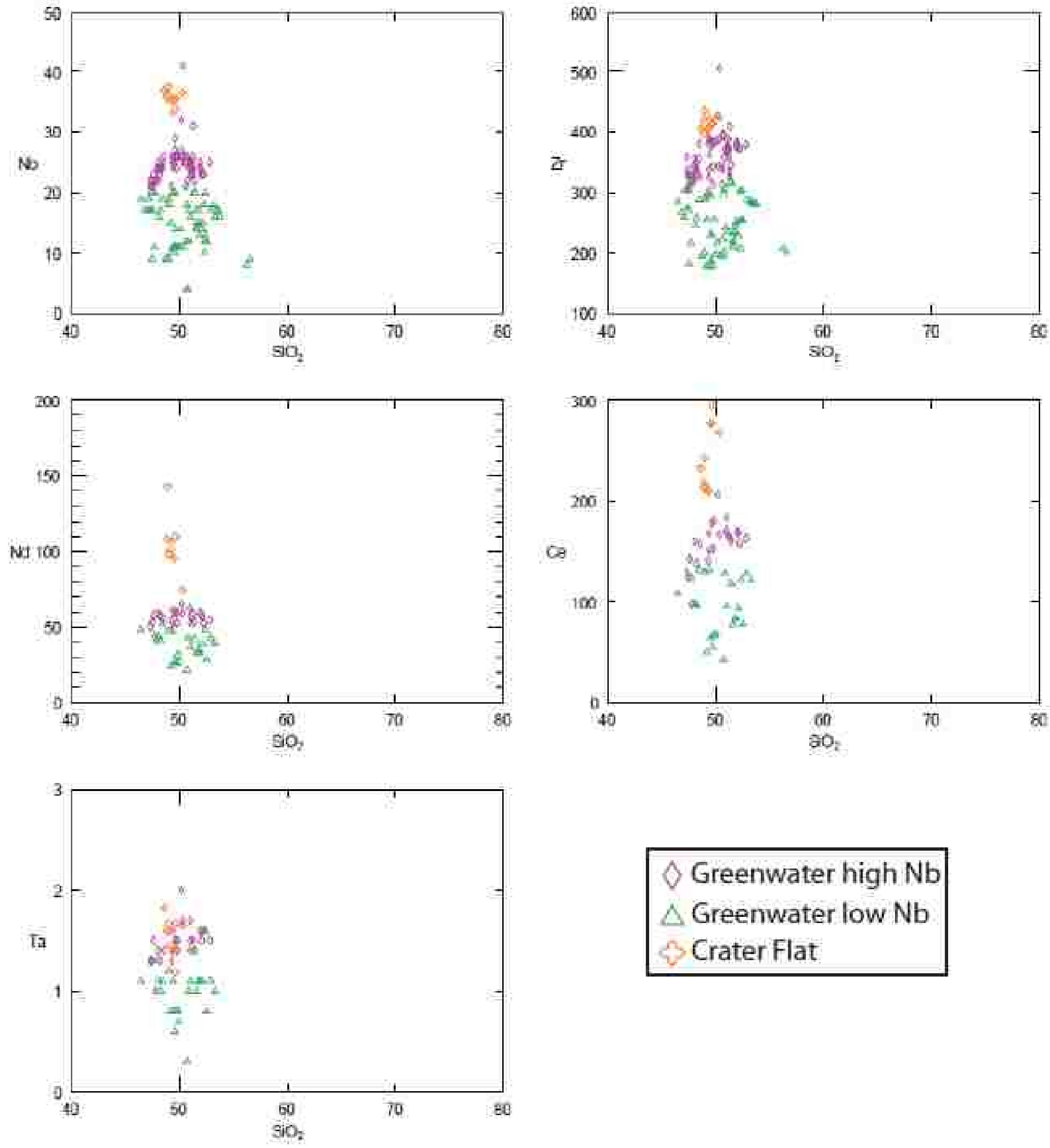

Figure 44: Trace/rare earth element vs. SiO_2 plots showing grouping of high and low Nb samples. Error bars are smaller than symbol size.

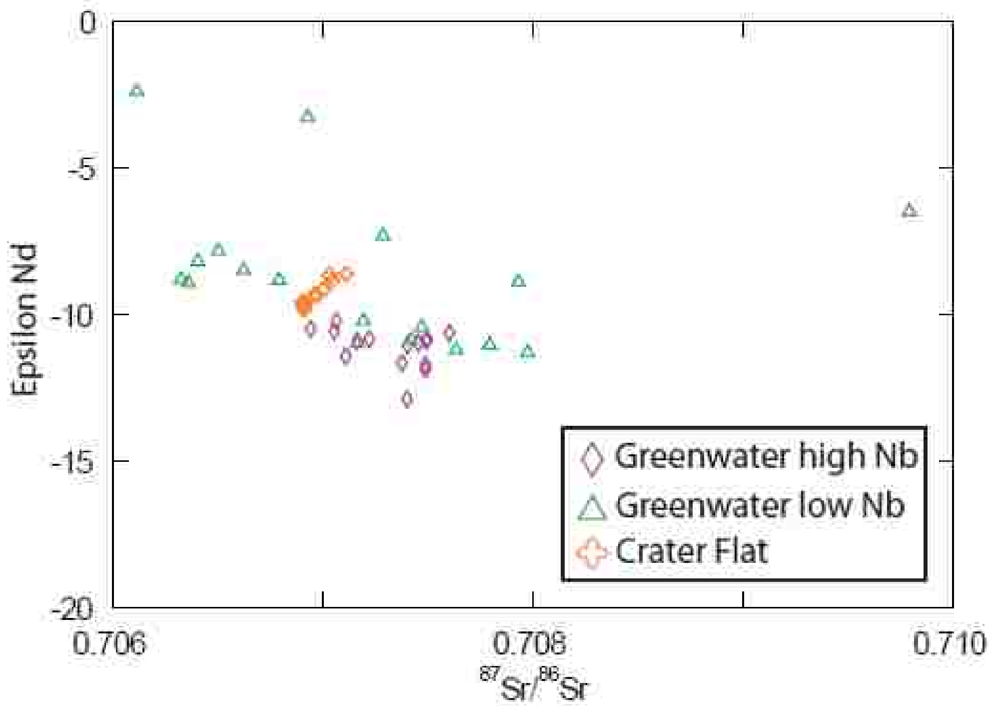

Figure 45: Epsilon Nd vs. $^{87}Sr/^{86}Sr$ plot for Greenwater and Crater Flat basalts. Compositional fields can be seen in figure 33. Error bars are smaller than symbol size.

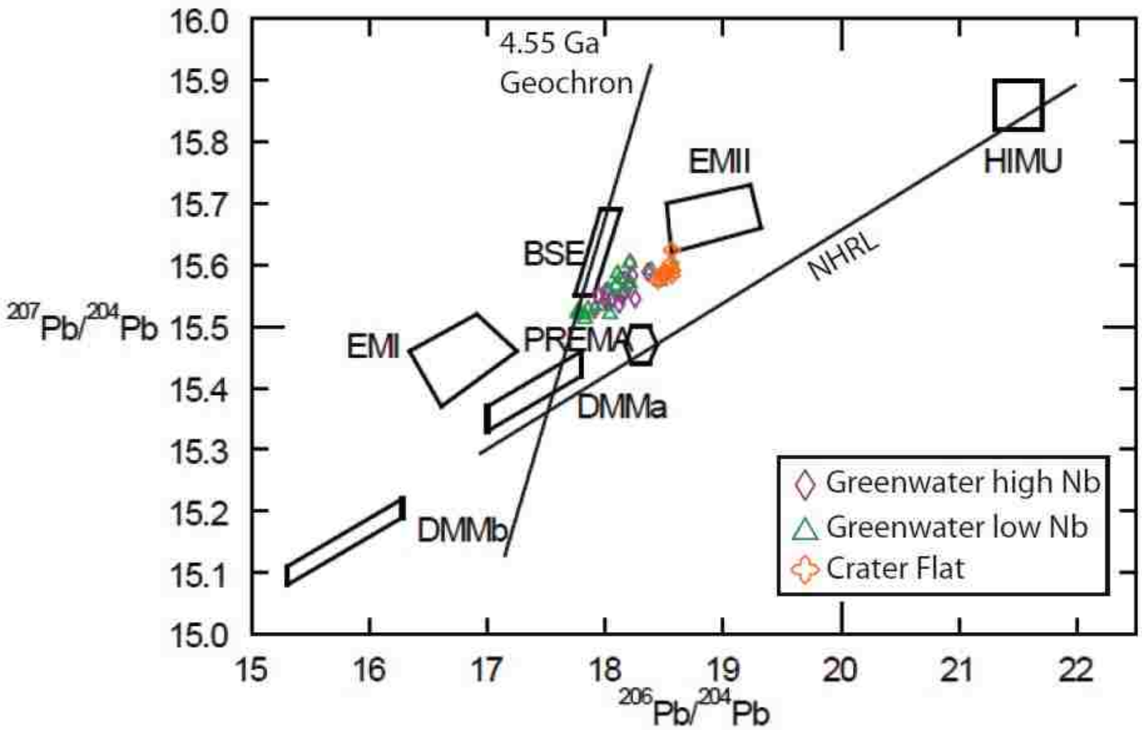

Figure 46: $^{207}Pb/^{204}Pb$ vs. $^{206}Pb/^{204}Pb$ plot Greenwater and Crater Flat basalts. NHRL and Geochron from Wilson (2001). Error bars are smaller than symbol size.

CHAPTER 8

SUMMARY AND CONCLUSIONS

The Greenwater Range volcanic field is mainly basalt/trachybasalt with some areas of basaltic andesite/basaltic trachyandesite. Twenty-four volcanic centers are cinder cones in various stages of erosion from cones to plugs to highly degraded craters. Most centers are associated with lava flows that overlie sedimentary units and the rhyolite of the Funeral Formation. Greenwater basalt contains olivine with rare plagioclase and oxides. Matrix is mainly plagioclase with varying amounts of olivine, glass, and oxides. Partially resorbed quartz and plagioclase xenocrysts were found in several samples.

The chemical signature is OIB with slight variations indicative of slab and oceanic sediment in the source. Epsilon Nd and $^{87}Sr/^{86}Sr$ indicate an ancient lithospheric influence as does $^{206}Pb/^{204}Pb$ and $^{207}Pb/^{204}Pb$ that fall above the northern hemisphere reference line and Nb/La <1.1. Trace and isotopic data distribution indicate evolution without significant FC or AFC.

Temperatures, pressures, and depths, of melting are 1367 - 1435^{o}C, 1.45 - 2.39 GPa, and 54.3 – 89.6 km for the Greenwater Range and 1388-1415^{o}C, 2.5-2.8 GPa (Plank, personal communication 2008), and 93.75-105 km for Crater Flat. The base of the lithosphere is 45-50 km below the Greenwater Range and 70 km below Crater Flat, placing the melting columns entirely in the asthenosphere and temperatures too high to be in the lithosphere.

The results of this study indicate that the best source and evolution model for the Greenwater Range and Crater Flat is melting of old ($\geq$ 1 billion yr) slab components from related to Proterozoic subduction. These slab components, along with lithospheric mantle, were converted to asthenosphere thermally and mechanically as the geotherm rose and caused the lithosphere-asthenosphere boundary to rise. This, combined with smaller degrees of partial melting to produce the basaltic andesites, explains the observed major, trace and isotopic chemistry of the Greenwater Range volcanic section. The chemical similarities and spatial relationships of the Crater Flat and Greenwater Range fields indicate that this may also be the source of the Crater Flat basalts.

The best melting mechanism for these basalts involves melting in low Vs pockets in the asthenosphere that move with the lithosphere but undergo downward shear. The chemical similarity of the Crater Flat basalts and their spatial proximity indicate this mechanism may be valid for both fields.

Future work to better understand these fields and their relationship to each other might include better imaging of the low velocity mantle anomaly under the Greenwater and Crater Flat fields to determine the nature of the small scale structure and its precise relationship to the melting. Water content of melt inclusions of this and other anomalies should be analyzed to determine whether the low velocity zones reflect high water contents or high temperatures. Melting columns for other basalt fields in the western United States should be compared to seismic tomographic profiles to see if calculated melting depths correspond to low velocity anomalies. This is an important step in determining whether mechanisms proposed for the Greenwater Range are generally applicable to other volcanic fields.

REFERENCES

Asmerom, Y., Jacobsen, S.B., Wernicke, B.P., 1994, Variations in magma source regions during large-scale continental extension, Death Valley region, western United States: Earth and Planetary Science Letters, v. 125, p. 235-25.

Atwater, T., 1970, Implications of plate tectonics for the Cenozoic tectonic evolution of western North America: Geological Society of America Bulletin, v. 81, p. 3515-3536.

Bradshaw, T.K., and Smith, E.I., 1994, Polygenetic Quaternary volcanism at Crater Flat, Nevada: Journal of Volcanology and Geothermal Research, v. 63, p. 165-182.

Bunge, H-P., Grand, S. P., 2000, Mesozoic plate-motion history below the northeast Pacific Ocean from seismic images of the subducted Farallon slab: Nature, v. 405, p. 337-340.

Conrad, C.P., Behn, M.D., Silver, P.G., 2007, Global mantle flow and the development of seismic anisotropy: Differences between ocean and continental upper mantle: Journal of Geophysical Research, v. 112, B07317, doi:10.1029/2006JB004608.

Conrad, C.P., Wu, B., Smith, E.I., Bianco, T.A., Tibbetts, A., 2009, Shear-Driven Upwelling Induced by Lateral Viscosity Variations and Asthenospheric Shear: A Mechanism for Intraplate Volcanism: Physics of the Earth and Planetary Interiors, doi:10.1016/j.pepi.2009.10.001.

Daley, E.E., and DePaolo, D.J., 1992, Isotopic evidence for lithospheric thinning during extension: Southeastern Great Basin: Geology v. 20, p. 104-108.

DePaolo, D. J., and E. E. Daley, 2000, Neodymium isotopes in basalts of the southwest basin and range and lithospheric thinning during continental extension: Chemical Geology, v. 169, p. 157-185.

Dickson, L.D., 1995, Volcanology and geochemistry of Pliocene and Quaternary basalts on Citadel Mountain, Lunar Crater volcanic field, Pancake Range, Nevada: Thesis, p. 146

Dueker, K., Yuan, H., and Zurek, B., 2001, Thick-structured Proterozoic Lithosphere of the Rocky Mountain Region: GSA Today, v. 11, no. 12, p. 4-9.

Eaton, G.P., 1982, The Basin and Range province: Origin and tectonic significance: Annual Reviews Earth and Planetary Science, v. 10, p. 409-440.

Farmer, G.L., Perry, F.V., Semken, S., Crowe, B., Curtis, D., and DePaolo, D.J., 1989, Isotopic evidence on the structure and origin of subcontinental lithospheric mantle in southern Nevada: Journal of Geophysical Research, v. 94, p. 7885-7898.

Feuerbach, D.L., Smith, E.I., Walker, J.D., and Tangeman, J.A., 1993, The role of the mantle during crustal extension: Constraints from geochemistry of volcanic rocks in the Lake Mead area, Nevada and Arizona: Geological Society of America Bulletin, v. 105, p. 1561-1575.

Fitton, J.G., James, D., and Leeman, W.P., 1991, Basic magmatism associate with late-Cenozoic extension in the western United States: Compositional variations in space and time: Journal of Geophysical Research, v. 96, p. 13693-13711.

Fleck, R.J., 1970, Age and tectonic significance of volcanic rocks, Death Valley area, California: Geological Society of America Bulletin, v. 81, p. 2807-2816.

Gallagher, K., Hawkesworth, C., 1992, Dehydration melting and he generation of continental flood basalts: Nature, v. 358, p. 57-59.

Harry, D.L., and Leeman, W.P., 1995, Partial melting of melt metasomatized subcontinental mantle and the magma source potential of the lower lithosphere: Journal of Geophysical Research, v. 100, p. 10255-10269.

Harry, D.L., Sawyer, D.S., and Leeman, W.P., 1993, The mechanics of continental extension in western North America: Implications for the magmatic and structural evolution of the Great Basin: Earth and Planetary Science Letters, v. 117, p. 59-71.

Jones, C.H., 1987, Is extension in Death Valley accommodated by thinning of the mantle lithosphere beneath the Sierra Nevada, California?: Tectonics, v. 6, p. 449-473.

Jones, C. H., B. P. Wernicke, G. L. Farmer, J. D. Walker, D S. Coleman, L. W. McKenna, and F. V. Perry, 1992, Variations across and along a major continental rift: An interdisciplinary study of the basin and range province, Western, USA: Tectonophysics, v. 213, p. 57-96.

Jones, J.V. III, Connelly, J.N., Karlstrom, K.E., Williams, M.L., and Doe, M.F., 2009, Age, provenance, and tectonic setting of Paleoproterozoic quartzite successions in the southwestern United States: Geological Society of America Bulletin, v. 121, p. 247-264.

King, S.D., and Anderson, D.L., 1998, Edge-driven convection: Earth Planetary Science Letters, v. 160, p. 289-296.

King, S.D., and Ritsema, J., 2000, African hot spot volcanism: Small-scale convection in the upper mantle beneath cratons, Science, v. 290, p. 1137-1140.

LeBas, M.J., LeMaitre, R.W., Streckeisen, A., and Zanettin, B., 1986. A chemical classification of volcanic rocks based on the total alkali silica diagram. J. Pet. 27:745-750.

Lee, C.-T. A., Luffi, P., Plank, T., Dalton, H., Leeman, W. P., 2009, Constraints on the depths and temperatures of basaltic magma generation on Earth and other terrestrial planets using new thermobarometers for mafic magmas: Earth and Planetary Science Letters, v. 279, p. 20-33.

Lee, C-T. A., Yin, Q., Rudnick, R.L., Chesley, J.T., Jacobsen, S.B., 2000, Osmium isotopic evidence for Mesozoic removal of lithospheric mantle beneath the Sierra Nevada, California: Science, v. 289, p. 1912-1916.

Luffi, P., Saleeby, J.B., Lee, C-T.A., and Ducea, M.N., 2009, Lithospheric mantle duplex beneath the central Mojave Desert revealed by xenoliths from Dish Hill, California: Journal of Geophysical Research, v. 114, B03202, doi:10.1029/2008JB005906.

Lum, C. L., Leeman, W.P., Foland, K.A., Kargel, J.A., Fitton, J.G., 1989, Isotopic variation in continental basalt lavas as indicators of mantle heterogeneity: Examples from the western U.S. Cordillera: Journal of Geophysical Research, v. 94, p. 7871-7884.

McAllister, J.F., 1970, Geologic Map and Sections of the Amargosa Valley Borate-Area Southeast Continuation of the Furnace Creek Area – Inyo County, California: U.S. Geological Survey Miscellaneous Investigations Map I-782, scale 1:24,000.

McAllister, J.F., 1973, Geology of the Furnace Creek Borate Area, Death Valley, Inyo County, California: California Div. Mines and Geology Map Sheet 14, with text, 9p.

McKenzie, D., and Bickle, M.J., 1988, The volume and composition of melt generated by extension of lithosphere: Journal of Petrology, v. 29, p. 625-679.

Ormerod, D.S., Hawkesworth, C.J., Rogers, N.W., Leeman, W.P., and Menzies, M., 1988, Tectonic and magmatic transitions in the western Great Basin, USA: Nature, v. 333, p. 349-353.

Ormerod, D. S., N. W. Rogers, and C. J. Hawkesworth, 1991, Melting in the lithospheric mantle: Inverse modeling of alkaline-olivine basalts from the big pine volcanic field, California: Contributions to Mineralogy and Petrology, v. 108, p. 305-317.

Perry, F.V., Baldridge, W.S., and DePaolo, D.J., 1988, Chemical and isotopic evidence of lithospheric thinning beneath the Rio Grande rift: Nature, v. 332, p. 432-434.

Rogers, N. W., C. J. Hawkesworth, and D. S. Ormerod, 1995, Late Cenozoic basaltic magmatism in the Western Great Basin: Journal of Geophysical Research, v. 100, p. 10,287-10,301.

Savage, M. K., and Sheehan, A. F., 2000, Seismic anisotropy and mantle flow from the Great Basin to the Great Plains, western United States: Journal of Geophysical Research, v. 105, p. 13725-13734.

Serpa, L., and Pavlis, T.L., 1996, Three-dimensional model of the late Cenozoic history of the Death Valley region, southeastern California: Tectonics, v. 15, p. 1113-1128.

Silver, P.G., Holt, W.E., 2002, The mantle flow field beneath western North America: Science, v. 295, p. 1054-1057.

Smith, E., Conrad, C.P., Plank, T., Tibbetts, A., Keenan, D., 2008, Testing Models for Basaltic Volcanism: Implications for Yucca Mountain, Nevada: International High-Level Radioactive Waste Management, p. 156-164.

Smith, E. I., Keenan, D. L., Plank, T., 2002, Episodic Volcanism and Hot Mantle: Implications for Volcanic Hazard Studies at the Proposed Nuclear Waste Repository at Yucca Mountain, Nevada: GSA Today, v. 12, p. 4-10.

Smith, E.I., and Keenan, D.L., 2005, Yucca Mountain could face greater volcanic threat: EOS, Transactions of the American Geophysical Union, v. 86, p. 317-321.

Streitz, R., Stinson, M.C., 1977, Geologic Map of California Death Valley Sheet: California Div. Mines and Geology, scale 1:250,000.

Terra Softa Inc., Igpet for Windows: 155 Emerson Rd. Somerset, NJ 08873 Copyright January 9, 2000

Van Der Lee, S., and Nolet, G., 1997, Upper mantle S velocity structure of North America: Journal Geophysical Research: v. 102, p. 22815-22838.

Vaniman, D. T. and Crowe, B. M., and Gladney, E. S., 1982, Petrology and geochemistry of Hawaiite lavas from crater flat, Nevada: Contributions to Mineralogy and Petrology, v. 80 p. 341-357.

Walker, J.D., and Colman, D.S., 1991, Geochemical constraints on mode of extension in the Death Valley region: Geology, v. 19, p. 971-974.

Wang, K., Plank, T., Walker, J.D., and Smith, E.I., 2002, A mantle melting profile across the Basin and Range, SW USA: Journal of Geophysical Research, v. 107, p. 1-21.

Wesnousky, S.G., 2005, The San Andreas and Walker Lane fault systems, western North America: transpression, transtension, cumulative slip and the structural evolution of a major transform plate boundary: Journal of Structural Geology, v. 27, p. 1505–1512.

Wilson, M., 2001, Igneous petrogenesis: A global tectonic approach: Kluwer Academic Publishers, Boston, MA, 219 pp..

Wooden, J.L, and Miller, D.M., 1990, Chronologic and isotopic framework for early Proterozoic crustal evolution in the Mojave Desert region, SE California: Journal of Geophysical Research, v. 95, p. 20,133-20,146..

Yang, Y., M. H. Ritzwoller, F.-C. Lin, M. P. Moschetti, and Shapiro, N.M., 2008, Structure of the crust and uppermost mantle beneath the western United States revealed by ambient noise and earthquake tomography: Journal of Geophysical Research, v. 113, B12310, doi:10.1029/2008JB005833.

Yogodzinski, G.M., Naumann, T.R., Smith, E.I., and Bradshaw, T.K., 1996, Evolution of a mafic volcanic field in the central Great Basin, south central Nevada: Journal of Geophysical Research, v. 101, p. 17,425-17,445.

Zandt, G., Myers, S.C., and Wallace, T.C., 1995, Crust and mantle structure across the basin and range-Colorado plateau boundary at 37^{o}N latitude and implications for Cenozoic extensional mechanism: Journal of Geophysical Research, v. 100, p. 10,529-10,548.

APPENDIX A

THIN SECTION DESCRIPTIONS

DV-07-05
98% matrix (plag., oxides) (mildly oriented)
2% phenocrysts (50% olivine, 50% oxides)
ol.– subhedral, partially altered to iddingsite; opaque, clumped, square oxide inclusions

DV-07-06
65% glassy matrix (99% plag., 1% ol.)
35% phenocrysts (60% oxides, 25% ol., 15% plag.)
ol. phenocrysts – subhedral/anhedral , partially altered to iddingsite
plag. – zoned, albite twinning, mostly large rectangular laths,
-very little plag. and ol. intergrowth for phenocrysts

DV-07-07
Matrix (80% plag., 10% oxides, 10% ol./idd) oriented
Phenocrysts (100% ol.)
ol. – subhedral/anhedral, not to mostly altered, oxide inclusions

DV-07-09
Slightly vesicular
85% matrix (40% plag., 5% ol./iddingsite, 55% glass)
15% phenocrysts (70% ol./idd, 30% oxides)
ol. phenocrysts – subhedral/anhedral, smaller are less altered to iddingsite, minor clumping

DV-07-11
80% matrix (10% oxides, 80% plag, 10% ol./idd)
20% phenocrysts (10% plag., 90% ol.)
ol. – sub/anhedral clumps
plag. – rectangular laths, albite twinning

DV-07-12
90% matrix (80% plag., 10% oxides, 10% ol.) oriented
10% phenocrysts (100% ol.)
ol. phenocrysts – anhedral/subhedral, minor alteration to iddingsite, lots of oxides and oxide clumps 10-50% of crystal volume

DV-07-13
Vesicular
95% matrix (88% glass, 10% plag., 2% oxides) oriented
5% phenocrysts (100% ol.)
Ol. phenocrysts – sub/anhedral, minor alteration to iddingsite, some oxide inclusions ($\leq$10% of crystal volume)

DV-07-14
90% matrix (60% glass, 5% oxides, 35% plag.)
10% phenocrysts (100% oxides)
Oxides – opaque, squares and clumps

DV-07-15
(40% black, 60% red) color differentiation is more distinct to naked eye than with microscope, black possibly filled in vesicles (amygdaloidal)

- Black

-Less plag. than red portion
matrix (glassy with very small plag. laths)
phenocrysts (some small rare oxides, large ol.)
Ol. – eu/subhedral, large, slightly altered to iddingsite, ~5% crystal volume oxide inclusions

- Red

90% matrix (30% plag., 40% glass, 30% oxides)
10% phenocrysts (100% oxide)
Oxides –large, blocky or globular

DV-07-16
Vesicular
98% matrix (70% glass, 25% plag., 3% oxides, 2% ol.) oriented
2% phenocrysts (100% ol.)
Ol. – mostly euhedral/subhedral, some anhedral, oxides inclusions are 5-10% crystal volume, minor alteration to iddingsite

DV-07-17
97% matrix (68% plag., 20% glass, 10% oxides, 2% ol.) oriented
3% phenocrysts (100% ol.)
ol. – sub/anhedral, very little alteration to iddingsite, ~5-10% crystal volume is oxide inclusions

DV-07-18
Nonvesicular
98% matrix (70% plag., 20% ol., 10% oxides) oriented
2% phenocrysts (100% ol.)
ol. – subhedral, minor alteration to iddingsite, oxide inclusions, (0.5-1.5 mm) single crystals, 1.5 mm glomerocrysts

DV-07-19
Nonvesicular
98% matrix (80% plag., 20% ol.) oriented
2% phenocrysts (100% ol.)
ol. – subhedral, minor alteration to iddingsite, some oxide inclusions, 0.5-1 mm, some clumping

DV-07-20
Highly vesicular
98% matrix (70% plag., 15% ol/idd, 15% oxides)
2% phenocrysts (100% ol.)
ol. – small (≤ 0.25 mm), rare, subhedral, commonly near vesicles, some alteration to iddingsite, some completely altered

DV-08-34
Minor vesiculation
70% matrix (90% plag., 10 oxides, <<1% ol.)
30% phenocrysts (95% ol., 5% oxides)
ol. – eu/subhedral, mostly large (1-2 mm), rare small (0.75 mm), half altered to iddingsite, lots of oxide inclusions

DV-08-39
Nonvesicular
70% matrix (90% plag., 5% ol., 5% oxides)
30% phenocrysts (95% ol., 5% oxides)
ol. – euhedral to anhedral, mostly large (1mm, few 1.5 mm), rare small (0.5 mm), most almost completely altered to iddingsite, lots of oxide inclusions

DV-08-69
Minor vesiculation
88% matrix (10% ol, 10% oxides, 80% plag.)
12% phenocrysts (95% ol., 5% plag.)
- several large ol./plag. glomerocrysts (2 mm)
ol. – sub/anhedral, mostly large (1-1.5 mm), few small (0.5 mm), minor alteration to iddingsite
plag. – several large (1.5-2 mm), mostly small (<0.25 mm) rectangular laths, albite twinning

DV-08-72
Vesicular
85% matrix (20% oxides, 30% glass, 50% plag.)
15% phenocrysts (90% ol., 10% plag.)
ol. – anhedral, large (1-1.5 mm), numerous small (0.25-0.5 mm), iddingsite rims, minor oxide inclusions, minor clumping
plag. – small/medium (0.25 mm) rectangular laths, albite twinning

DV-08-84
Minor vesiculation
90% matrix (70% plag., 30% glass)
10% phenocrysts (95% ol., 5% plag.)
- several partially resorbed feldspar xenocrysts (1 mm)
ol. – eu/subhedral, mostly large (1-2 mm), some small (<0.25 mm), minor alteration to iddingsite, minor clumping

plag. –small (<0.25 mm), rectangular laths, albite twinning

<u>DV-08-86</u>
Minor vesiculation
70% matrix (50% plag., 10% ol., 20% oxides, 20% glass)
30% phenocrysts (50% ol., 45% oxides, 5% plag.)
- lots of badly degraded, resorbed pieces of quartz (0.5-1 mm)
- 2 large partially resorbed plag. with albite twinning (1.5-2 mm)
ol. – large (1-1.5 mm) eu/subhedral and lots of small (0.25 mm) anhedral; almost completely altered to iddingsite, lots of oxide inclusions, very minor clumping
plag. – small (0.25 mm) rectangular laths, albite twinning

<u>DV-08-92</u>
85% matrix (15% ol/idd, 15% oxides, 10% glass, 60% plag.)
15% phenocrysts (95% ol., 5% plag.)
- large quartz glomerocryst with resorbtion edges, xenocrysts (1 mm)
- several partially resorbed feldspar xenocrysts (0.75-1 mm)
ol. – subhedral, mostly large (0.5-0.75 mm), few small (<0.25 mm), some alteration to iddingsite, few oxide inclusions, minor clumping
plag. – mostly small rectangular laths, rare larger clasts, twinning

<u>DV-08-102</u>
Nonvesicular
85% matrix (70% plag., 10% glass, 10% oxides, 10% ol.)
15% phenocrysts (95% ol., 5% plag.)
ol. – sub/anhedral, small/medium (0.5 mm), few larger (0.75-1 mm), partially altered to iddingsite, minor clumping
plag. – mostly small (0.5 mm), rectangular laths, albite twinning

<u>DV-08-116</u>
Minor vesiculation
95% matrix (15% ol., 70% plag., 10% glass, 5% oxide)
5% phenocrysts (99% ol., 1% plag.)
- some amoeboid shaped partially resorbed feldspar and quartz (1-1.5 mm)
ol. – sub/anhedral, large (0.5-1 mm), partially altered to iddingsite, few (1.5-2 mm) glomerocrysts
plag. – small (<0.25 mm), rectangular laths, albite twinning

<u>DV-08-118</u>
Vesicular
95% matrix (60% plag., 30% oxides, 10% ol.)
5% phenocrysts (100% ol.)
ol. – eu/subhedral, mostly small (<0.25 mm), few large (0.75-1 mm), minor alteration to iddingsite, lots of oxide inclusions, few large (1.5-2 mm) gomerocrysts

DV-08-124
Vesicular
80% matrix (20% ol/idd, 80% plag.)
20% phenocrysts (80% ol., 20% plag.)
- large plag./ol. glomerocryst (2 mm)
- several partially resorbed feldspar and plag. (0.75-1 mm)
ol. – sub/anhedral, small (<0.25 mm), rare large (0.5 mm), some alteration to iddingsite
plag. – bimodal small (<0.25 mm) and large (0.5 mm) size distribution, distinct albite twinning, rectangular laths to stubby rectangles

DV-08-125
Vesicular
80% matrix (20% ol, 80% plag.)
20% phenocrysts (80% ol., 20% plag.)
- 1 large partially resorbed plag. xenocrysts with albite twinning (2.5 mm)
- 1 partially resorbed quartz xenocrysts (1 mm)
ol. – anhedral, small (0.25-0.5 mm), some alteration to iddingsite, some clumping
plag. – bimodal small (<0.25 mm) and large (0.5 mm) size distribution, distinct albite twinning, rectangular laths to stubby rectangles

DV-08-130
Minor vesiculation
90% matrix (80% plag., 10% oxides, 10% ol.)
10% phenocrysts (95% ol., 5% plag.)
-some badly resorbed amoeboid quartz and feldspar (0.5 mm)
ol. – eu/subhedral, large (0.5-0.75 mm) altering to iddingsite; lots of small (0.25 mm), anhedral, altered to iddingsite
plag. – mostly small (0.25 mm) rectangular laths, some stubby rectangular, few larger (0.5 mm) laths, albite twinning

DV-08-132A
Minor vesiculation
80% matrix (80% plag., 20% glass) vague orientation
20% phenocrysts (95% ol., 5% plag.)
- large xenocrystic partially resorbed quartz glomerocryst (1.5 mm)
- several partially resorbed feldspar xenocrysts (1 mm)
ol. – eu/subhedral, abundant small (0.25-0.5 mm), some large (0.75 mm), some alteration to iddingsite, minor oxide inclusions
plag. – mostly small (<0.25 mm), rare large (0.5 mm), rectangular laths, distinct albite twinning

DV-08-133
Vesicular
95% matrix (90% plag., 10% oxides)
5% phenocrysts (95% ol., 5% plag.)
- several large (1-2 mm) partially resorbed plag. and quartz

ol. – anhedral, small (0.25-0.5 mm), almost no alteration to iddingsite, lots of clumping, not in equilibrium with surroundings
plag. – few large (0.5-1 mm) twinned laths, not in equilibrium with surroundings

DV-08-134
Nonvesicular
90% matrix (80% plag., 10% oxides, 10% ol.)
10% phenocrysts (98% ol., 2% plag.)
- several smaller partially resorbed feldspar and plag. (~1.5 mm)
ol. – mostly anhedral, small (<0.25 mm), altered to iddingsite; few eu/subhedral, large (1-1.5 mm)
plag. – small (0.25 mm), rectangular laths, albite twinning

DV-08-138
Nonvesicular
80% matrix (15% ol., 15% oxides, 70% plag.) oriented
20% phenocrysts (95% ol., 5% plag.)
ol. – plentiful small (0.25-0.5 mm), anhedral, completely altered to iddingsite; rare large (1-1.5 mm), anhedral, partially altered to iddingsite
plag. – mostly small (0.25-0.5 mm), rectangular laths, albite twinning; few stubby, faded extinction twinning

DV-08-144
Nonvesicular
90% matrix (90% plag., 5% ol., 5% oxides)
10% phenocrysts (95% ol., 5% plag.)
ol. – sub/anhedral, mostly altered to iddingsite, some clumping, bimodal size distribution (0.25, 0.75 mm)
plag. – rectangular laths, albite twinning (0.5 mm)

APPENDIX B

SAMPLE LOCATIONS

Sample	elevation	latitude	longitude	Easting	Northing
DV01	895	N36°20'35.04"	W116°37'48.3"	533195	4022064
DV02	907	N36°20'32.22"	W116°37'52.92"	533080	4021977
DV03	1056	N36°20'26.04"	W116°38'26.46"	532245	4021783
DV04S	1066	N36°20'28.98"	W116°38'34.98"	531808	4021872
DV05	954	N36°20'56.58"	W116°39'12.06"	531105	4022720
DV06	1060	N36°20'6.24"	W116°39'1.44"	531375	4021170
DV07	1234	N36°19'19.44"	W116°38'47.16"	531736	4019729
DV8	1301	N36°18'59.76"	W116°38'56.7"	531500	4019122
DV9	1301	N36°18'59.76"	W116°38'56.7"	531500	4019122
DV10	1059	N36°19'34.32"	W116°38'21.24"	532380	4020468
DV11	1059	N36°19'34.32"	W116°38'21.24"	53238	4020468
DV12	1082	N36°19'36.72"	W116°38'23.88"	532315	4020264
DV-07-13	---	N36°19'37.10"	W116°38'9.88"	532664	4020277
DV-07-14	---	N36°19'35.03"	W116°37'54.91"	533037	4020215
DV-07-15	---	N36°19'33.72"	W116°37'57.39"	532975	4020174
DV-07-16	---	N36°19'38.21"	W116°38'12.24"	532605	4020311
DV-07-17	---	N36°21'29.77"	W116°39'6.70"	531234	4023743
DV-18-07	973	N36°21'0.0"	W116°39'13.1"	531078	4022825
DV-19-07	947	N36°20'59.6"	W116°39'13.6"	531066	4022813
DV-20-07	1068	N36°20'29.7"	W116°38'44.4"	531797	4021894
DV-08-21	1117	N36°19'8.8"	W116°38'28.9"	532193	4019403
DV-08-22	1108	N36°19'14.0"	W116°38'30.4"	532155	4019563
DV-08-23	1159	N36°19'10.0"	W116°38'33.5"	532078	4019440
DV-08-24	1151	N36°19'5.8"	W116°38'38.3"	531959	4019310
DV-08-25	1265	N36°18'6.5"	W116°38'38.8"	531953	4017483
DV-08-26	---	N36°19'0.9"	W116°38'54.8"	531548	4019157
DV-08-27	---	N36°18'54.7"	W116°38'51.3"	531636	4018967
DV-08-28	---	N36°18'52.2"	W116°38'43.3"	531835	4018890
DV-08-29	1256	N36°18'4.6"	W116°38'36.8"	532003	4017424
DV-08-30	1168	N36°18'2.3"	W116°38'20.2"	532417	4017355
DV-08-31	1177	N36°18'1.3"	W116°38'17.5"	532485	4017325
DV-08-32	1212	N36°18'5.8"	W116°38'25.1"	532295	4017462
DV-08-33	1277	N36°18'25.9"	W116°38'48.7"	531704	4018080
DV-08-34	1285	N36°18'27.2"	W116°38'48.9"	531699	4018120
DV-08-35	1308	N36°18'30.6"	W116°38'59.2"	531441	4018223
DV-08-36	1299	N36°18'33.7"	W116°38'52.8"	531601	4018320
DV-08-37	1298	N36°18'34.5"	W116°38'53.2"	531591	4018344
DV-08-38	1281	N36°18'37.9"	W116°38'51.6"	531630	4018449
DV-08-39	1281	N36°18'28.2"	W116°38'40.7"	531903	4018151
DV-08-40	1296	N36°18'33.6"	W116°38'27.8"	532224	4018319
DV-08-41	815	N36°19'13.56"	W116°39'9.6"	531177	4019546

Sample	elevation	latitude	longitude	Easting	Northing
DV-08-42	827	N36°19'13.3"	W116°39'9.9"	531170	4019538
DV-08-43	1092	N36°18'54.6"	W116°40'1.1"	529895	4018957
DV-08-44	1170	N36°18'52.6"	W116°39'57.4"	529988	4018896
DV-08-45	1196	N36°18'52.7"	W116°39'56.2"	530018	4018899
DV-08-46	1205	N36°18'53.1"	W116°39'56.6"	530008	4018912
DV-08-47	1214	N36°18'53.1"	W116°39'55.8"	530027	4018912
DV-08-48	1220	N36°18'53.1"	W116°39'55.9"	530025	4018912
DV-08-49	1227	N36°18'53.2"	W116°39'55.1"	530045	4018915
DV-08-50	1243	N36°18'53.3"	W116°39'54.3"	530065	4018918
DV-08-51	1177	N36°18'28.9"	W116°39'42.2"	530369	4018167
DV-08-52	1230	N36°18'27.2"	W116°39'56.1"	530023	4018114
DV-08-53	1215	N36°18'19.6"	W116°39'51.8"	530131	4017880
DV-08-54	1226	N36°18'19.3"	W116°39'51.3"	530143	4017871
DV-08-55	1256	N36°18'30.9"	W116°39'22.1"	530143	4017957
DV-08-56	1241	N36°17'52.7"	W116°38'46.4"	531765	4017057
DV-08-57	1242	N36°17'51.3"	W116°38'46.6"	532758	4017017
DV-08-58	1253	N36°17'51.4"	W116°38'47.4"	531740	4017017
DV-08-59	1265	N36°17'51.3"	W116°38'47.9"	531728	4017014
DV-08-60	1218	N36°18'12.0"	W116°38'12.4"	532611	4017655
DV-08-61	1138	N36°18'21.1"	W116°36'57.2"	534485	4017942
DV-08-62A	1107	N36°18'29.7"	W116°36'43.3"	534831	4018209
DV-08-62	1140	N36°18'15.0"	W116°36'57.3"	534483	4017754
DV-08-63	1185	N36°17'10.2"	W116°36'25.7"	535279	4015761
DV-08-64	1166	N36°17'12.7"	W116°36'23.3"	535339	4015838
DV-08-65	1182	N36°17'19.5"	W116°36'22.3"	535363	4016048
DV-08-66	1146	N36°17'25.3"	W116°36'37.9"	534973	4016225
DV-08-67	1152	N36°18'7.6"	W116°37'36.2"	533514	4017523
DV-08-68	1052	N36°20'6.4"	W116°39'1.2"	531406	4021175
DV-08-69	872	N36°17'2.8"	W116°32'59.1"	540434	4015555
DV-08-70	877	N36°17'1.9"	W116°32'58.4"	540452	4015528
DV-08-71	839	N36°16'41.5"	W116°32'20.7"	541395	4014904
DV-08-72	834	N36°16'40.9"	W116°32'22.1"	541360	4014885
DV-08-73	857	N36°15'22.5"	W116°31'29.9"	542674	4012476
DV-08-74	1045	N36°11'23.1"	W116°33'39.6"	539471	4005084
DV-08-75	1087	N36°10'46.9"	W116°33'32.9"	539644	4003970
DV-08-76	1085	N36°11'20.0"	W116°33'58.5"	540247	4004992
DV-08-77	835	N36°21'32.6"	W116°39'10.7"	531134	4023830
DV-08-78	930	N36°20'20.3"	W116°35'49.0"	536170	4021622
DV-08-79	1090	N36°20'26.0"	W116°38'32.8"	532087	4021782
DV-08-80	1133	N36°17'14.0"	W116°36'38.3"	534965	4015877
DV-08-81	1191	N36°16'50.7"	W116°36'30.6"	535160	4015160
DV-08-82	1203	N36°16'51.6"	W116°36'37.9"	534977	4015187
DV-08-83	1216	N36°16'53.1"	W116°36'45.5"	534788	4015232
DV-08-84	1250	N36°16'43.1"	W116°36'54.0"	534577	4014923
DV-08-85	1266	N36°16'22.4"	W116°36'46.0"	534779	4014286

Sample	elevation	latitude	longitude	Easting	Northing
DV-08-86	1261	N36°16'21.7"	W116°36'46.6"	534764	4014264
DV-08-87	1291	N36°16'4.7"	W116°36'48.7"	534714	4013740
DV-08-88	1348	N36°15'42.1"	W116°37'16.1"	534033	4013041
DV-08-89	1317	N36°16'10.3"	W116°37'22.4"	533872	4013910
DV-08-90	1342	N36°16'12.5"	W116°37'19.2"	533952	4013978
DV-08-91	1314	N36°16'3.8"	W116°37'6.5"	534270	4013711
DV-08-92	1292	N36°16'42.0"	W116°37'8.0"	534228	4014888
DV-08-93	1264	N36°16'38.9"	W116°37'1.5"	534390	4014793
DV-08-94	1260	N36°16'39.2"	W116°37'1.8"	534383	4014802
DV-08-95	1239	N36°16'32.4"	W116°37'43.0"	533356	4014589
DV-08-96	1271	N36°16'38.0"	W116°38'4.3"	532824	4014759
DV-08-97	1260	N36°16'44.4"	W116°37'48.6"	533214	4014958
DV-08-98	1205	N36°17'1.1"	W116°37'36.2"	533522	4015474
DV-08-99	1201	N36°17'17.5"	W116°38'0.8"	532906	4015977
DV-08-100	1184	N36°16'51.3"	W116°37'20.5"	533915	4015173
DV-08-101	1164	N36°16'56.8"	W116°37'22.8"	533857	4015342
DV-08-102	1176	N36°16'58.4"	W116°37'23.4"	533841	4015392
DV-08-103	1261	N36°16'46.0"	W116°37'24.4"	533818	4015009
DV-08-104	1202	N36°17'3.1"	W116°36'51.0"	534649	4015540
DV-08-105	1158	N36°17'25.2"	W116°36'53.5"	534584	4016220
DV-08-106	1178	N36°18'1.7"	W116°37'49.7"	533178	4017339
DV-08-107	1161	N36°17'54.5"	W116°38'10.6"	532658	4017116
DV-08-108	1159	N36°17'55.7"	W116°38'10.9"	532650	4017153
DV-08-109	1259	N36°18'43.0"	W116°38'27.5"	532230	4018608
DV-08-110	1278	N36°19'10.3"	W116°38'55.6"	531527	4019447
DV-08-111	1158	N36°19'15.5"	W116°38'30.6"	532149	4019610
DV-08-112	1129	N36°19'17.1"	W116°38'26.8"	532244	4019659
DV-08-113	1115	N36°19'20.1"	W116°38'27.1"	532236	4019752
DV-08-114	1111	N36°19'19.8"	W116°38'27.4"	532229	4019742
DV-08-115	1101	N36°19'20.2"	W116°38'25.4"	532279	4019755
DV-08-116	1155	N36°19'35.1"	W116°37'53.2"	533080	4020217
DV-08-117	1152	N36°19'35.2"	W116°37'52.1"	533107	4020220
DV-08-118	1091	N36°19'36.6"	W116°37'42.6"	533344	4020264
DV-08-119	1057	N36°19'47.0"	W116°37'46.2"	533253	4020584
DV-08-120	1048	N36°19'51.9"	W116°37'50.8"	533138	4020735
DV-08-121	1038	N36°19'55.9"	W116°37'55.4"	533022	4020858
DV-08-122	936	N36°16'17.0"	W116°34'39.8"	537928	4014133
DV-08-123	938	N36°16'16.3"	W116°34'44.3"	537816	4014111
DV-08-124	3794	N36°15'14.6"	W116°29'56.3"	545011	4012244
DV-08-125	3797	N36°15'24.0"	W116°29'59.1"	544940	4012533
DV-08-126	4643	N36°16'10.0"	W116°34'25.9"	538276	4013919
DV-08-127	4643	N36°16'10.0"	W116°34'25.9"	538276	4013919
DV-08-128	872	N36°20'11.1"	W116°35'57.3"	535965	4021338
DV-08-129	1086	N36°18'54.8"	W116°35'52.8"	536087	4018987
DV-08-130	1110	N36°18'56.6"	W116°35'48.8"	536186	4019043

Sample	elevation	latitude	longitude	Easting	Northing
DV-08-131	976	N36°18'45.4"	W116°34'48.3"	537696	4018704
DV-08-132A	947	N36°18'49.9"	W116°34'54.0"	537554	4018842
DV-08-132B	957	N36°19'6.0"	W116°34'58.0"	537452	4019338
DV-08-133	735	N36°11'51.6"	W116°24'8.8"	553722	4006038
DV-08-134	687	N36°11'59.4"	W116°24'25.2"	553311	4006276
DV-08-135	653	N36°11'42.5"	W116°22'29.8"	556196	4005774
DV-08-136	689	N36°11'44.6"	W116°22'51.8"	555646	4005835
DV-08-137	675	N36°11'43.2"	W116°22'56.3"	555534	4005791
DV-08-138	679	N36°11'43.9"	W116°22'59.0"	555466	4005812
DV-08-139	656	N36°11'37.1"	W116°22'41.6"	555902	4005605
DV-08-140	605	N36°11'32.8"	W116°22'0.6"	556927	4005480
DV-08-141	605	N36°11'32.8"	W116°22'0.6"	556927	4005480
DV-08-142	611	N36°11'32.1"	W116°21'59.7"	556950	4005458
DV-08-143	606	N36°11'39.3"	W116°22'8.8"	556721	4005678
DV-08-144	1217	N36°18'54.1"	W116°38'37.8"	531972	4018949
DV-08-145	1300	N36°16'1.8"	W116°36'53.9"	534584	4013651
DV-08-146	1339	N36°15'43.4"	W116°37'5.5"	534297	4013083
DV-08-147	1306	N36°15'40"	W116°37'4.7"	534317	4012978
DV-08-148	1310	N36°15'23.8"	W116°36'50.7"	534669	4012480
DV-08-149	1271	N36°16'12.3"	W116°36'46.9"	534758	4013975
DV-08-150	1120	N36°10'51.4"	W116°32'57.3"	540532	4004112
DV-08-151	1149	N36°10'0.3"	W116°33'36.5"	539560	4002533
DV-08-152	1090	N36°12'56.6"	W116°30'52.5"	543630	4007985
DV-08-153	1018	N36°13'29.2"	W116°30'19.3"	544454	4008994
DV-08-154	1021	N36°12'33.9"	W116°28'51.6"	546652	4007301
DV-08-155	1038	N36°12'30.8"	W116°29'2.2"	546388	4007204
DV-08-156	1044	N36°12'34.4"	W116°28'51.5"	546655	4007317
DV-08-157	987	N36°12'34.9"	W116°28'55.9"	546545	4007331

APPENDIX C

MAJOR ELEMENT DATA (IN WT. %)

The data reported in this appendix were obtained on a Panalytical Axios Advanced X-ray Fluorescence Spectrometer (XRF) at the University of Nevada Las Vegas. Data are reported as provided by the laboratory with no adjustment for significant figures.

	DV01	**DV02**	**DV03**	**DV05**	**DV06**	**DV07**
SiO_2	50.75	47.32	51.2	50.65	51.07	49.45
Al_2O_3	17.18	15.31	16.75	16.42	16.86	16.27
TiO_2	1.63	2.51	1.7	1.77	1.79	2.35
Fe_2O_3	9.2	13.15	10.22	10.3	10.67	11.99
MgO	5.34	6.08	4.78	5.03	4.95	4.83
Na_2O	3.92	3.76	3.2	3.65	3.33	3.2
K_2O	1.51	1.9	1.82	1.73	1.75	1.94
MnO	0.14	0.17	0.15	0.15	0.15	0.17
CaO	8.89	8.47	8.75	8.42	8.49	8.49
P_2O_5	0.55	0.88	0.78	0.82	0.76	0.75
Total	99.1	99.55	99.35	98.94	99.83	99.44

	DV9	**DV11**	**DV12**	**DV-07-13**	**DV-07-15**	**DV-07-16**
SiO_2	48.19	47.46	48.24	51.94	51.04	51.22
Al_2O_3	15.87	15.44	15.57	17.24	17.1	16.73
TiO_2	2.45	2.6	2.45	1.57	1.59	1.58
Fe_2O_3	12.65	12.66	12.6	10.17	10.7	9.93
MgO	4.99	5.74	5.36	4.7	5.26	4.78
Na_2O	3.23	3.64	3.39	3.33	3.39	3.59
K_2O	1.94	2	1.86	1.81	1.64	1.75
MnO	0.17	0.17	0.17	0.15	0.16	0.15
CaO	8.64	8.68	8.5	7.99	8.34	8.14
P_2O_5	0.88	0.88	0.95	0.81	0.83	0.87
Total	99.01	99.27	99.09	99.72	100.04	98.74

	DV-07-17	DV-07-18	DV-07-19	DV-07-20	DV-08-22	DV-08-26
SiO_2	51.21	51.16	50.8	51.43	47.34	47.47
Al_2O_3	17	16.8	16.71	16.91	15.99	15.9
TiO_2	1.83	1.77	1.91	1.72	2.5	2.61
Fe_2O_3	10.48	10.18	10.5	9.99	12.45	13.33
MgO	5.02	4.92	4.97	4.51	6.33	6.01
Na_2O	3.69	3.52	3.47	3.37	4.2	3.3
K_2O	1.79	1.66	1.72	1.87	1.51	2.03
MnO	0.15	0.15	0.16	0.15	0.16	0.18
CaO	8.03	8.34	8.29	8.55	7.84	8.23
P_2O_5	0.76	0.77	0.74	0.78	0.62	0.76
Total	99.96	99.27	99.26	99.27	98.94	99.81

	DV-08-27	DV-08-28	DV-08-29	DV-08-30	DV-08-31	DV-08-32
SiO_2	48.26	48.07	51.06	49.43	49.32	52.11
Al_2O_3	15.88	15.78	16.54	16.32	16.28	16.38
TiO_2	2.61	2.5	1.86	2.27	2.26	1.75
Fe_2O_3	13.37	13.43	10.32	11.45	11.85	9.66
MgO	5.86	6.64	5.96	5.05	5.3	5.79
Na_2O	3.32	2.99	3.36	3.76	3.65	3.43
K_2O	1.92	1.87	1.84	2.25	2.22	1.98
MnO	0.18	0.18	0.15	0.16	0.16	0.14
CaO	8.42	8.5	8.41	8.1	7.97	8.02
P_2O_5	0.87	0.85	0.56	0.72	0.72	0.52
Total	100.69	100.8	100.06	99.5	99.73	99.78

	DV-08-34	DV-08-35	DV-08-36	DV-08-37	DV-08-38	DV-08-39
SiO_2	49.83	49.41	49.35	50.1	47.63	49.63
Al_2O_3	16.24	16.19	16.29	16.46	15.75	16.39
TiO_2	2.03	2.01	2.05	2.06	2.48	2.08
Fe_2O_3	11.41	11.14	11.59	11.63	13.18	11.97
MgO	5.28	5.27	5.18	5.22	5.72	5.45
Na_2O	3.62	3.27	3.56	3.22	3.01	3.35
K_2O	1.93	1.83	1.88	1.9	1.89	1.86
MnO	0.16	0.16	0.17	0.16	0.19	0.16
CaO	8.17	8.72	8.39	8.11	8.94	7.77
P_2O_5	0.93	0.96	0.95	0.94	0.85	0.93
Total	99.61	98.96	99.4	99.8	99.64	99.6

	DV-08-40	DV-08-41	DV-08-42	DV-08-43	DV-08-44	DV-08-45
SiO_2	50.99	46.81	46.47	47.81	47.17	47.38
Al_2O_3	17.35	15.91	15.74	15.88	15.81	15.68
TiO_2	1.83	2.73	2.73	2.52	2.6	2.5
Fe_2O_3	10.08	13.39	13.54	13.19	13.2	13.24
MgO	3.95	6.51	6.42	6.27	6.28	5.82
Na_2O	3.46	3.24	3.15	3.52	3.22	3.7
K_2O	1.94	2.2	2.12	1.93	2.01	1.92
MnO	0.16	0.17	0.17	0.18	0.18	0.18
CaO	8.58	8.29	8.33	8.33	8.26	8.48
P_2O_5	0.88	0.63	0.69	0.83	0.76	0.84
Total	99.22	99.87	99.36	100.45	99.49	99.74

	DV-08-46	DV-08-47	DV-08-48	DV-08-49	DV-08-50	DV-08-51
SiO_2	47.83	48.09	48.2	47.92	48.43	49.78
Al_2O_3	15.92	15.48	15.65	15.8	16	16.35
TiO_2	2.63	2.61	2.59	2.55	2.5	2.2
Fe_2O_3	12.82	13.08	12.57	12.77	12.77	11.54
MgO	5.81	5.57	5.58	5.39	5.44	4.68
Na_2O	3.19	3.15	3.14	3.15	3.3	3.39
K_2O	1.97	1.94	1.89	1.95	1.88	1.86
MnO	0.17	0.17	0.17	0.18	0.18	0.16
CaO	8.65	8.54	8.59	8.4	8.55	8.54
P_2O_5	0.85	0.83	0.84	0.88	0.9	0.97
Total	99.85	99.46	99.21	98.99	99.95	99.47

	DV-08-52	DV-08-53	DV-08-54	DV-08-55	DV-08-56	DV-08-57
SiO_2	49.71	48.5	49.61	49.45	51.64	51.74
Al_2O_3	16.37	16.11	16.26	16.27	16.41	16.68
TiO_2	2.01	2.33	2.16	2.01	1.77	1.76
Fe_2O_3	11.55	12.61	11.21	11.25	9.8	9.7
MgO	5.12	5.13	4.59	5.44	6.27	6.18
Na_2O	3.64	3.25	3.51	3.54	3.49	3.34
K_2O	1.92	1.88	1.9	1.82	1.74	1.73
MnO	0.16	0.17	0.16	0.16	0.15	0.15
CaO	8.46	8.6	8.7	8.51	8.45	8.49
P_2O_5	0.93	1.05	0.96	0.96	0.52	0.51
Total	99.87	99.63	99.06	99.41	100.24	100.27

	DV-08-58	DV-08-59	DV-08-60	DV-08-61	DV-08-62	DV-08-63
SiO_2	51.74	51.53	50.75	52.39	49.62	50
Al_2O_3	16.33	16.43	16.95	17.37	17.76	18.03
TiO_2	1.75	1.83	1.86	1.43	1.84	1.36
Fe_2O_3	9.8	10.19	10.43	8.98	9.79	8.87
MgO	5.69	5.83	4.79	4.85	5.63	6.36
Na_2O	3.23	3.37	3.41	3.48	3.92	3.4
K_2O	1.73	1.84	1.79	1.39	1.14	1.2
MnO	0.14	0.15	0.16	0.15	0.16	0.13
CaO	8.69	8.37	8.35	8.72	9.58	10.64
P_2O_5	0.51	0.54	0.88	0.39	0.49	0.38
Total	99.62	100.08	99.36	99.14	99.94	100.37

	DV-08-64	DV-08-65	DV-08-66	DV-08-67	DV-08-68	DV-08-69
SiO_2	49	48.74	47.54	50.4	51.23	49.59
Al_2O_3	18.23	18.07	17.94	18.03	17.12	17.04
TiO_2	1.51	1.52	1.48	1.41	1.82	1.52
Fe_2O_3	9.73	9.18	9.3	9.11	10.59	8.98
MgO	6.39	6.96	5.79	6.73	5.13	7.78
Na_2O	3.41	3.56	3.46	3.45	3.42	3.69
K_2O	0.74	0.62	0.53	1.22	1.72	1.1
MnO	0.15	0.15	0.15	0.14	0.16	0.15
CaO	11.1	11.02	13.5	9.68	8.63	9.83
P_2O_5	0.36	0.37	0.34	0.39	0.79	0.48
Total	100.62	100.2	100.02	100.55	100.61	100.16

	DV-08-70	DV-08-72	DV-08-74	DV-08-75	DV-08-76	DV-08-77
SiO_2	49.91	50.87	47.87	56.27	48.27	50.92
Al_2O_3	17.32	16.14	17.5	19.15	14.53	17.01
TiO_2	1.69	1.5	1.66	0.96	1.1	1.86
Fe_2O_3	9.4	9.42	10.44	5.77	8.46	10.72
MgO	7.62	7.64	7.65	3.84	12.18	5.05
Na_2O	4.28	3.46	3.78	3.69	2.95	3.53
K_2O	1.14	1.61	0.74	1.8	1.09	1.77
MnO	0.16	0.15	0.17	0.09	0.14	0.16
CaO	8.42	8.49	10.24	8.02	10.59	8.14
P_2O_5	0.56	0.56	0.52	0.22	0.56	0.77
Total	100.49	99.84	100.58	99.81	99.87	99.92

	DV-08-78	DV-08-79	DV-08-80	DV-08-81	DV-08-83	DV-08-84
SiO_2	49.24	51.98	50.25	50.54	51.28	49.41
Al_2O_3	17.31	17.27	17.06	17.09	17	16.76
TiO_2	2.2	1.76	1.87	1.83	1.76	1.88
Fe_2O_3	10.87	9.94	10.62	10.62	10.32	11.08
MgO	6.22	4.3	5.3	5.14	5.08	5.69
Na_2O	3.68	3.51	3.46	3.79	3.5	4.11
K_2O	1.79	1.95	1.86	1.92	1.99	1.9
MnO	0.16	0.15	0.16	0.16	0.15	0.16
CaO	8.12	8.54	8.36	8.37	8.09	8.27
P_2O_5	0.46	0.83	0.83	0.82	0.8	0.83
Total	100.04	100.23	99.77	100.28	99.98	100.1

	DV-08-86	DV-08-87	DV-08-88	DV-08-89	DV-08-91	DV-08-92
SiO_2	49.42	49.8	72.02	52.91	48.5	53.32
Al_2O_3	16.59	16.99	14.44	17.2	16.25	17.03
TiO_2	1.89	1.85	0.262	1.33	2.4	1.29
Fe_2O_3	11.25	10.45	1.96	8.9	11.95	8.39
MgO	5.37	5.08	0.1	5.33	5.19	5.48
Na_2O	3.39	4.1	3.43	3.31	3.41	3.41
K_2O	1.82	1.84	4.37	1.58	2.41	1.8
MnO	0.16	0.16	0.051	0.13	0.16	0.13
CaO	9.28	8.69	3.39	8.48	8.05	7.99
P_2O_5	0.81	0.85	0.118	0.62	0.67	0.59
Total	99.98	99.81	100.141	99.8	98.99	99.42

	DV-08-93	DV-08-95	DV-08-96	DV-08-97	DV-08-98	DV-08-99
SiO_2	52.44	52.29	49.02	53.73	53.63	53.44
Al_2O_3	16.3	17.25	16.61	17.2	17.25	17.1
TiO_2	1.84	1.37	2.44	1.29 1.29	1.29	
Fe_2O_3	10.44	8.56	12.07	8.45	8.19	8.31
MgO	4.88	5.07	4.18	5.44	5.39	5.28
Na_2O	3.81	3.32	3.71	3.7	3.49	3.58
K_2O	1.97	1.76	2.55	1.81	1.91	1.61
MnO	0.15	0.14	0.16	0.13	0.13	0.13
CaO	7.42	8.78	8.44	7.97	7.99	8.42
P_2O_5	0.76	0.66	0.69	0.6	0.61	0.6
Total	100.01	99.2	99.86	100.32	99.88	99.76

	DV-08-101	DV-08-102	DV-08-103	DV-08-104	DV-08-105	DV-08-106
SiO_2	47.36	47.78	53.26	50.66	51.25	50.33
Al_2O_3	17.35	17.61	17.14	16.55	16.8	16.68
TiO_2	1.91	1.869	1.32	1.76	1.74	1.88
Fe_2O_3	11.12	10.44	8.45	10.84	10.1	10.79
MgO	6.68	7.11	5.26	5.03	4.47	5.09
Na_2O	4.26	3.92	3.52	3.73	3.5	3.4
K_2O	0.62	0.73	1.8	1.96	2.08	1.75
MnO	0.17	0.172	0.13	0.15	0.15	0.16
CaO	9.24	9.79	8.44	8.27	8.42	8.3
P_2O_5	0.76	0.714	0.62	0.78	0.78	0.9
Total	99.47	100.13	99.94	99.73	99.29	99.28

	DV-08-107	DV-08-108	DV-08-109	DV-08-110	DV-08-111	DV-08-112
SiO_2	49.6	52.55	50.7	48.07	47.14	47.54
Al_2O_3	16.31	17.7	17.01	15.97	16.02	16.22
TiO_2	2.25	1.44	1.82	2.49	2.67	2.57
$Fe2O_3$	11.64	9.07	10.95	12.82	13.55	12.64
MgO	5.04	5.42	4.74	5.07	6.45	6.42
Na_2O	3.55	3.56	3.5	3.16	3.81	3.88
K_2O	2.31	1.22	1.83	1.94	1.31	1.87
MnO	0.16	0.15	0.16	0.18	0.17	0.17
CaO	7.93	8.56	8.53	8.78	8.32	7.96
P_2O_5	0.7	0.41	0.87	0.9	0.62	0.62
Total	99.49	100.07	100.11	99.39	100.06	99.89

	DV-08-114	DV-08-116	DV-08-118	DV-08-119	DV-08-120	DV-08-121
SiO_2	48.11	51.86	51.07	52.1	52.25	52.85
Al_2O_3	15.97	17.46	17.07	17.69	17.81	17.83
TiO_2	2.49	1.51	1.56	1.51	1.51	1.51
Fe_2O_3	12.42	9.58	9.91	8.92	8.98	9.12
MgO	6.14	4.85	5.47	4.2	4.71	4.29
Na_2O	3.82	3.64	3.44	3.62	3.61	3.55
K_2O	1.45	1.77	1.56	1.64	1.68	1.81
MnO	0.16	0.16	0.16	0.15	0.15	0.15
CaO	8.13	7.91	8	8.59	8.36	8.19
P_2O_5	0.61	0.74	0.77	0.74	0.75	0.75
Total	99.3	99.48	99	99.16	99.81	100.05

	DV-08-122	DV-08-123	DV-08-124	DV-08-125	DV-08-127	DV-08-128
SiO_2	51.31	49.02	50.82	50.73	50.22	48.28
Al_2O_3	16.87	16.79	16.93	16.6	17.27	17.01
TiO_2	1.67	2.46	1.45	1.41	1.74	2.36
Fe_2O_3	10.32	10.96	9.57	9.26	10.91	11.25
MgO	5.61	4.16	7.3	7.3	4.6	5.63
Na_2O	3.27	3.87	3.63	3.14	3.39	3.4
K_2O	1.82	1.86	0.85	0.72	1.89	1.78
MnO	0.15	0.14	0.16	0.15	0.15	0.16
CaO	8.03	9.04	9.37	10.14	8.26	8.78
P_2O_5	0.81	0.63	0.24	0.24	0.86	0.47
Total	99.86	98.93	100.32	99.68	99.29	99.11

	DV-08-130	DV-08-132A	DV-08-132B	DV-08-133	DV-08-134	DV-08-135
SiO_2	51.43	51.86	51.45	65.27	54.95	49.41
Al_2O_3	17.5	16.74	17.46	15.7	17.45	18.12
TiO_2	1.68	1.55	1.68	0.57	1.15	1.43
Fe_2O_3	9.24	9.3	9.59	4.06	6.96	9.18
MgO	5.34	6.54	5.43	2.96	4.87	6.64
Na_2O	3.92	3.45	3.89	4.04	3.54	3.3
K_2O	1.6	1.33	1.59	3.47	2.07	0.99
MnO	0.15	0.15	0.15	0.08	0.12	0.15
CaO	8.41	8.5	8.21	4.16	8.53	10.72
P_2O_5	0.58	0.45	0.57	0.19	0.34	0.39
Total	99.85	99.87	100.02	100.5	99.99	100.33

	DV-08-136	DV-08-138	DV-08-139	DV-08-140	DV-08-142	DV-08-143
SiO_2	49.61	49.25	49.69	49.57	47.74	51.64
Al_2O_3	18.04	18.09	18.04	18.55	17.52	17.27
TiO_2	1.45	1.43	1.42	1.47	1.79	1.5
Fe_2O_3	9.29	8.96	8.91	9.02	10.05	8.41
MgO	6.4	6.53	6.63	5.78	6.78	5.93
Na_2O	3.28	3.27	3.19	3.3	3.32	3.71
K_2O	1.05	1	1	1.05	0.97	1.56
MnO	0.15	0.15	0.15	0.15	0.17	0.14
CaO	10.67	10.76	10.69	10.75	11.08	9.7
P_2O_5	0.41	0.39	0.39	0.41	0.6	0.48
Total	100.34	99.82	100.11	100.04	100.01	100.34

	DV-08-144	DV-08-145	DV-08-146	DV-08-148	DV-08-149	DV-08-150
SiO_2	47.5	48.59	71.91	50.67	50.34	50.17
Al_2O_3	15.83	16.98	14.47	18.48	16.99	16.76
TiO_2	2.61	1.967	0.275	1.509	1.861	1.471
Fe_2O_3	12.98	11.16	2.06	9.58	10.7	8.82
MgO	6.14	4.99	0.7	5.94	5.04	8.04
Na_2O	3.4	3.43	3.45	3.69	3.62	3.43
K_2O	1.94	1.7	4.4	0.84	1.88	1.3
MnO	0.18	0.169	0.052	0.154	0.155	0.156
CaO	8.28	9.67	2.93	9.28	9.01	9.29
P_2O_5	0.85	0.892	0.107	0.364	0.827	0.429
Total	99.71	99.55	100.35	100.51	100.42	99.87

	DV-08-151	DV-08-152	DV-08-153	DV-08-154	DV-08-155	DV-08-157
SiO_2	56.52	50.95	52.34	51.85	52.05	52.46
Al_2O_3	19.6	17	17.02	16.59	16.73	16.86
TiO_2	0.98	1.73	1.31	1.51	1.51	1.51
Fe_2O_3	6.02	9.14	8.74	8.69	9.13	8.69
MgO	3.92	6.86	6.82	6.53	6.61	6.24
Na_2O	3.45	3.81	3.65	3.86	3.62	3.84
K_2O	1.68	1.34	1.23	1.74	1.61	1.74
MnO	0.10	0.15	0.15	0.15	0.15	0.15
CaO	8.27	8.59	8.77	8.19	8.06	8.16
P_2O_5	0.24	0.49	0.41	0.48	0.49	0.49
Total	100.78	100.07	100.44	99.59	99.96	100.13

APPENDIX D

TRACE ELEMENT DATA (IN PPM)

The data reported in this appendix were obtained on a Panalytical Axios Advanced X-ray Fluorescence Spectrometer (XRF) at the University of Nevada Las Vegas. Data are reported as provided by the laboratory with no adjustment for significant figures.

Sample	**Sc**	**V**	**Ni**	**Cu**	**Ga**	**Rb**	**Sr**	**Y**
DV1	22	202	58	33	18	21	806	21
DV02	24	210	29	43	19	22	945	23
DV03	24	215	30	46	18	27	988	23
DV05	23	265	50	43	19	21	791	26
DV06	21	221	30	47	19	24	950	25
DV07	24	226	20	32	20	20	962	27
DV9	26	305	31	38	19	22	888	25
DV11	25	284	43	49	19	21	798	25
DV-12	23	260	30	44	18	20	923	25
DV-07-13	25	191	28	46	20	25	1002	23
DV-07-15	23	203	57	58	19	23	953	19
DV-07-16	22	201	29	44	18	25	1006	23
DV-07-17	21	227	36	47	20	23	873	24
DV-07-18	24	225	31	44	19	25	953	22
DV-07-19	22	229	33	45	20	24	883	23
DV-07-20	25	276	29	33	20	30	1000	23
DV-08-22	29	335	53	39	16	11	709	19
DV-08-26	27	365	50	38	18	20	762	19
DV-08-27	29	333	39	42	18	21	803	19
DV-08-28	25	323	58	32	17	21	803	19
DV-08-29	26	268	60	41	16	31	633	19
DV-08-30	26	293	29	40	18	27	866	19
DV-08-31	26	306	29	67	19	28	867	19
DV-08-32	21	242	55	37	17	37	607	19
DV-08-34	22	276	38	18	19	26	1026	19
DV-08-35	24	251	41	52	19	19	1096	18
DV-08-36	23	255	41	45	20	24	970	18
DV-08-37	22	302	38	39	19	24	986	18
DV-08-38	26	376	51	3	19	20	818	20
DV-08-39	23	242	39	51	19	24	973	19
DV-08-40	22	229	16	48	20	26	1010	19
DV-08-41	30	356	49	35	17	20	739	19
DV-08-42	26	342	48	36	18	19	754	19
DV-08-43	25	302	52	40	19	22	787	19
DV-08-44	27	304	51	39	17	21	781	20
DV-08-45	27	298	52	43	18	21	804	20
DV-08-46	27	316	39	42	18	19	813	19
DV-08-47	27	334	39	42	18	19	805	19

Sample	Sc	V	Ni	Cu	Ga	Rb	Sr	Y
DV-08-48	28	316	36	41	18	17	824	19
DV-08-49	25	285	34	41	19	22	855	20
DV-08-50	28	295	30	40	19	18	910	20
DV-08-51	24	255	21	36	16	15	833	18
DV-08-52	20	256	35	50	20	24	1051	18
DV-08-53	24	264	31	47	18	17	976	18
DV-08-54	25	245	26	42	19	22	1055	20
DV-08-55	21	240	41	53	19	20	1064	18
DV-08-56	23	245	60	35	16	30	605	18
DV-08-57	22	226	60	31	17	30	613	18
DV-08-58	23	236	58	22	17	28	623	18
DV-08-59	27	233	54	35	17	31	644	19
DV-08-60	24	237	26	45	20	21	1116	18
DV-08-61	30	239	16	20	19	25	674	18
DV-08-62	30	269	44	52	19	13	773	18
DV-08-63	31	223	66	31	16	16	645	15
DV-08-64	33	244	68	45	15	7	614	16
DV-08-65	32	232	68	47	16	5	600	15
DV-08-66	36	284	71	44	14	2	597	15
DV-08-67	27	233	84	38	15	17	621	15
DV-08-68	26	231	28	43	19	24	962	19
DV-08-69	30	232	100	45	17	12	798	17
DV-08-70	25	215	117	36	17	17	656	19
DV-08-72	24	213	134	38	17	21	753	18
DV-08-74	31	257	54	25	17	6	753	18
DV-08-75	18	148	33	34	19	37	798	14
DV-08-76	25	176	279	62	15	20	1006	13
DV-08-77	23	228	34	45	20	23	887	19
DV-08-78	27	321	42	26	18	20	701	18
DV-08-79	26	254	26	44	18	29	945	20
DV-08-80	26	261	37	51	18	24	986	18
DV-08-81	26	251	31	52	19	24	993	18
DV-08-83	22	246	38	47	20	30	949	18
DV-08-84	24	252	47	55	20	26	964	18
DV-08-86	27	293	62	49	19	23	959	17
DV-08-87	24	262	41	50	18	22	994	18
DV-08-88	6	15	3	8	15	109	333	24
DV-08-89	23	206	51	38	19	32	902	17
DV-08-91	27	352	27	41	18	23	907	19
DV-08-92	23	214	60	30	19	31	892	17
DV-08-93	19	226	45	35	19	31	716	19
DV-08-95	22	204	42	34	19	31	953	17
DV-08-96	28	332	23	37	19	28	910	19
DV-08-97	21	199	54	35	19	34	896	17
DV-08-98	20	200	55	30	17	29	896	16

Sample	Sc	V	Ni	Cu	Ga	Rb	Sr	Y
DV-08-99	21	194	55	36	18	36	902	17
DV-08-101	25	251	53	25	16	15	896	19
DV-08-102	28	256	49	21	17	12	861	18
DV-08-103	21	198	50	36	19	32	917	17
DV-08-104	25	254	39	49	18	25	983	18
DV-08-105	25	255	40	50	17	32	942	18
DV-08-106	23	235	40	54	19	22	1011	18
DV-08-107	27	283	27	46	18	30	845	19
DV-08-108	28	230	14	15	18	22	673	18
DV-08-109	24	226	25	42	21	23	1066	19
DV-08-110	26	291	32	42	18	24	900	20
DV-08-111	28	334	49	37	18	20	752	19
DV-08-112	28	341	51	43	17	16	708	19
DV-08-114	26	310	47	40	15	10	644	17
DV-08-116	21	224	39	36	19	27	946	19
DV-08-118	23	219	47	46	20	24	929	18
DV-08-119	24	193	17	33	20	26	931	19
DV-08-120	24	207	27	38	19	22	900	18
DV-08-121	24	198	16	34	21	26	925	19
DV-08-122	21	227	57	42	20	27	1044	18
DV-08-123	32	343	13	34	20	18	971	18
DV-08-124	30	230	78	47	17	15	447	18
DV-08-125	35	226	80	47	15	13	461	18
DV-08-127	24	239	51	38	20	31	1086	18
DV-08-128	29	379	36	36	16	14	906	17
DV-08-130	24	274	57	35	20	24	778	18
DV-08-132A	29	230	75	24	18	20	611	17
DV-08-132B	21	212	58	36	19	24	791	18
DV-08-133	10	71	37	22	16	75	512	19
DV-08-134	22	176	46	44	17	38	633	17
DV-08-135	30	246	57	32	16	10	798	15
DV-08-136	31	246	59	31	18	12	828	15
DV-08-138	32	247	53	30	17	11	804	14
DV-08-139	34	249	60	31	17	11	789	14
DV-08-140	31	254	49	28	16	10	915	14
DV-08-142	29	280	65	39	16	6	993	16
DV-08-143	32	195	67	39	16	17	769	16
DV-08-144	27	322	46	42	19	19	791	19
DV-08-145	22	234	45	49	19	21	1036	21
DV-08-146	7	17	3	7	15	111	329	25
DV-08-148	26	215	67	31	17	13	517	20
DV-08-149	27	250	41	49	18	40	1605	39
DV-08-150	26	213	127	32	15	18	578	20
DV-08-151	17	152	32	31	19	27	823	12
DV-08-152	23	225	108	37	18	20	719	21

Sample	Sc	V	Ni	Cu	Ga	Rb	Sr	Y
DV-08-153	30	215	66	28	15	17	677	20
DV-08-154	26	210	93	46	18	29	705	22
DV-08-155	22	230	94	35	17	29	711	23
DV-08-157	25	228	89	35	18	32	712	22

Sample	Zr	Nb	Ba	La	Hf	Pb	Th
DV01	298	18	828	56	7	4	12
DV02	360	22	1220	69	9	6	13
DV03	371	24	1230	75	10	6	18
DV05	313	21	1004	62	8	4	10
DV06	364	23	1250	77	10	6	16
DV07	363	24	1193	93	10	4	14
DV9	341	24	1148	63	8	0	15
DV11	311	21	1031	49	7	2	12
DV12	349	24	1173	65	8	4	14
DV-07-13	384	25	1338	84	10	7	19
DV-07-15	369	25	1350	95	13	0	20
DV-07-16	387	25	1324	97	9	7	19
DV-07-17	359	24	1145	65	9	7	14
DV-07-18	367	23	1267	90	10	4	17
DV-07-19	358	22	1197	68	9	5	15
DV-07-20	346	22	1612	84	8	6	17
DV-08-22	276	17	859	29	9	2	7
DV-08-26	304	20	987	67	15	---	12
DV-08-27	327	24	1109	81	11	---	11
DV-08-28	321	22	1044	53	10	---	9
DV-08-29	236	16	814	31	7	5	8
DV-08-30	297	20	1089	68	11	6	12
DV-08-31	300	21	1075	54	9	4	14
DV-08-32	229	15	797	42	7	4	8
DV-08-34	381	26	1413	88	18	4	17
DV-08-35	392	25	1712	86	17	7	15
DV-08-36	381	26	1417	88	16	5	15
DV-08-37	386	26	1429	94	18	7	14
DV-08-38	328	23	1155	58	12	4	11
DV-08-39	377	27	1401	99	16	7	16
DV-08-40	388	25	1474	82	15	5	15
DV-08-41	266	17	922	38	8	2	8
DV-08-42	285	19	930	49	10	1	11
DV-08-43	320	22	1024	72	11	4	10
DV-08-44	304	19	989	56	13	3	9
DV-08-45	329	22	1026	74	14	4	11
DV-08-46	325	22	1082	73	11	1	9

Sample	Zr	Nb	Ba	La	Hf	Pb	Th
DV-08-47	333	24	1095	71	13	1	10
DV-08-48	336	23	1098	55	11	3	13
DV-08-49	344	24	1149	74	14	4	13
DV-08-50	357	24	1189	70	16	5	13
DV-08-51	313	24	1416	86	12	5	13
DV-08-52	384	26	1392	81	13	5	16
DV-08-53	381	26	1402	77	17	7	14
DV-08-54	414	29	1394	97	15	4	18
DV-08-55	387	25	1438	82	18	6	13
DV-08-56	220	14	745	51	9	2	8
DV-08-57	218	15	756	56	7	4	10
DV-08-58	233	15	818	30	8	7	8
DV-08-59	236	17	811	28	9	5	11
DV-08-60	395	26	1415	74	16	6	17
DV-08-61	253	12	792	38	10	5	10
DV-08-62	229	14	709	37	7	4	9
DV-08-63	198	11	672	39	6	2	9
DV-08-64	200	9	408	18	6	---	4
DV-08-65	195	9	463	15	6	2	5
DV-08-66	182	9	342	20	3	2	6
DV-08-67	196	11	653	24	6	2	8
DV-08-68	375	23	1354	75	14	6	15
DV-08-69	232	10	707	33	8	2	11
DV-08-70	255	11	642	13	6	2	7
DV-08-72	305	17	1082	67	12	4	14
DV-08-74	236	9	577	11	8	2	7
DV-08-75	208	8	762	36	7	6	11
DV-08-76	188	9	930	36	5	3	11
DV-08-77	372	24	1213	67	14	4	15
DV-08-78	255	15	854	38	10	0	8
DV-08-79	382	24	1382	89	18	8	16
DV-08-80	343	27	1398	66	13	5	15
DV-08-81	343	26	1436	86	15	6	16
DV-08-83	334	26	1396	90	15	8	16
DV-08-84	339	26	1385	63	14	7	16
DV-08-86	325	25	1329	59	16	---	16
DV-08-87	343	26	1441	84	14	---	16
DV-08-88	153	12	1056	28	2	20	14
DV-08-89	288	17	1562	64	8	6	13
DV-08-91	289	19	1334	67	11	---	11
DV-08-92	281	16	1629	72	10	7	15
DV-08-93	304	20	951	54	11	7	11
DV-08-95	302	18	1890	66	11	8	18
DV-08-96	291	19	1046	63	14	2	11
DV-08-97	282	16	1674	61	11	8	15

Sample	Zr	Nb	Ba	La	Hf	Pb	Th
DV-08-98	280	17	1660	70	12	8	14
DV-08-99	283	17	1656	66	10	11	15
DV-08-101	337	21	905	55	13	---	8
DV-08-102	313	20	844	39	11	---	12
DV-08-103	287	18	1675	85	11	10	15
DV-08-104	339	25	1369	83	15	6	15
DV-08-105	327	24	1369	67	13	9	15
DV-08-106	388	25	1455	83	16	7	14
DV-08-107	295	20	1058	54	10	5	10
DV-08-108	255	12	765	42	7	3	9
DV-08-109	396	25	1926	81	16	3	17
DV-08-110	356	25	1228	78	13	3	14
DV-08-111	260	17	877	42	11	3	9
DV-08-112	270	17	860	52	9	3	9
DV-08-114	247	16	880	45	6	2	8
DV-08-116	375	24	1898	79	11	6	19
DV-08-118	375	24	1359	103	16	5	20
DV-08-119	377	23	1413	89	16	8	16
DV-08-120	373	23	1361	94	15	9	17
DV-08-121	379	25	1390	89	18	9	18
DV-08-122	409	31	1589	113	19	10	22
DV-08-123	290	18	1154	48	13	2	12
DV-08-124	202	4	482	12	7	3	6
DV-08-125	194	4	376	9	4	1	5
DV-08-127	428	32	1673	128	20	12	22
DV-08-128	258	17	865	41	7	1	14
DV-08-130	317	20	905	76	9	5	14
DV-08-132A	244	17	855	53	4	1	11
DV-08-132B	316	20	902	58	12	4	11
DV-08-133	235	12	1250	28	7	15	12
DV-08-134	224	12	975	24	6	3	8
DV-08-135	179	11	596	14	8	---	9
DV-08-136	186	11	601	16	7	0	8
DV-08-138	179	10	595	25	5	1	9
DV-08-139	178	11	590	21	7	0	9
DV-08-140	189	11	810	29	5	---	12
DV-08-142	216	11	674	16	7	---	10
DV-08-143	210	14	737	36	7	3	12
DV-08-144	306	21	1048	60	10	1	11
DV-08-145	326	25	1474	94	12	4	14
DV-08-146	157	11	1137	38	6	23	12
DV-08-148	223	12	473	0	7	3	6
DV-08-149	505	41	1400	88	14	10	26
DV-08-150	216	14	600	9	8	3	7
DV-08-151	202	9	1139	21	5	6	13

Sample	Zr	Nb	Ba	La	Hf	Pb	Th
DV-08-152	242	12	826	27	12	5	9
DV-08-153	207	10	777	28	6	4	6
DV-08-154	250	13	908	53	10	5	12
DV-08-155	253	14	94	44	10	4	13
DV-08-157	254	13	973	41	8	5	10

APPENDIX E

REE DATA (IN PPM)

The data reported in this appendix were obtained by inductively coupled mass spectrometry (ICP-MS) at Activation Laboratories LTD. Data are reported as provided by the laboratory with no adjustment for significant figures.

Sample	**Ce**	**Pr**	**Nd**	**Sm**	**Eu**	**Gd**	**Tb**	**Dy**	**Ho**	**Er**
DV-07-15	184	17.9	56.5	10.3	2.76	7.4	1	5.2	1	2.8
DV-07-20	161	16.2	53.3	9.8	2.66	7.1	1	5.1	0.9	2.7
DV-08-27	138	17.3	57.4	10.7	2.96	8.6	1.2	6.3	1.2	3.3
DV-08-29	95.7	10.3	37.2	7.8	2.17	6.4	0.9	5	0.9	2.8
DV-08-30	132	13.9	47.3	9.4	2.51	7.9	1.1	5.9	1	2.7
DV-08-31	141	16.9	54.5	10.2	2.71	8.3	1.2	5.7	1.1	3
DV-08-32	94	11.6	38.9	7.6	2.12	6.7	0.9	5.1	1	3
DV-08-34	180	18.3	59.3	11	2.96	7.9	1.1	5.3	1	2.7
DV-08-38	143	17.6	57.9	11	3.04	8.9	1.3	6.5	1.2	3.5
DV-08-39	178	18.1	59.7	11.1	2.99	8	1	5.4	1	2.8
DV-08-40	171	19.8	62.5	10.6	2.91	8	1.1	5.8	1.1	3.1
DV-08-42	109	13.9	48.5	9.5	2.64	7.8	1.1	6.1	1.2	3.3
DV-08-46	97.6	12.3	41	7.8	2.14	6.2	0.9	4.6	0.9	2.5
DV-08-56	77.4	9.65	33.4	6.5	1.79	5.4	0.8	4.6	0.9	2.6
DV-08-63	67.9	8.1	26.9	5.2	1.58	4.6	0.7	3.8	0.7	2.2
DV-08-69	65.2	7.35	28	6.3	1.92	5.5	0.8	4.7	0.9	2.8
DV-08-70	67.5	8.73	31.8	6.4	1.99	6.2	0.9	5.4	1.1	3.3
DV-08-72	128	12.8	43.5	7.8	2.14	5.9	0.9	4.8	0.9	2.7
DV-08-79	169	19.5	59.2	10.4	2.77	7.7	1.1	5.8	1.1	3
DV-08-83	164	18.8	59	10	2.64	7.7	1.1	5.3	1	2.9
DV-08-84	168	19.3	61.4	10.4	2.79	8	1.1	5.5	1	2.9
DV-08-86	151	15.3	51.2	9.5	2.52	6.8	0.9	4.8	0.9	2.5
DV-08-87	153	17.7	52.8	9.4	2.48	6.8	1	5.1	0.9	2.7
DV-08-89	128	12.6	42.5	7.6	2.08	5.6	0.8	4.1	0.8	2.3
DV-08-91	131	16.1	52.2	10	2.68	7.9	1.1	6	1.1	3.1
DV-08-92	121	11.9	39.3	7.2	1.96	5.3	0.7	3.9	0.7	2.1

Sample	Tm	Yb	Lu	Co	Cr	Ta	Zn	U	Cs
DV-07-15	0.4	2.5	0.37	163	110	1.5	130	2.8	0.5
DV-07-20	0.39	2.4	0.36	148	40	1.4	140	2	0.7
DV-08-27	0.46	2.7	0.37	165	70	1.3	150	1	0.5
DV-08-29	0.41	2.5	0.37	124	110	1.1	130	0.8	< 0.5
DV-08-30	0.36	2.1	0.3	55	30	1.1	140	0.8	< 0.5
DV-08-31	0.41	2.3	0.32	25	40	1.3	90	0.9	0.5
DV-08-32	0.41	2.5	0.34	77	120	1.1	100	0.9	< 0.5
DV-08-34	0.38	2.4	0.35	74	70	1.5	150	1.2	0.8
DV-08-38	0.49	2.8	0.39	38	90	1.5	190	0.9	< 0.5
DV-08-39	0.39	2.5	0.35	76	70	1.5	170	1.1	0.7
DV-08-40	0.42	2.5	0.36	83	20	1.4	110	1.4	0.5
DV-08-42	0.45	2.6	0.36	112	100	1.1	160	0.6	< 0.5
DV-08-46	0.34	2	0.28	100	50	1	30	0.6	< 0.5
DV-08-56	0.37	2.3	0.32	123	120	1	60	0.8	< 0.5
DV-08-63	0.3	1.8	0.25	140	140	0.7	80	0.6	< 0.5
DV-08-69	0.42	2.6	0.39	120	200	0.6	100	0.7	0.9
DV-08-70	0.49	2.9	0.42	105	220	0.8	100	0.6	< 0.5
DV-08-72	0.4	2.5	0.38	141	250	1	100	1	< 0.5
DV-08-79	0.43	2.6	0.38	32	40	1.6	140	1.9	1
DV-08-83	0.4	2.3	0.32	146	50	1.5	150	1.5	1
DV-08-84	0.39	2.4	0.33	37	60	1.6	160	1.3	0.7
DV-08-86	0.35	2.1	0.32	119	90	1.4	130	1.3	0.5
DV-08-87	0.36	2.1	0.31	161	50	1.4	130	1.4	0.6
DV-08-89	0.33	2.1	0.31	182	200	1.1	130	1.1	0.8
DV-08-91	0.41	2.4	0.32	43	30	1.1	80	1.1	< 0.5
DV-08-92	0.31	2	0.29	180	90	1	120	1	0.5

Sample	Zr	W	Mo	Ag	In	Sn	Sb	Tl	Bi
DV-07-15	292	387	< 2	< 0.5	< 0.2	1	1.2	< 0.1	< 0.4
DV-07-20	307	373	< 2	< 0.5	< 0.2	1	0.8	0.1	< 0.4
DV-08-27	313	401	< 2	< 0.5	< 0.2	2	0.7	0.2	29.3
DV-08-29	210	289	< 2	< 0.5	< 0.2	1	0.9	0.3	< 0.4
DV-08-30	236	104	< 2	< 0.5	< 0.2	< 1	< 0.5	0.2	< 0.4
DV-08-31	217	24	< 2	< 0.5	< 0.2	1	0.9	0.1	4.7
DV-08-32	218	149	< 2	< 0.5	< 0.2	1	0.7	0.3	16.4
DV-08-34	292	166	< 2	< 0.5	< 0.2	1	0.6	0.2	< 0.4
DV-08-38	315	23	< 2	< 0.5	< 0.2	1	0.7	0.1	31.5
DV-08-39	336	142	< 2	< 0.5	< 0.2	2	0.9	0.2	< 0.4
DV-08-40	319	192	< 2	< 0.5	< 0.2	2	0.7	< 0.1	1.7
DV-08-42	268	212	< 2	< 0.5	< 0.2	2	0.8	< 0.1	10.3
DV-08-46	186	213	< 2	< 0.5	< 0.2	< 1	< 0.5	< 0.1	< 0.4
DV-08-56	149	278	< 2	< 0.5	< 0.2	< 1	< 0.5	0.2	9
DV-08-63	168	295	< 2	< 0.5	< 0.2	1	0.8	0.1	3.1
DV-08-69	197	290	< 2	< 0.5	< 0.2	1	1	< 0.1	< 0.4
DV-08-70	237	231	< 2	< 0.5	< 0.2	2	1.1	0.2	28.1
DV-08-72	263	351	< 2	< 0.5	< 0.2	2	1.3	0.2	< 0.4
DV-08-79	357	46	< 2	< 0.5	< 0.2	1	1.1	0.4	25.2
DV-08-83	332	347	< 2	< 0.5	< 0.2	2	0.7	0.2	75.4
DV-08-84	316	38	< 2	< 0.5	< 0.2	2	0.6	0.3	83.2
DV-08-86	246	274	< 2	< 0.5	< 0.2	< 1	1	< 0.1	< 0.4
DV-08-87	299	409	< 2	< 0.5	< 0.2	1	1	0.1	39.6
DV-08-89	242	467	< 2	< 0.5	< 0.2	1	101	0.5	3.5
DV-08-91	225	74	< 2	< 0.5	< 0.2	< 1	< 0.5	< 0.1	1.2
DV-08-92	227	485	< 2	< 0.5	< 0.2	< 1	1.4	0.5	< 0.4

Sample	Ce	Pr	Nd	Sm	Eu	Gd	Tb	Dy	Ho	Er
DV-08-93	122	14.6	48.1	8.9	2.52	7.4	1.1	5.7	1.1	3.2
DV-08-96	129	13.7	47.4	9.9	2.64	7.2	1	5.5	1	2.8
DV-08-101	129	15.6	50.2	9.1	2.58	7.6	1.1	5.8	1.1	3.4
DV-08-102	123	13	44.9	9	2.52	6.9	1	5.4	1	3
DV-08-108	78	8.09	28.8	6	1.71	5.2	0.8	4.6	0.9	2.8
DV-08-110	160	16.9	58.6	11.8	3.14	8.6	1.2	6.1	1.1	3.2
DV-08-114	98	12.5	44	8.7	2.53	7.6	1.1	5.8	1.1	3.3
DV-08-118	167	18.6	52.8	9.3	2.53	6.8	1	5.2	1	2.8
DV-08-119	169	18.7	57.4	9.5	2.61	7.3	1	5.4	1.1	3.1
DV-08-120	158	17.4	52.3	9	2.47	6.9	0.9	5.1	1	2.9
DV-08-121	163	18.1	54.6	9.4	2.48	7.1	1	5.5	1	3
DV-08-125	42.5	5.68	21.5	4.9	1.53	5	0.8	5.2	1.1	3.3
DV-08-127	206	22.8	65.3	10.9	2.83	7.5	1	5.3	1	2.7
DV-08-128	96	11.9	40.7	8.1	2.36	6.9	1	5.5	1	3
DV-08-130	118	13.6	42	7.6	2.23	6.1	0.9	5	1	2.9
DV-08-132A	84.4	10.1	32.8	6.3	1.86	5.5	0.9	4.9	1	2.8
DV-08-133	63.1	6.94	21.3	3.8	0.97	3.1	0.5	2.7	0.5	1.7
DV-08-134	59.2	7.23	24.5	4.8	1.48	4.2	0.7	3.9	0.8	2.3
DV-08-138	50.2	6.5	24	5	1.59	4.4	0.7	4	0.8	2.3
DV-08-139	55.3	7.09	24.8	5.2	1.75	4.9	0.8	4.1	0.8	2.5
DV-08-144	124	15.7	53.2	10	2.71	7.9	1.1	5.9	1.1	3.1
DV-08-145	158	18.3	55.6	9.8	2.65	7.5	1	5.1	1	2.7
DV-08-146	67.9	7.25	21.4	3.6	0.76	2.7	0.4	2.3	0.5	1.4
DV-08-149	167	19.2	58.9	10.2	2.75	7.9	1.1	5.5	1	2.9
DV-08-154	84	10.4	34.9	6.5	1.92	5.7	0.9	5	1	2.9

Sample	Tm	Yb	Lu	Co	Cr	Ta	Zn	U	Cs
DV-08-93	0.44	2.6	0.37	36	70	1.6	80	1.1	< 0.5
DV-08-96	0.38	2.3	0.33	86	20	1.2	50	1.5	< 0.5
DV-08-101	0.48	2.9	0.4	126	80	1.3	110	0.8	0.5
DV-08-102	0.44	2.8	0.4	142	80	1.3	140	0.8	0.5
DV-08-108	0.41	2.6	0.39	87	30	0.8	< 30	0.7	< 0.5
DV-08-110	0.44	2.7	0.38	77	50	1.4	140	0.9	0.5
DV-08-114	0.44	2.6	0.37	92	120	1.1	130	0.7	< 0.5
DV-08-118	0.38	2.4	0.35	41	90	1.7	140	2.5	1.2
DV-08-119	0.46	2.6	0.38	109	20	1.5	120	2.4	1.3
DV-08-120	0.4	2.5	0.35	33	50	1.6	130	2.2	0.8
DV-08-121	0.44	2.5	0.38	107	< 20	1.5	140	2.4	0.8
DV-08-125	0.48	2.9	0.41	135	200	0.3	70	0.4	< 0.5
DV-08-127	0.37	2.2	0.32	28	70	2	120	3	3
DV-08-128	0.43	2.5	0.34	141	60	1	150	0.4	< 0.5
DV-08-130	0.4	2.5	0.35	32	90	1.4	120	1.2	< 0.5
DV-08-132A	0.4	2.4	0.34	127	150	1.1	110	1.1	1.1
DV-08-133	0.25	1.6	0.25	147	70	1	40	2.4	2
DV-08-134	0.34	2.1	0.29	144	80	0.9	90	0.9	3.4
DV-08-138	0.33	2	0.29	106	140	0.8	60	0.8	< 0.5
DV-08-139	0.36	2.1	0.31	126	170	0.8	70	0.7	< 0.5
DV-08-144	0.43	2.5	0.37	178	80	1.3	160	0.7	< 0.5
DV-08-145	0.38	2.2	0.31	115	70	1.4	150	1.3	0.5
DV-08-146	0.22	1.4	0.2	16	< 20	1.5	30	2.7	2.1
DV-08-149	0.4	2.4	0.33	37	50	1.7	160	1.5	0.6
DV-08-154	0.42	2.5	0.37	35	170	1.1	70	1	< 0.5

Sample	Zr	W	Mo	Ag	In	Sn	Sb	Tl	Bi
DV-08-93	223	48	< 2	< 0.5	< 0.2	1	< 0.5	0.1	26.1
DV-08-96	123	185	< 2	< 0.5	< 0.2	< 1	< 0.5	< 0.1	< 0.4
DV-08-101	299	280	< 2	< 0.5	< 0.2	1	0.5	< 0.1	16.2
DV-08-102	277	347	< 2	< 0.5	< 0.2	1	0.8	0.1	< 0.4
DV-08-108	149	259	< 2	< 0.5	< 0.2	< 1	< 0.5	< 0.1	< 0.4
DV-08-110	241	158	< 2	1.4	< 0.2	1	0.6	0.2	< 0.4
DV-08-114	262	178	< 2	< 0.5	< 0.2	2	0.6	0.1	21
DV-08-118	359	75	< 2	< 0.5	< 0.2	1	0.6	0.2	17.2
DV-08-119	361	245	< 2	< 0.5	< 0.2	2	< 0.5	0.3	11.7
DV-08-120	342	56	< 2	< 0.5	< 0.2	2	1.1	0.3	13
DV-08-121	362	257	< 2	< 0.5	< 0.2	1	0.9	0.4	18.9
DV-08-125	183	283	< 2	< 0.5	< 0.2	1	1.2	0.1	29.3
DV-08-127	376	36	< 2	< 0.5	< 0.2	1	< 0.5	0.3	24.1
DV-08-128	226	313	< 2	< 0.5	< 0.2	1	0.9	< 0.1	< 0.4
DV-08-130	285	40	< 2	< 0.5	< 0.2	2	0.8	0.1	33.1
DV-08-132A	226	316	< 2	1	< 0.2	2	1	< 0.1	31.2
DV-08-133	226	374	< 2	< 0.5	< 0.2	1	1.3	0.6	11.4
DV-08-134	209	391	< 2	< 0.5	< 0.2	< 1	2	0.5	22.1
DV-08-138	124	230	< 2	< 0.5	< 0.2	< 1	0.6	< 0.1	16.3
DV-08-139	134	273	< 2	< 0.5	< 0.2	< 1	0.7	< 0.1	13.2
DV-08-144	291	421	< 2	< 0.5	< 0.2	1	0.6	0.1	0.6
DV-08-145	298	220	< 2	< 0.5	< 0.2	2	0.8	0.2	4
DV-08-146	161	69	< 2	< 0.5	< 0.2	< 1	0.7	1	68.1
DV-08-149	315	53	< 2	< 0.5	< 0.2	2	1.1	< 0.1	32.3
DV-08-154	217	68	< 2	< 0.5	< 0.2	< 1	< 0.5	< 0.1	12.9

APPENDIX F

ISOTOPIC DATA

The data reported in this appendix were obtained by VG Sector 54 mass spectrometer at the University of Kansas Isotope Geochemistry Laboratory. Data are reported as provided by the laboratory with no adjustment for significant figures.

Sample	$^{206}Pb/^{204}Pb$	$^{207}Pb/^{204}Pb$	$^{208}Pb/^{204}Pb$	$^{87}Sr/^{86}Sr$	$^{143}Nd/^{144}Nd$	ε_{Nd}
DV-07-15	18.254	15.545	38.462	0.707062	0.512114	-10.21
DV-07-20	18.142	15.550	38.599	0.707600	0.512093	-10.63
DV-08-27	17.942	15.550	38.692	0.707400	0.512072	-11.05
DV-08-29	17.822	15.519	38.854	0.706789	0.512186	-8.82
DV-08-30	18.104	15.586	38.836	0.707631	0.512063	-11.21
DV-08-34	18.059	15.545	38.497	0.707490	0.512079	-10.90
DV-08-39	18.047	15.541	38.481	0.707219	0.512083	-10.83
DV-08-42	18.027	15.559	38.771	0.707468	0.512103	-10.43
DV-08-46	17.912	15.528	38.633	0.707452	0.512076	-10.96
DV-08-56	17.764	15.521	38.840	0.706620	0.512203	-8.48
DV-08-63	17.975	15.533	38.608	0.706322	0.512187	-8.79
DV-08-69	18.509	15.587	38.820	0.706925	0.512471	-3.26
DV-08-72	18.146	15.555	38.821	0.707417	0.512081	-10.87
DV-08-79	18.165	15.576	38.678	0.707487	0.512038	-11.71
DV-08-86	18.167	15.557	38.615	0.707494	0.512083	-10.83
DV-08-87	18.212	15.603	38.735	0.707053	0.512096	-10.57
DV-08-89	17.827	15.512	38.237	0.707163	0.512075	-10.98
DV-08-91	18.126	15.577	38.805	0.707973	0.512059	-11.29
DV-08-92	17.776	15.526	38.283	0.707191	0.512114	-10.21
DV-08-96	18.040	15.520	38.622	0.707792	0.512073	-11.02
DV-08-102	18.464	15.574	38.662	0.706358	0.512181	-8.92
DV-08-108	18.390	15.591	39.603	0.707928	0.512182	-8.89
DV-08-110	18.001	15.543	38.643	0.707486	0.512029	-11.88
DV-08-118	18.227	15.583	38.583	0.706940	0.512100	-10.49
DV-08-121	18.206	15.570	38.610	0.707161	0.512079	-10.90
DV-08-125	18.206	15.603	40.531	0.709790	0.512306	-6.48
DV-08-127	18.361	15.588	38.732	0.707399	0.511977	-12.89
DV-08-130	18.209	15.569	38.631	0.706501	0.512236	-7.83
DV-08-132A	17.856	15.528	38.529	0.706402	0.512219	-8.18
DV-08-134	18.422	15.593	38.886	0.706516	0.512385	-4.93
DV-08-138	18.573	15.596	38.826	0.706113	0.512516	-2.38
DV-08-144	18.004	15.556	38.713	0.707374	0.512041	-11.65
DV-08-146	18.108	15.577	38.782	0.708529	0.512106	-10.38
DV-08-149	18.117	15.537	38.536	0.707108	0.512053	-11.42
DV-08-154	18.089	15.565	38.715	0.707285	0.512263	-7.31

APPENDIX G

ASSESSMENT OF PREVIOUSLY PROPOSED MODELS FOR DEATH VALLEY AND SURROUNDING REGIONS

Slab window

The slab window model for asthenospheric upwelling is based on the concept that during subduction the Farallon slab prevented the asthenosphere from rising to the continental lithosphere above the slab. Once the slab migrated away from the area, a "slab window" opened and the asthenosphere rose to fill the space (Fig. G1) (Ormerod et al., 1988; Jones et al, 1992). The Farallon slab migrated north of California and Nevada as the San Andreas transform developed (Ormerod, 1988) and the East Pacific Rise intersected the subduction zone effectively stopping subduction. Motion between the North American Plate and the Pacific Plate was then accommodated by the San Andreas Fault (Atwater, 1970), the eastern California shear zone, and the Walker Lane (Wesnousky, 2005). The lithosphere to asthenosphere source change of magmatism in this region also migrated north with time (Ormerod et al., 1988; Farmer et al., 1989; Jones et al., 1992). This change in source is believed to be caused by the opening of a slab window to the north allowing for asthenospheric upwelling. There is, however, a lag time of 2-3 m.y. between slab removal and volcanism due to a 5-8 cm/yr upwelling rate of asthenosphere over 230 km to the base of the lithosphere (Ormerod et al., 1988).

The main problems associated with the slab window model are both temporal and isotopic. The slab was removed from under the Death Valley area by 20 Ma and even with a 2-3 my time lag, mantle upwelling cannot explain the ~4 Ma basalts of the Greenwater Range. Furthermore, pure asthenospheric melting by upwelling of deeper mantle would produce an OIB trace element signature but cannot explain the observed trace element variation from OIB or the isotopic signature.

Lithospheric melting

The melting of basaltic components in the subcontinental mantle due to lithospheric thinning and the subsequent crossing of the basalt solidus assumes that the subcontinental mantle has a temperature of at least 1300^{o}C and is composed of peridotite which contains dry tholeiitic mafic components such as pods, sills, and dikes produced from an ancient subduction zone (Harry and Leeman, 1995). The model works best for an initial lithospheric thickness of 125 km with melting occurring in the lower 25 km of the lithospheric mantle (Fig. G2), but is also relevant for initial thicknesses of 100-150 km. The 125 km thick lithosphere thins due to extension, causing the dry tholeiitic mafic components to cross the basalt solidus and melt. Volcanism from 20-17 Ma was silicic and between 17-6 Ma was intermediate to basaltic (Eaton, 1982) in the Great Basin. Initial silicic volcanism was most likely produced by crustal anatexis caused by heat from coeval mafic melts at mantle depths. After 25-30% extension, lithospheric melting decreased in volume (Fig. G2), thus accounting for the decrease in the volume of early silicic volcanism (Harry and Leeman, 1995). This volume decrease is estimated to occur at ~5 Ma, concurrent with reaching 25-30% extension and the observed change in magmatic source from lithospheric to asthenospheric mantle (Harry and Leeman, 1995). After 25-30% extension the lithosphere thinned enough to allow for asthenospheric upwelling, which caused the change in magmatic source from lithospheric to asthenospheric mantle at 5 Ma (Harry et al., 1993; Harry and Leeman, 1995). The proposed rise of the lithosphere-asthenosphere boundary and relatively constant depth of melting (Harry et al., 1993; Harry and Leeman, 1995) was supported in a study of basaltic volcanism at Lake Mead (Nevada and Arizona) by Feuerbach et al. (1993).

Melting of the lithosphere can also be accomplished by the addition of heat from asthenospheric upwelling as the result of the opening of a slab window. The added heat will initially melt the lithosphere before the upwelling asthenosphere undergoes decompression melting and the source changes from lithospheric to asthenospheric with time (Ormerod et al., 1988; Ormerod et al., 1991).

Mantle lithosphere can also be melted during rapid extension of the lithosphere. As the lithosphere extends, the lithosphere-asthenosphere boundary moves to a shallower depth, causing the geotherm to rise and allowing H_2O-bearing peridotite (1-3%) to cross the solidus and melt (Fig. G3) (DePaolo and Daley, 2000). Gallagher and Hawkesworth (1992) state that given the extension of a depleted peridotite lithosphere over anomalously hot mantle, ~0.4 wt% water is sufficient to melt the lithosphere to produce silica saturated basalt and leave residual olivine. The more the geotherm rises the more peridotite enters the melting field and the greater the melt fraction. As extension slows, the geotherm is depressed, decreasing the amount of melting (Daley and DePaolo, 1992). The shallowing of the lithosphere-asthenosphere boundary also allows the asthenosphere to rise to fill the space and undergo decompression melting, resulting in an eventual change from lithospheric to asthenospheric source with a decrease in pressure/depth of melting and an increase in the degree of partial melting (DePaolo and Daley, 2000; Daley and DePaolo, 1992). At extension factors (β = extended length/original length) of greater than 1.2-1.3 and a mechanical boundary layer (lithospheric mantle) of 100 km the asthenosphere will rise and dominate the chemical signature of basalt magma (Gallagher and Hawkesworth, 1992).

The model of Harry and Leeman (1995) for a transition from lithospheric to asthenospheric melting due to lithospheric thinning has several problems. First, it is used to explain early silicic volcanism which, according to Eaton (1982), occurred from 20-17 Ma; but Death Valley extension did not begin until 16 Ma (Daley and DePaolo, 1992). Second, during extension there was only thinning from 100 to 40 km (DePaolo and Daley, 2000), this is the lower limit for a working initial thickness, which would decrease the effectiveness of the model for the Death Valley area. In addition to this, given 25-30% extension before the change in source from lithosphere to asthenosphere (Harry and Leeman 1995) and the extension rate of 20-30 mm/yr between 16-5 Ma and 10 mm/yr from 5 Ma to the present (Daley and DePaolo, 1992) it would only take 5.5 -6.5 m.y. after the onset of extension to reach 25-30% extension and change source. This puts asthenospheric upwelling and the change in source for this region at 10.5-9.5 Ma, not at ~5 Ma as proposed by Harry et al. (1993) and Harry and Leeman (1995).

The main problem with all other lithosphere to asthenosphere source models is the simple fact that they cannot explain the exceptions to the OIB trace element signature and lithospheric isotopic signature when an overall asthenospheric source signature is expected. Most of the above described models melt an upwelling peridotite source that would require large amounts of lithospheric contamination to account for the isotopic signature seen in the Greenwater Range basalts. The large amount of lithospheric contamination would contaminate the source enough to change it to a lithospheric trace element signature as well and, depending on the contaminant, could result in a more evolved composition.

The only models that may account for the observed chemical and isotopic signatures in the Greenwater Range are those that include the shallowing of the lithosphere-asthenosphere boundary and the melting of mantle that was previously lithosphere before the rise of the geotherm, as in the model proposed by DePaolo and Daley (2000). Gallagher and Hawkesworth's (1992) suggestion of upwelling asthenosphere creating a dominant asthenospheric signature could explain part of the signature seen in the Greenwater basalts. However, this model can only explain the asthenospheric signature and does not explain the combination of lithospheric and asthenospheric signatures. This suggests that this model needs revising before it can be considered a viable melting model.

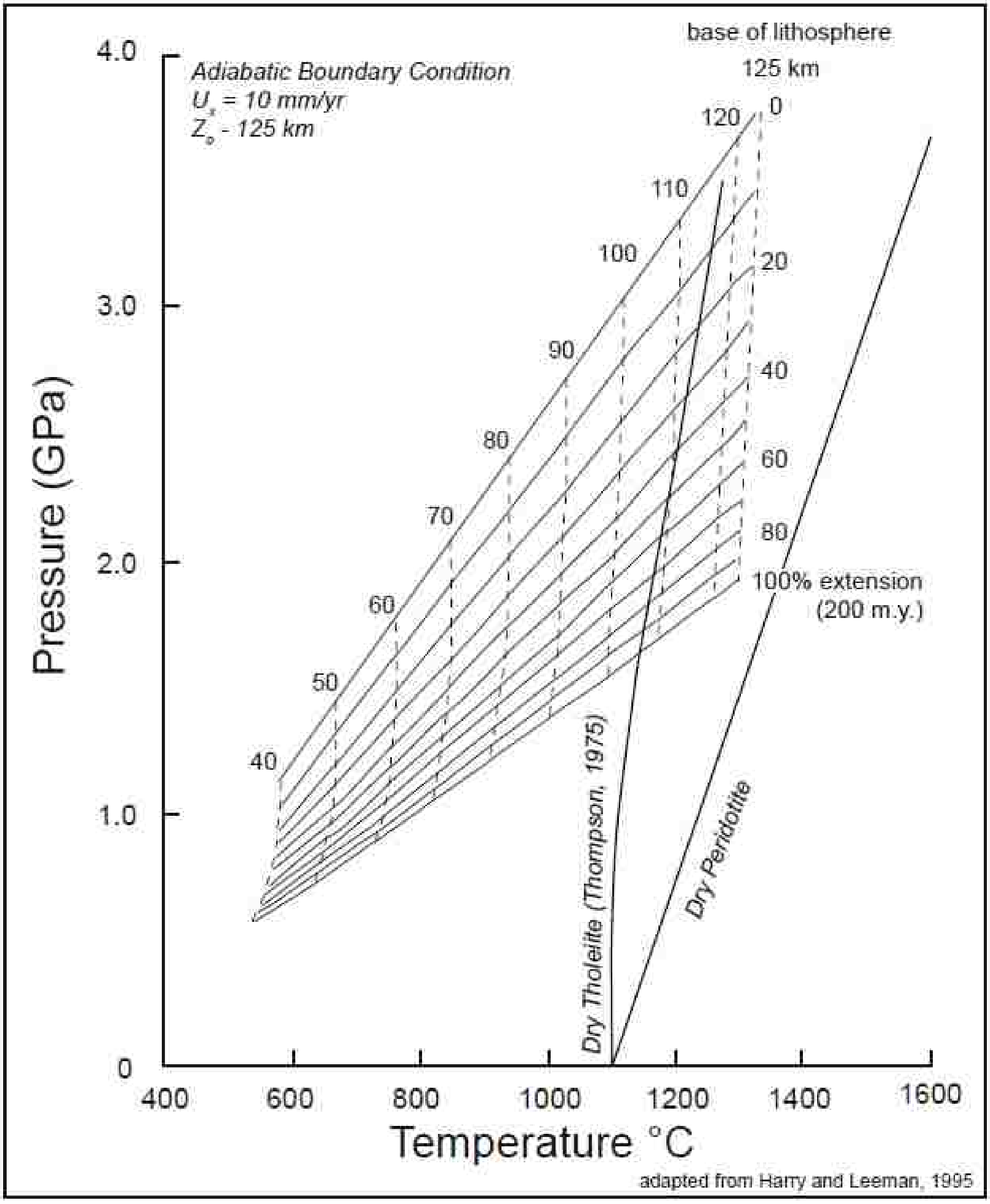

Figure G1: P-T path of basalts over time with continued extension. A dry tholeiitic solidus produces melting in the lower 25 km of the lithosphere, as the rocks initial depths rise to lower pressures entering the melting field (sub-horizontal grid lines move down as lithosphere thins and base moves to shallower depths). As extension increases (down the right hand axis), the field of melt (the area to the right of the dry tholeiite solidus) increases from approximately 5- 25 km of the lower lithosphere. After Harry and Leeman (1995).

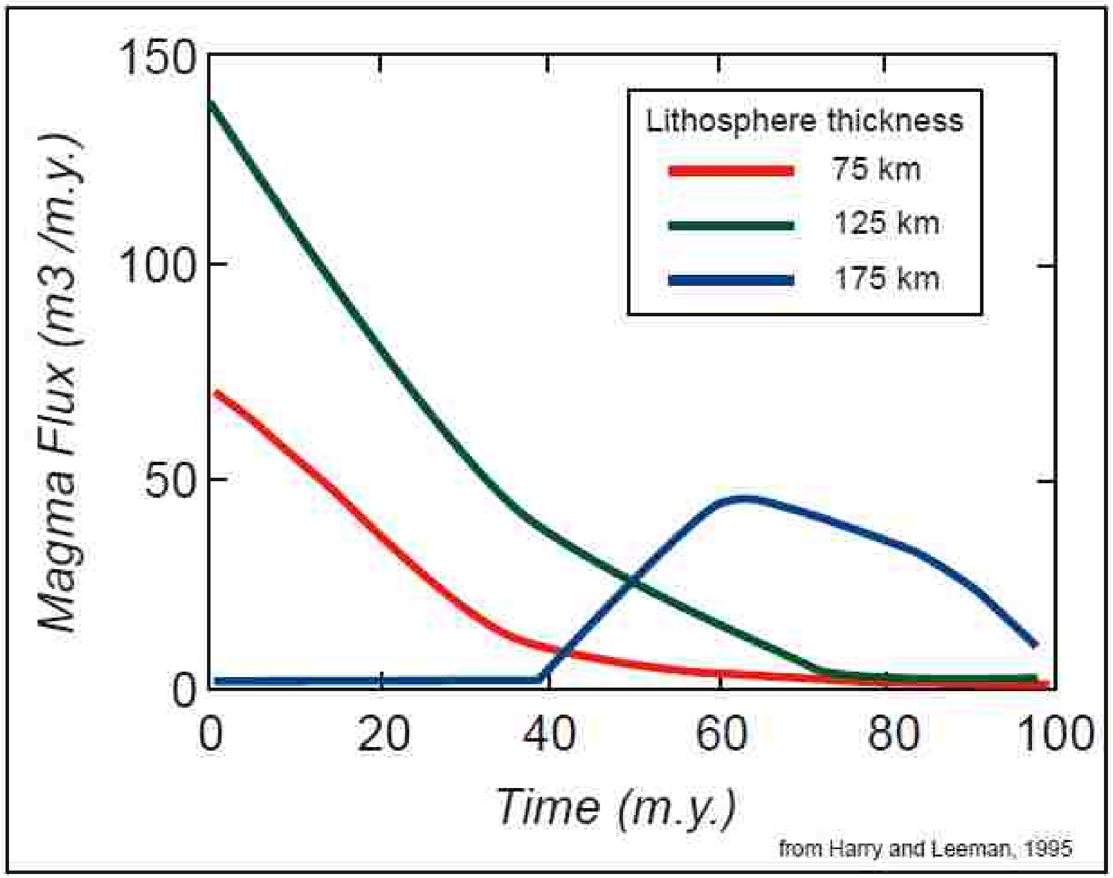

Figure G2: The volume of magmatism decreases over time for the 125 km initial lithospheric thickness model. This agrees with the observed waning volcanism in the Lunar Crater-Crater Flat belt (Harry and Leeman, 1995).

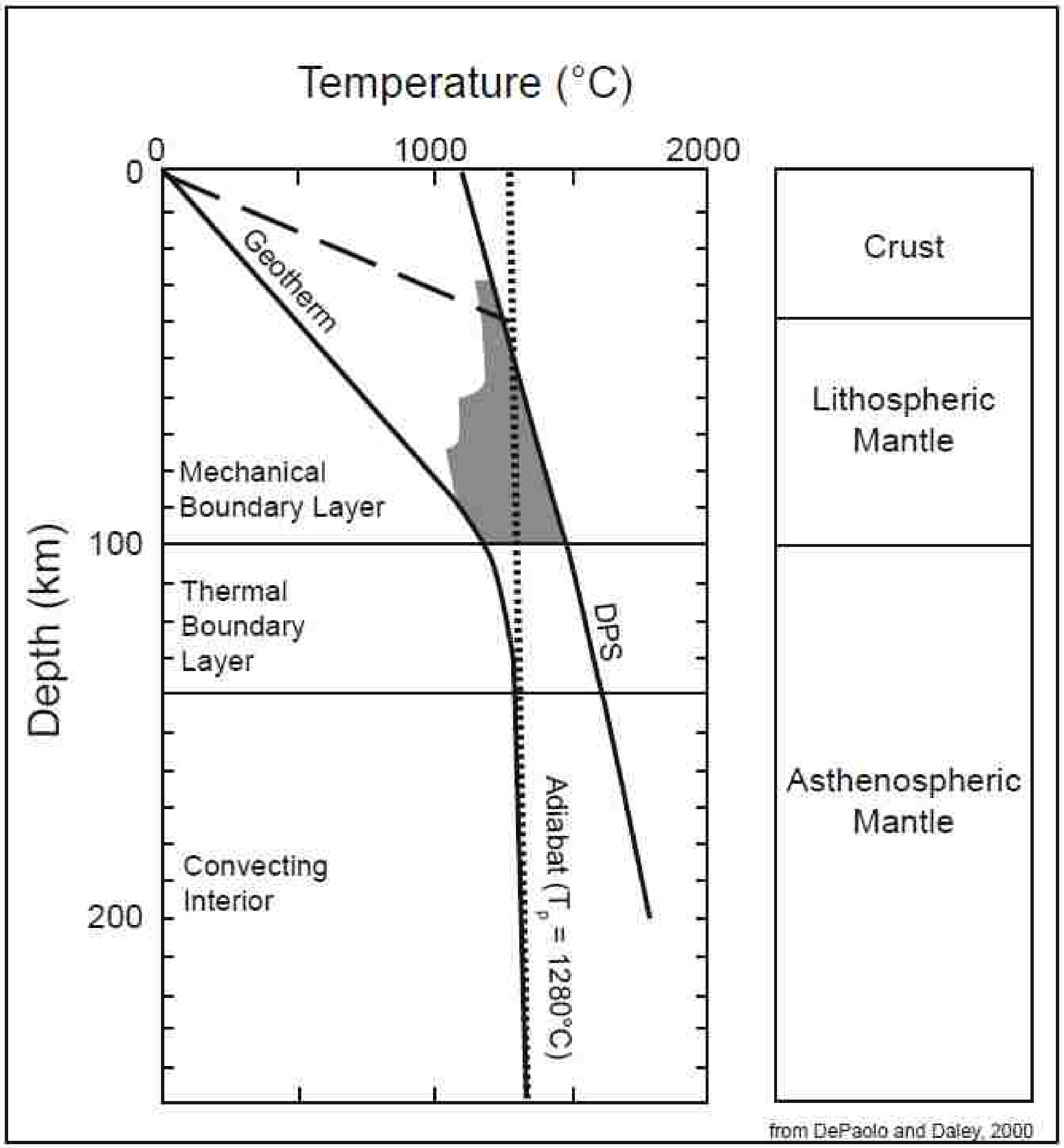

Figure G3: Depth vs. temperature in the lithosphere and upper asthenospheric mantle. DPS is the dry peridotite solidus. Solid curve is a stable geotherm for a 100-km-thick chemical lithosphere. Dotted line is an adiabat; long dashed line is an approximate geotherm after the lithosphere has been rapidly thinned to 40-km thickness. Shaded region is the extended melting region for H_2O-bearing peridotite. (DePaolo and Daley, 2000).

APPENDIX H

FIELD PICTURES

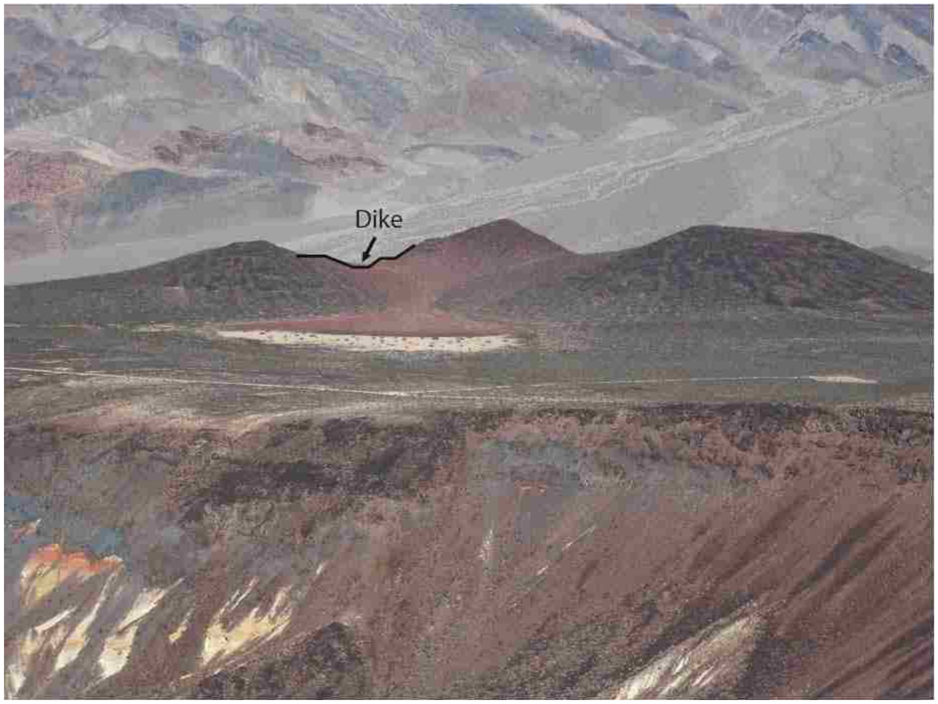

Picture 1: Three Peaks as seen from the south. Dike crops out between the two left most cones. Playa in foreground partially overlain by a thin layer of scoria.

Picture 2: Smith's climb as seen from the west. Scoria deposits visible in the foreground.

Picture 3: Crater as viewed from north. Arrow points to crater wall, with crater in the foreground.

Picture 4: Zoned bomb embedded in welded scoria of the Crater. Bomb displays red vesicular core and blue degassed rim.

Picture 5: Bedded scoria lapping against crater wall. Arrows points to bedding.

Picture 6: Sedimentary xenoliths form the Furnace Creek or Artist Drive Formation in the basalt of the Crater.

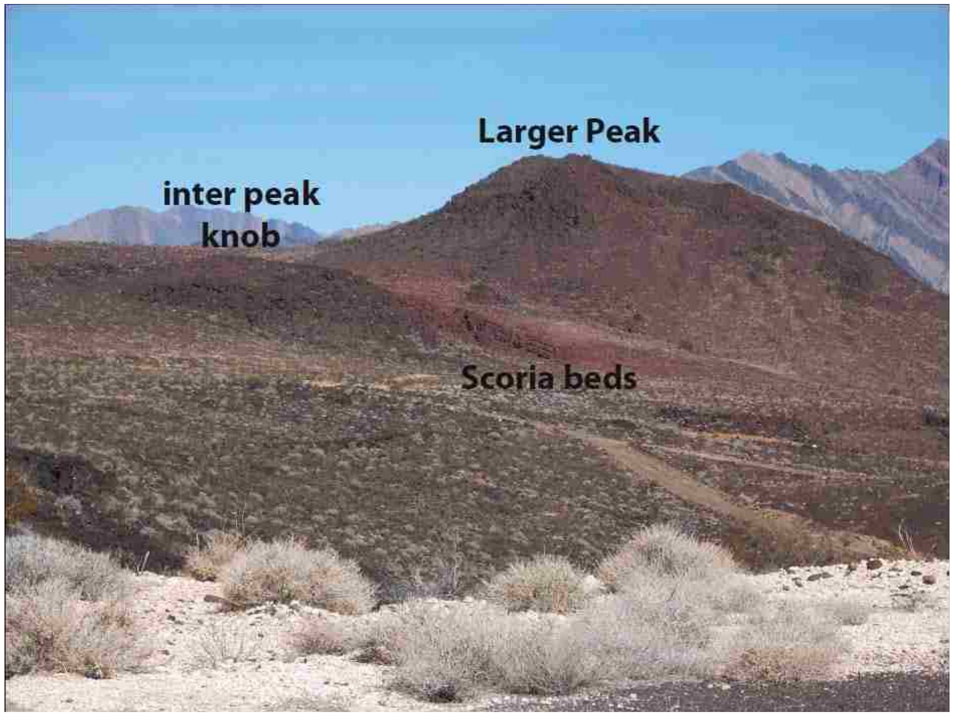

Picture 7: Two Peaks larger peak and inter peak knob as seen from the southwest.

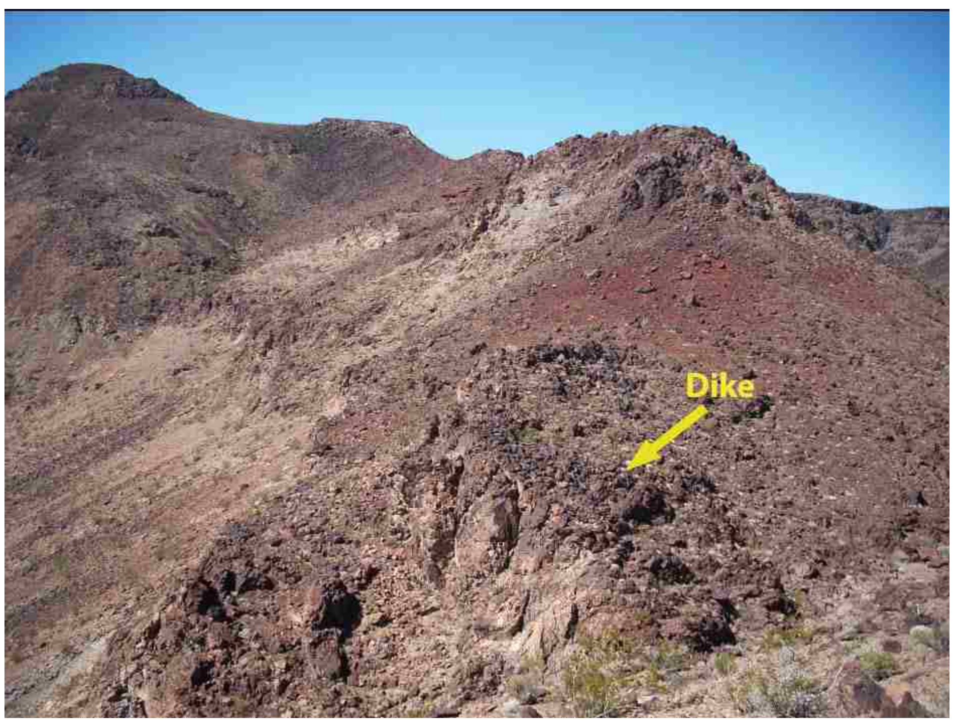

Picture 8: Point Cone as seen from bottom knob looking along the connecting dike.

Picture 9: Point Cone bombs on highest knob.

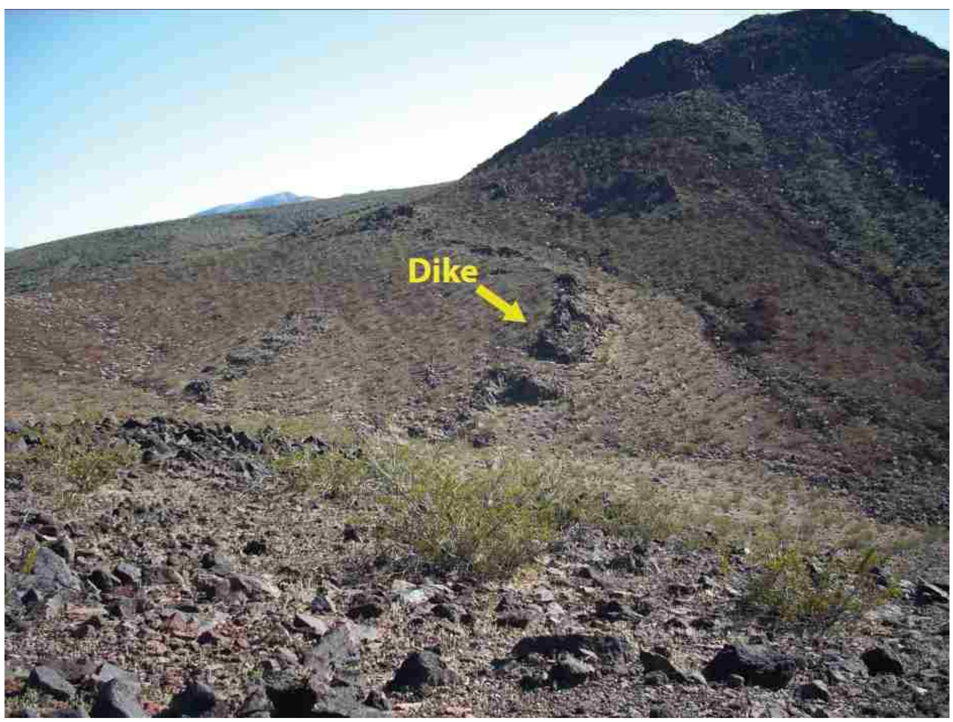

Picture 10: Lower Cone 1 and associated dikes as seen from the north.

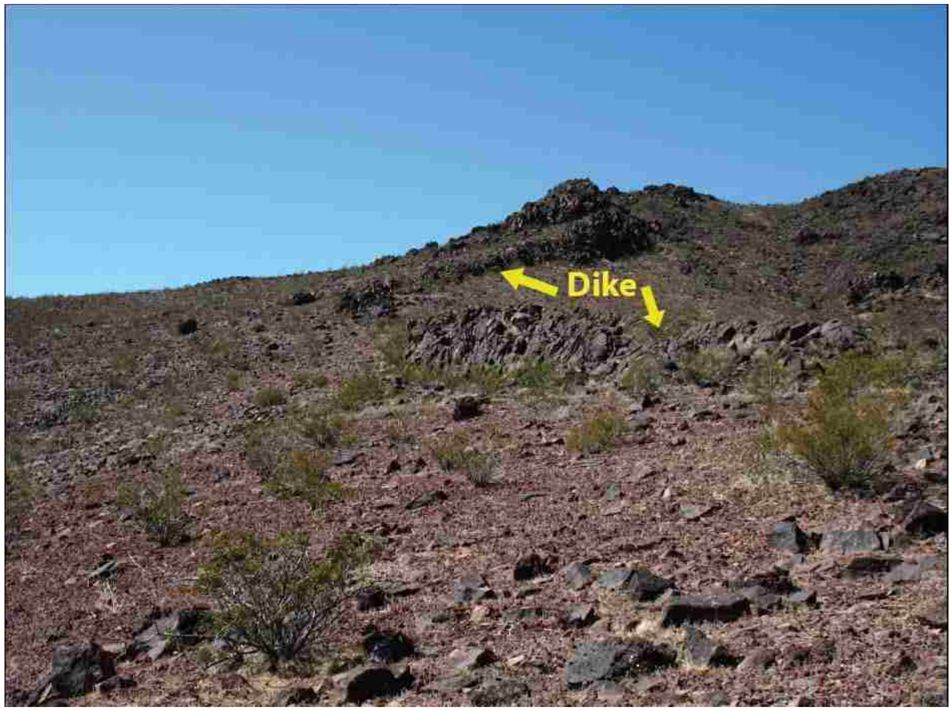

Picture 11: Dikes of Lower Cone 1 as seen from the east.

:


Picture 12: Lower Cone 2 as seen from the south.


Picture 13: Sculpted bomb on the flank of Lower Cone 2.


Picture 14: Lower Plug as seen from the west.

Picture 15: Mesa Center as seen from the north.

Picture 16: Exposed scoria beds at base of Tall Peak.

Picture 17: Old Peak as seen from the South.

Picture 18: Basalt overlying the rhyolite in the southwestern end of the field.

Picture 19: Northernmost conduit of the Southeast Center.

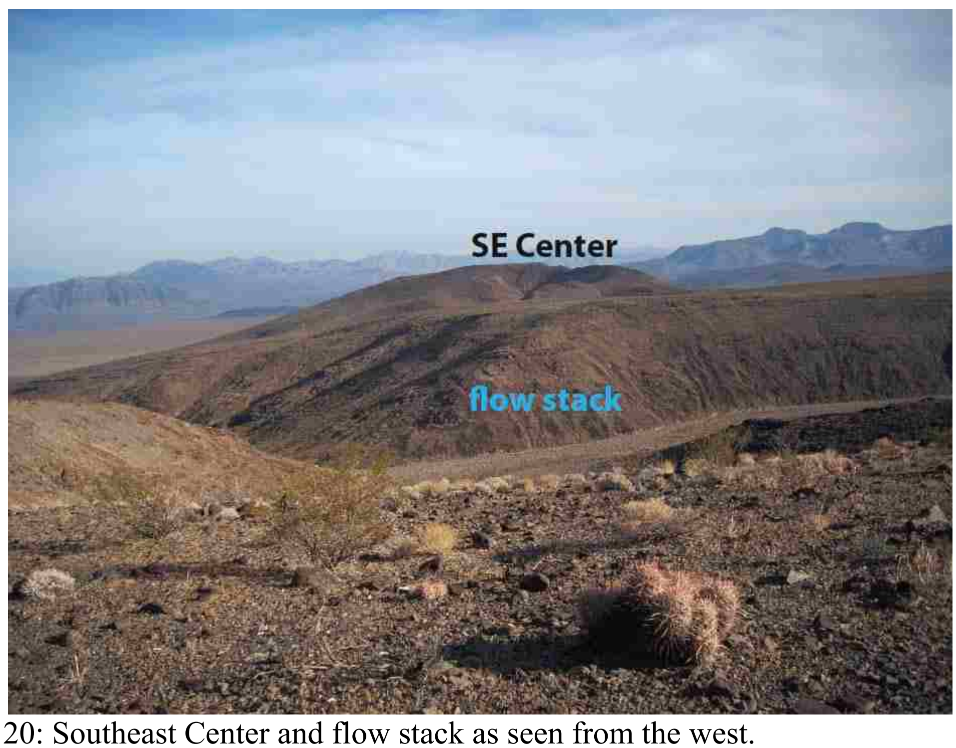

Picture 20: Southeast Center and flow stack as seen from the west.

Picture 21: Basalt enclave in the rhyolite near the basalt/rhyolite contact.

VITA

Graduate College
University of Nevada, Las Vegas

Ashley K. Tibbetts

Degrees:

Bachelor of Science in Earth Sciences, 2007
Boston University

Thesis Title: Petrogenesis of the Greenwater Range: Comparison to the Crater Flat Volcanic Field and Implications for Hazard Assessment

Thesis Examination Committee:

Chairperson, Dr. Eugene Smith, Ph.D.
Committee Member, Dr. Adam Simon, Ph.D.
Committee Member, Dr. Pamela Burnley, Ph.D.
Committee Member, Dr. Diane Pyper-Smith, Ph.D.